JOURNAL OF PETROLOGY | VOLUME 47 | NUMBER 1 | PAGES 145–189 | 2006 | doi:10.1093/petrology/egi071

Sampling the Cape Verde Mantle Plume: Evolution of Melt Compositions on Santo Antão, Cape Verde Islands

P. M. HOLM[1]*, J. R. WILSON[2], B. P. CHRISTENSEN[1], L. HANSEN[2], S. L. HANSEN[1], K. M. HEIN[1], A. K. MORTENSEN[2], R. PEDERSEN[2], S. PLESNER[2] AND M. K. RUNGE[1]

[1]GEOLOGICAL INSTITUTE, UNIVERSITY OF COPENHAGEN, GEOCENTER COPENHAGEN, DK-1350 COPENHAGEN, DENMARK

[2]DEPARTMENT OF EARTH SCIENCES, AARHUS UNIVERSITY, DK-8000 ÅRHUS C, DENMARK

RECEIVED OCTOBER 10, 2003; ACCEPTED JULY 11, 2005
ADVANCE ACCESS PUBLICATION SEPTEMBER 6, 2005

The volcanic history of Santo Antão, NW Cape Verde Islands, includes the eruption of basanite–phonolite series magmas between 7·5 and 0·3 Ma and (melilite) nephelinite–phonolite series magmas from 0·7 to 0·1 Ma. The most primitive volcanic rocks are olivine ± clinopyroxene-phyric, whereas the more evolved rocks have phenocrysts of clinopyroxene ± Fe–Ti oxide ± kaersutite ± haüyne ± titanite ± sanidine; plagioclase occurs in some intermediate rocks. The analysed samples span a range of 19–0·03% MgO; the most primitive have 37–46% SiO_2, 2·5–7% TiO_2 and are enriched 50–200 × primitive mantle in highly incompatible elements; the basanitic series is less enriched than the nephelinitic series. Geochemical trends in each series can be modelled by fractional crystallization of phenocryst assemblages from basanitic and nephelinitic parental magmas. There is little evidence for mineral–melt disequilibrium, and thus magma mixing is not of major importance in controlling bulk-rock compositions. Mantle melting processes are modelled using fractionation-corrected magma compositions; the models suggest 1–4% partial melting of a heterogeneous mantle peridotite source at depths of 90–125 km. Incompatible element enrichment among the most primitive magma types is typical of HIMU OIB. The Sr, Nd and Pb isotopic compositions of the Santo Antão volcanic sequence and geochemical character change systematically with time. The older volcanic rocks (7·5–2 Ma) vary between two main mantle source components, one of which is a young HIMU type with $^{206}Pb/^{204}Pb = 19{\cdot}88$, $\Delta 7/4 = -5$, $\Delta 8/4 \approx 0$, $^{87}Sr/^{86}Sr = 0{\cdot}7033$ and $^{143}Nd/^{144}Nd = 0{\cdot}51288$, whereas the other has somewhat less radiogenic Sr and Pb and more radiogenic Nd. The intermediate age volcanic rocks (2–0·3 Ma) show a change of sources to two-component mixing between a carbonatite-related young HIMU-type source ($^{206}Pb/^{204}Pb = 19{\cdot}93$, $\Delta 7/4 = -5$, $\Delta 8/4 = -38$, $^{87}Sr/^{86}Sr = 0{\cdot}70304$) and a DM-like source. A more incompatible element-enriched component with $\Delta 7/4 > 0$ (old HIMU type) is prominent in the young volcanic rocks (0·3–0·1 Ma). The EM1 component that is important in the southern Cape Verde Islands appears to have played no role in the petrogenesis of the Santo Antão magmas. The primary magmas are argued to be derived by partial melting in the Cape Verde mantle plume; temporal changes in composition are suggested to reflect layering in the plume conduit.

KEY WORDS: *radiogenic isotopes; geochemistry; mantle melting; Cape Verde*

INTRODUCTION

It is widely recognized that the mantle source of hotspot volcanism is complex, and that the volcanism is caused by decompression melting in rising mantle plumes. A number of workers have proposed that plumes may be zoned or change composition with time, e.g. Hawaii (Kurz *et al.*, 1995; Hauri *et al.*, 1996; Lassiter *et al.*, 1996; Abouchami *et al.*, 2000; DePaolo *et al.*, 2001; Mukhopadhyay *et al.*, 2003), Iceland (Hards *et al.*, 1995; Fitton *et al.*, 1997; Chauvel & Hémond, 2000; Holm *et al.*, 2000; Kempton *et al.*, 2000) and the Galapagos (Hoernle *et al.*, 2000). Understanding the geochemical heterogeneities of intraplate volcanism is fundamental to the understanding of mantle convection.

*Corresponding author. Telephone: +45 3532 2426. Fax: +45 3532 2440. E-mail: paulmh@geol.ku.dk

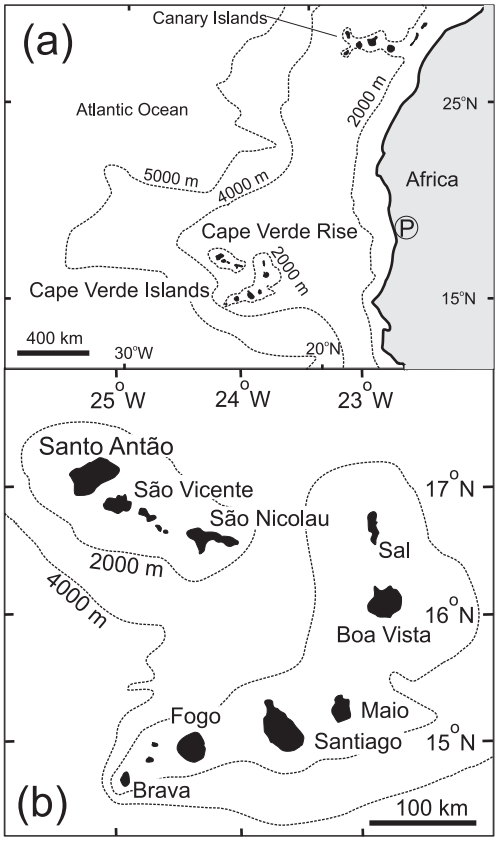

Fig. 1. Maps of (a) the location of the Cape Verde Islands with respect to the coast of western Africa and the Cape Verde Rise; (b) the Cape Verde archipelago. Pole of rotation for the African plate (P) is from Pollitz (1991).

The extreme range of isotopic variation in the most primitive mafic igneous rocks within the Cape Verde islands (e.g. Gerlach *et al.*, 1988) indicates that this hotspot may be useful further to constrain the mantle processes which lead to hotspot volcanism and the nature of mantle plumes. The Cape Verde hotspot (Fig. 1) is virtually stationary relative to the lithosphere, as it is situated close to the rotational pole of the slowly moving African plate (Pollitz, 1991). This setting allows the study of interactions between the plume and the overlying lithosphere without the complication of plate movement. Igneous activity related to the Cape Verde hotspot began at least 19 Myr ago (Duncan & Jackson, 1977; Mitchell *et al.*, 1983) and, therefore, it should be possible to evaluate the changing nature of plume–lithosphere interactions and to test competing hypotheses of whether the parental magmas are derived from the convecting mantle (Gerlach *et al.*, 1988; Davies *et al.*, 1989; Hart *et al.*, 1992; Hanan & Graham, 1996; Hofmann, 1997; Thirlwall, 1997) or the lithospheric mantle (Halliday *et al.*, 1995; Chauvel *et al.*, 1997; Class & Goldstein, 1997). Furthermore, the mantle source volumes for small degrees of melting under old, thick oceanic lithosphere may, potentially, be minor and adequate for high-resolution modelling of mantle composition. The complexity of the Cape Verde mantle plume may, therefore, be tested. Previous studies of the volcanic rocks of the Cape Verde archipelago have revealed a strong contrast between the southern islands, characterized by an EM1-type mantle source component, and the northern islands, which have greater affinity to HIMU (Gerlach *et al.*, 1988; Davies *et al.*, 1989; Christensen *et al.*, 2001; Jørgensen & Holm, 2002). The presence of carbonatites on five of the 10 major islands is a unique feature of Cape Verde, suggesting that the mantle source is CO_2-rich.

To constrain magma generation processes in the Cape Verde archipelago, we have investigated the westernmost of the northern islands, Santo Antão; this island has not previously been studied in detail (Bebiano, 1932; Gerlach *et al.*, 1988; Christensen *et al.*, 2001). We present volcanological, age and petrographical information as well as new major and trace element analyses and Sr–Nd–Pb isotope data (329 samples have been studied). These data are used to characterize the igneous evolution of the island and to provide a basis for modelling plume–lithosphere interactions. Systematic changes with time in the most primitive magma compositions on Santo Antão indicate that melt generation took place in a region of geochemically heterogeneous convecting mantle and that the lithospheric contribution to the melts was insignificant. We propose that changes in the composition of the most primitive magmas with time are related to layering in the plume and that a succession of layers yielded melts as they rose under the island. Lateral variations in the plume may explain inter-island compositional variations between the northern and southern chains of the Cape Verde archipelago, and perhaps even on the scale of individual neighbouring islands.

THE GEOLOGICAL SETTING OF THE CAPE VERDE ISLANDS

The Cape Verde Islands (4033 km^2) consist of 10 major and several smaller islands located 500–800 km west of Africa (Fig. 1a). They are situated SW of the Cape Verde Plateau and 200 km from the centre of the Cape Verde Rise (McNutt, 1988), which covers an area $>3 \times 10^5$ km^2 and is considered to represent a hotspot swell (Crough, 1978). Jurassic–Cretaceous sea-floor constitutes the basement for the islands (Hayes & Rabinowitz, 1975) and was intruded in early Miocene times (19 Ma) by tholeiitic sills, which are suggested to mark the initiation of Cape Verde magmatism (Duncan & Jackson, 1977; Natland, 1977). The N–S oriented Sal–Maio ridge is bounded to the east by large-displacement, N–S-trending, normal faults (Dash *et al.*, 1976). The sea-floor has very steep gradients to depths of several kilometres north of Santiago and east

of São Nicolau (Fig. 1). This may be related to lithospheric fracture zones, indicating that eruption sites for mantle melts are partly governed by deep faults. The Jurassic ocean floor is exposed on Maio and Santiago (De Paepe *et al.*, 1974; Gerlach *et al.*, 1988). Submarine Neogene lavas are found up to 400 m above the present coastline on several islands (Serralheiro, 1976; our unpublished data). These features demonstrate large local vertical movements in the lithosphere. Prior to initiation of volcanic activity, the sea-floor was covered by sediments (silt, clay and shale) which decreased in thickness towards the west from >1000 to <500 m. From early Miocene times, sediments, volcanic ash and mass wasting products from the islands were deposited around the islands in a flexural moat (Ali *et al.*, 2003).

Age determinations on several islands (Mitchell *et al.*, 1983; Plesner *et al.*, 2002; Holm *et al.*, unpublished data) suggest that most of the volcanic activity took place from 16 Ma until the present. Fogo may be entirely Quaternary and Maio relatively old (≥12–7 Ma), whereas Santo Antão (7·5–0·1 Ma), São Vicente (7–0·3 Ma), Santiago (6–0·3 Ma) and Sal (16–1 Ma) developed over extended periods. The greatests amount of young (≤0·5 Ma) volcanism is present on the western islands of Santo Antão and Fogo, as is evident from their immature morphology and age determinations. With recent (0·1–1 Ma) volcanism on several islands, and the oldest dated rock on Santo Antão only surpassed by rocks on Sal and Maio, there is not a simple age progression related to the geographical position of the islands.

The Neogene volcanic rocks consist of a large spectrum of eruption products with lavas being by far the most abundant. All the volcanic rocks are silica-undersaturated with basanites–tephrites and nephelinites representing the dominant lithologies. Phonolitic rocks constitute a few per cent of the total volcanic section. Small carbonatite intrusions are present on São Vicente, Maio, Santiago, Fogo and Brava.

Santo Antão

The geology of the 770 km^2 island of Santo Antão (Fig. 2) was investigated by Bebiano (1932), who identified a wide variety of rock types. The island is almost entirely of subaerial volcanic origin, dominantly built up of large shields of gently seaward-dipping lavas, stratovolcanoes with numerous lateral vents, and hundreds of monogenetic scoria-cones. Strombolian to Hawaiian eruption products are typical and created the basic morphology of the island. Volcanoclastic fluviatile sediments and lahars occur locally, and are widespread in the Chã de Morte depression and SE towards the coast. Very minor amounts of aeolian sediments occur in the north. Most of the central part of the island is more than 1300 m asl. This highland is dissected, mainly to the N and NE, by deep gorges and steep valleys. The southern part of the island is covered by young volcanic products and is less deeply dissected.

The evolution of Santo Antão can be divided into three phases. We refer to these as the Older, Intermediate and Young Volcanic rocks (Fig. 2). In addition to field relations and age determinations, part of the grouping of the younger rocks has been based on geochemistry.

Older Volcanic rocks

The Older Volcanic rocks (OV) make up large parts of the island and constitute the bulk of its volume. Ages of 7·5 and 5·2 Ma have been obtained, but most of the succession is 3–2 Ma old (Plesner *et al.*, 2002; Holm *et al.*, unpublished data). A dyke swarm running SW–NE is exposed in the central Chã de Morte area and along the northern Ribeira Grande valley and represents part of the feeder system for the OV. Rocks older than 7·5 Ma probably exist below the present level of erosion and probably make up much of the submarine pedestal of the island. According to our calculations, the unexposed subaerial part and its submarine pedestal may represent around 50% of the total erupted mass for Santo Antão. The OV partly consist of a large volcanic complex centered near Chã de Morte and extending to the Escabecada, Tarrafal and Agua Nova valleys, where the lava successions have been sampled. The rest of the OV was sampled in the Chã de Igreja valley and at Fontainhas (Fig. 2).

Intermediate Volcanic rocks

This volcanic phase is divided into five groups. The volcanic complex in the Cova–Corda–Paul area (1·4–0·7 Ma) constitutes the COVA group. In the western part of the Chã de Morte depression, an edifice was built on the eroded Chã de Morte volcano; this comprises the Bordeira (BOR) group (2–1 Ma). A new fissure system opened parallel to, and SE of, the earlier (OV) dyke swarm, feeding the Cadela (CAD) volcanic rocks (0·7–0·3 Ma) that mainly erupted in the central highlands. The Sinagoa volcano also belongs to this group and was probably situated at the NE end of the fissure system at this time. In the west, the Agua Nova (AN) volcanic rocks were erupted between 0·5 and 0·3 Ma, at about the same time that the Monte Frado (FRA) volcano erupted further to the south (0·5–0·4 Ma).

Young Volcanic rocks

Volcanism younger than about 0·4 Ma is divided into four groups: YTAR, PRC, COROA and LAGOA. The volcanic rocks in the Tarrafal area and to the NE constitute the YTAR (0·4–0·2 Ma) (young Tarrafal) group. In the western Tope de Coroa area, magmas were erupted through numerous aligned sets of SW-NE-trending fissures. The proto Coroa (PRC) group outcrops around Tope de Coroa (0·4–0·2 Ma), and is partly covered by

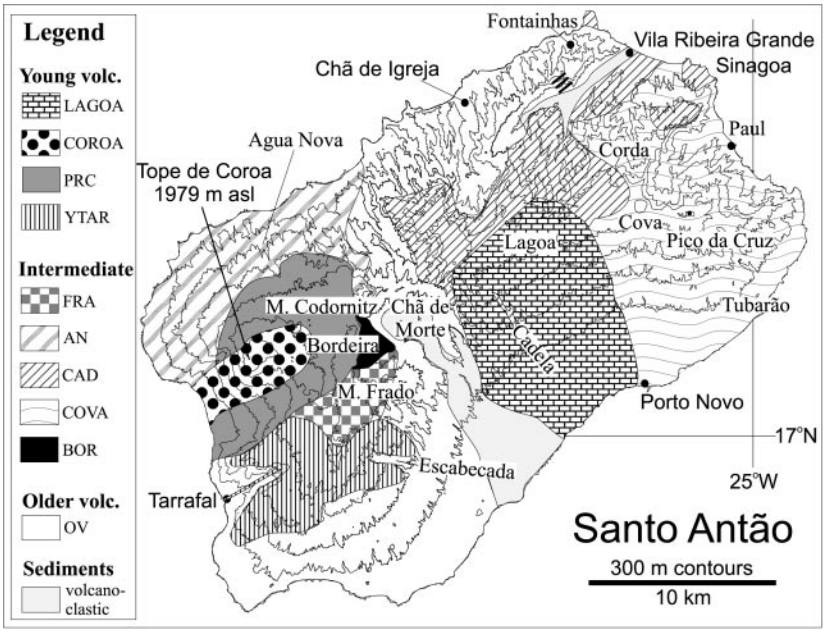

Division of the volcanic formations of Santo Antão, Cape Verde Islands

Age (Ma)*	Group name	N~	Major sample locations and profiles	Rock type+	Symbol°
Older Volcanics:					
7.5 - 2	OV	75	Escabecada valley, Tarrafal valley, Chã de Morte depression/N wall, Chã de Igreja valley, Fontainhas	Bas	◇
	EOV	4	Enriched Old Volcanics: Lower Agua Nova gorge	Bas	□
Intermediate volcanics:					
2 - 1	BOR	13	Chã de Morte/W wall to Bordeira	Neph	⊕
1.4 - 0.7	COVA	73	Cova-Corda road, NW coast: Vila Ribeira Grande-Paul-Gui	Bas	⊕
0.5 - 0.4	FRA	18	Older surface cones and flows, mainly from W & S Santo Antão, Monte Frado	Bas	▽
0.5 - 0.3	AN	15	Younger Agua Nova gorge	Bas	△
0.7 - 0.3	CAD	29	Cadela valley, old volcanics of the Lagoa area, Sinagoa	Neph/ bas	⊠
Young volcanics:					
0.4 - 0.2	PRC	29	Scoria cones and lavas mainly N & E of Tope de Coroa (Proto Coroa)	Neph	■
0.4 - 0.2	YTAR	19	Young Tarrafal: upper valley profile and plain	Neph	▲
0.2	Cão Grande phonolite	7	Plinian pumice mainly on western Santo Antão with two successions: CG1 & CG2	Neph	▼
0.2 - 0.17	COROA	30	Tope de Coroa complex	Neph	★
0.4 - 0.10	LAGOA	15	Lagoa area to Pico de la Cruz	Neph	●

Fig. 2. Simplified geological map of Santo Antão and the correlation between age and volcanic groups. *All ages are from Plesner *et al.* (2002) or our unpublished data (i.e. bottom of Cadela profile: 0·7 Ma, bottom of Tarrafal profile: 5·2 Ma); ~number of analysed samples from group; +Bas-group dominated by basanite–phonolite series rocks; Neph-group dominated by nephelinite–phonolite series rocks; °symbols used in ensuing figures.

lavas of the central volcanic COROA complex (0·20–0·17 Ma). The other main site for young volcanism is the LAGOA fissure system (0·4–0·10 Ma) in the central part of the island forming several aligned sets of scoria cones over the most recent fissures in the central highlands. Lavas from these areas, including the youngest lava on Santo Antão, descended the SE slopes and reached the coast W of Porto Novo (Fig. 2).

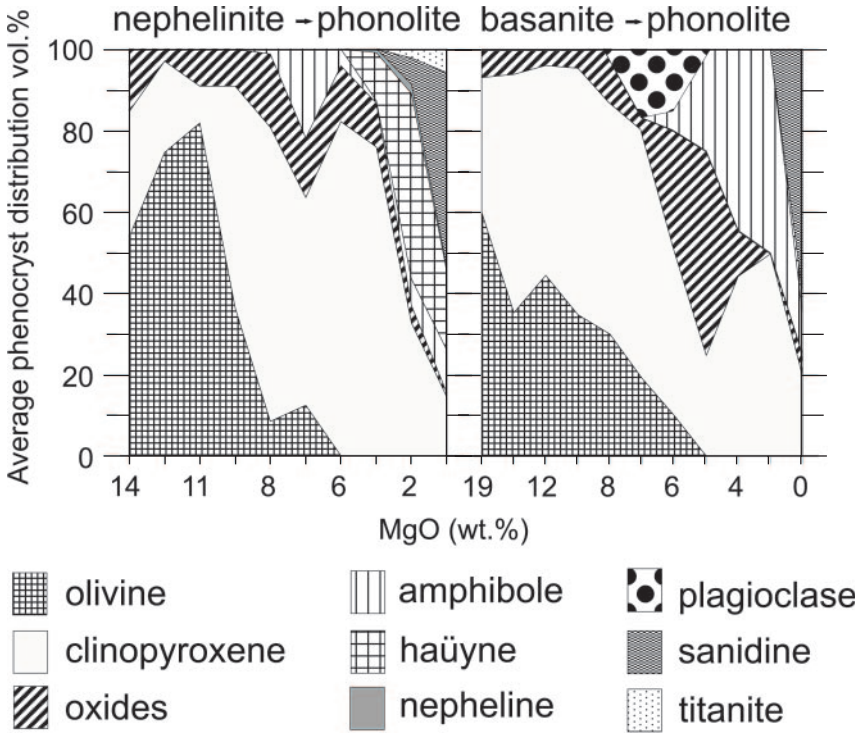

Fig. 3. Average phenocryst content, as a percentage of total number of phenocrysts in the two main magma series of Santo Antão, based on 261 thin sections. Clinopyroxene phenocrysts are present in almost all rocks, except for a few picritic samples, and most rocks have oxide phenocrysts. Oxide is chromite or titanomagnetite, amphibole is kaersutite–pargasite. Plagioclase phenocrysts are present only in 20% of the tephrites.

The LAGOA (and earlier CAD) magmas dominantly flowed towards the SE, giving rise to a youthful morphology on this side of the island. The NW and SE coastlines have migrated towards the SE. A major Plinian eruption at 0·2 Ma resulted in deposition of the phonolitic Cão Grande pumice (Mortensen *et al.*, in preparation) from a vent which was centered just south of the Coroa complex but has since been buried by younger volcanic rocks. The pumice consists mainly of two layered sequences (CG1 and CG2). CG1 can be traced over most of the island and serves as a valuable marker below the most recent volcanic products.

The bulk of the island is built of lava flows. Pyroclastic rocks, mainly lapilli and bombs, are commonly prominent near the main eruption centres. A few ignimbrites have been observed locally but the Cão Grande phonolitic pumice (CG1) is by far the most voluminous deposit from a single eruption.

PETROGRAPHY OF THE VOLCANIC ROCKS

Rock types by modal composition and mineralogy

The volcanic rocks have been divided into a nephelinite–phonolite series and a basanite–phonolite series on the basis of their geochemical characteristics. These are referred to as the nephelinite and basanite series, respectively. Figure 3 shows the average distribution of phenocryst phases in members of the two series based on visual estimation.

Most of the lavas contain clinopyroxene ± olivine ± Fe–Ti oxide phenocrysts in aphanitic to glassy matrices. The lavas show considerable variations in phenocryst content from almost aphyric to rocks with >50% phenocrysts. The phenocryst content generally decreases with increasing magmatic differentiation from around 20 vol. % (range: 5–55) in the most primitive samples to 5 vol. % (range <1–20) in the most evolved. Petrographic studies reveal complex crystallization histories with reverse zonation in some clinopyroxenes in many of the lavas in which Fe-rich green or Ti-rich purple cores have light-coloured diopsidic rims. Picritic and ankaramitic lava types constitute around 10 and 20% of the lavas, respectively; these commonly contain small chromite phenocrysts. Phonolitic rocks contain abundant aegirine–augite phenocrysts with minor amounts of one or more of magnetite, haüyne, titanite and sanidine. Compositionally intermediate rock types (8–3% MgO) have phenocrysts of Ti-rich clinopyroxene, titanomagnetite, amphibole, ± olivine, ± haüyne, ± plagioclase. Many of the lavas carry xenoliths of cumulate rocks derived from subvolcanic magma chambers; some of the primitive lavas contain nodules of mantle peridotite.

Clinopyroxene is present in all rock types, except a few picrites, and is generally the most abundant phase in the most primitive rock types, except when exceeded by olivine in the nephelinites. When present, reversely zoned clinopyroxenes usually constitute only a small proportion of the clinopyroxene population. The colour of the clinopyroxene in thin section varies with its Fe/Mg ratio from pale brown diopside through brownish-purple, Ti-rich intermediate salitic types to green, pleochroic acmitic salites. Zoning is commonly very complex with resorbed cores and is of oscillatory or hourglass type. Not uncommonly, clinopyroxene generations with both reversely zoned brownish-purple rims around green cores, and brownish-purple rims with pale brown cores are present in the same rock. Chromite is present in rocks with ≥12% MgO (and in one sample, with 8% MgO), whereas olivine occurs only in rocks with >6% MgO. Olivine is optically homogeneous and commonly has embayed rims; replacement with iddingsite is very rarely complete. Titanomagnetite occurs in the entire range of rock types but is most abundant in samples with 3–7% MgO. Amphibole is common in the intermediate members but rare in the most evolved (<3% MgO) members of the nephelinite series; it becomes increasingly common in the evolved rocks of the basanite series. Most amphiboles have decomposed to aggregates of Fe–Ti oxide crystallites, but are otherwise strongly pleochroic (brown to red–brown) and commonly show complex zonation. Plagioclase is only a common phenocryst phase in 20% of the tephrites (with 5–7% MgO) within the basanite series rocks, some phonolites, and a few primitive rocks. Oscillatory zonation is common in plagioclase that is sometimes overgrown by sanidine. Haüyne phenocrysts, forming clear blue to colourless equant crystals, typically with a black reaction rim, are common (up to 10 vol. %) in the nephelinite series in rocks with <5% MgO. Trace amounts of haüyne also occur in some phonolites of the COVA group of intermediate age which belong to the basanite series. Apatite is a common accessory in rocks of intermediate composition. Minor amounts of titanite occur in intermediate to evolved rocks with MgO < 7% and biotite is rare, occurring only in trace amounts in some phonolites (e.g. the COVA group).

ANALYTICAL METHODS

Sample preparation

Samples of 1–2 kg were prepared and analysed (unless otherwise indicated) at the Geological Institute, University of Copenhagen. To remove secondary alteration associated with the presence of caliche, specimens were initially leached with cold 0·1 M (or slightly stronger) HCl overnight and dried at 40°C. Subsequently, jaw-crushed material was used for Pb isotope analyses or crushed to fine powder (<10 μm) in an agate swing mill (for major and trace element and Nd–Sr isotopic analysis).

Whole-rock major and trace element analysis

Major elements were analysed at the Geological Survey of Denmark and Greenland (GEUS) by X-ray fluorescence (XRF) using a Philips PW1606 instrument; volatile contents were estimated based on loss on ignition (weight loss 110–1000°C) corrected for the oxidation of Fe. Na was analysed by flame photometry and Fe^{2+} by titration (Kystol & Larsen, 1999). The analytical precision of the data is (1σ, abs. wt %): SiO_2: 0·15; TiO_2: 0·015; Al_2O_3: 0·05; $Fe_2O_3^{total}$: 0·1; FeO: 0·1; MnO: 0·003; MgO: 0·05; CaO: 0·03; Na_2O: 0·05; K_2O: 0·005; P_2O_5: 0·005; volatiles: 0·10%.

Trace elements were analysed by XRF on pressed powder pellets using a Philips PW 1400 instrument. The international standards G-2, GSP-1, AGV-1, W-1, BCR-1, PCC-1 and DTS-1 were used for calibration and AGV-1 as monitor (Table 1).

A subset of 60 samples was analysed by instrumental neutron activation analysis (INAA) using a Ge detector on a multi-channel analyser at the Geological Institute (R. Gwozdz, Tracechem) on 100 mg powder irradiated at the Danish Nuclear Research Reactor at Risø. Iron was used for calibration and the analytical quality monitored by BHVO-1 (Appendix A).

Another subset of 40 samples was analysed by ICP-MS at GEUS. Calibrations were based on synthetic standards and BHVO-1, BIR-1 and GH. The international standards BE-N and BCR-1 were used to monitor the analytical quality, and were dissolved and analysed along with the samples (Appendix A).

Precision and detection limits for the analysed elements and analyses of standard materials are given in Table 1. Incompatible trace element levels are, in general, relatively high and analytical uncertainties low: e.g. La, Zr and Nb 2σ ~4% for typical concentrations, and 2σ(La/Nb) ≈ 0·03 and 2σ(Zr/Nb) ≈ 0·3.

In the subsequent discussion, XRF results are plotted for the elements Sc, V, Cr, Co, Ni, Cu, Zn, Ga, Rb, Sr, Y, Zr, Nb, Y, Ba, La, Ce, Nd, Pb and Th for consistency. For other trace elements, ICP-MS analyses are preferred to INAA when both are available (for Cs, REE, Hf and Ta).

Mineral compositions

Mineral analyses were performed on polished thin sections using a fully automated JEOL 733 electron microprobe at the Geological Institute, University of Copenhagen, and the Department of Earth Sciences,

Table 1: Major and trace element concentrations in selected volcanic rocks from Santo Antão

Sample:	106454	111753	109965	109564	111750	111743	111757	111822	111762	111756	111748	111751	114531
Group:	OV	OV	OV	OV	OV	OV	OV	OV	OV	OV	OV	OV	OV
SiO_2 wt %	42·99	42·54	42·41	43·62	42·77	44·98	41·81	43·85	42·07	45·16	43·75	43·02	43·71
TiO_2	3·34	3·15	2·99	3·83	4·05	3·68	4·37	3·79	4·32	3·54	4·19	4·92	4·42
Al_2O_3	8·60	8·04	7·82	10·71	12·01	10·42	11·75	12·62	12·53	13·08	13·31	14·46	15·12
$Fe_2O_3^{cor}$	3·42	3·24	3·64	3·42	3·59	3·51	3·77	3·62	3·69	3·30	3·64	3·61	3·24
FeO^{cor}	8·33	7·89	8·84	8·32	8·73	8·53	9·17	8·80	8·97	8·02	8·85	8·79	7·88
MnO	0·17	0·18	0·19	0·18	0·20	0·18	0·20	0·19	0·20	0·18	0·19	0·20	0·22
MgO	17·46	16·73	15·64	12·18	12·17	12·16	12·15	9·56	9·19	8·89	8·60	7·08	6·17
CaO	13·06	14·62	14·62	13·10	11·74	13·34	12·15	12·96	14·39	13·01	13·21	12·67	11·75
Na_2O	1·02	1·73	1·01	2·58	2·25	1·70	3·19	2·13	2·32	2·36	2·67	2·70	4·22
K_2O	0·44	0·37	0·55	0·57	1·13	0·80	0·56	1·24	1·00	1·36	0·69	1·13	1·16
P_2O_5	0·42	0·56	0·65	0·59	0·62	0·49	0·72	0·58	0·81	0·52	0·58	0·95	1·19
Total	99·24	99·03	12·10	99·12	99·26	99·79	99·84	99·34	99·48	99·42	99·69	99·54	99·07
$Fe_2O_3^{measured}$	4·84	5·35	13·17	4·91	5·06	4·61	3·69	4·92	4·70	5·27	4·48	4·83	5·15
$FeO^{measured}$	7·47	6·08	1·40	7·27	7·54	7·65	9·36	7·77	8·21	6·41	8·25	7·91	6·50
FeO^{total}	11·83	10·90	12·10	11·69	12·09	11·80	12·68	12·19	12·44	11·15	12·28	12·26	11·14
Volatiles	3·37	0·68	7·42	2·32	0·91	0·82	0·94	0·97	1·17	1·21	1·20	1·71	2·96
Rb ppm	15	13	10	28	29	13	19	28	24	26	27	29	37
Ba	284	416	449	386	595	325	521	441	464	429	420	667	794
Pb	5	3	1	3	1	3	3	4	3	4	4	5	5
Sr	485	673	616	733	806	477	863	844	919	705	798	1145	1400
Y	21	25	24	26	29	21	31	30	34	25	32	39	41
Zr	192	198	193	239	278	185	307	263	343	226	320	412	420
Nb	44	63	57	63	74	43	80	68	79	61	74	114	122
Zn	97	111	106	115	97	135	119	143	109	133	141	127	138
Cu	45	56	104	76	59	83	103	95	96	96	71	40	62
Co	75	72	87	77	68	60	60	52	52	50	54	46	40
Ni	494	427	572	365	315	234	296	201	160	136	146	72	63
Sc	35	46	28	34	30	39	30	30	33	33	29	29	12
V	306	296	212	341	371	377	375	395	397	331	416	429	310
Cr	1237	1134	914	766	695	682	639	401	356	372	273	97	129
Ga	16	18	16	20	20		20	22	24				23
La	29	52	43	42	46	36	51	49	58	40	45	78	95
Ce	66	108	95	88	105	75	114	103	125	85	102	162	190
Pr								**12·04**					**20·27**
Nd	36	54	46	48	53	43	58	52	65	44	55	80	93
Sm		*9·00*		*0·00*	*9·00*	*9·00*	*11·00*	**10·06**		*10·00*	*11·00*	*17·00*	**14·62**
Eu		*3·00*		*2·75*	*3·00*	*2·70*	*3·30*	**3·01**		*2·70*	*3·10*	*4·90*	**4·33**
Gd								**9·73**					**14·09**
Tb		*1·10*		*1·20*	*1·30*	*1·10*	*1·40*	***1·29***		*1·30*	*1·30*	*2·10*	**1·80**
Dy								**6·68**					**9·16**
Ho								**1·08**					**1·44**
Er								**2·92**					**3·94**
Tm								**0·35**					**0·48**
Yb		*1·80*			*1·90*	*1·70*	*2·10*	**2·14**		*2·00*	*2·40*	*3·30*	**2·89**
Lu		*0·23*		*0·18*	*0·31*	*0·24*	*0·29*	**0·29**		*0·26*	*0·34*	*0·44*	**0·39**
Cs				*0·40*				**0·22**					**0·56**
Hf		*6·00*		*6·00*	*7·00*	*6·00*	*7·00*	**6·77**		*6·00*	*8·00*	*11·00*	**9·54**
Ta		*3·70*		*3·92*	*4·70*	*3·30*	*4·70*	**3·37**		*3·60*	*4·70*	*7·70*	**5·68**
Pb		**2·27**			**2·25**	**1·63**	**2·54**	**2·59**		**2·03**	**1·94**	**4·38**	**5·96**
Th	*4·5*	*3·6*		*3·0*	*4·0*	*3·0*	*5·0*	*5·0*	*6·3*	*5·0*	*4·0*	*9·0*	*10·1*
U		**1·2**			**0·9**	**0·7**	**1·0**	**1·1**		**1·2**	**1·0**	**1·9**	**2·5**

Table 1: continued

Sample:	111745	109521	109957	109527	109962	106453	109952	114528	114533	109901	109994	109995	109997
Group:	OV	OV	OV	OV	OV	OV	OV	EOV	EOV	BOR	BOR	BOR	BOR
SiO_2 wt %	45·17	43·61	43·47	44·64	45·72	44·06	49·03	42·15	43·19	39·42	39·12	43·38	50·35
TiO_2	4·70	4·86	4·81	4·30	4·49	4·23	3·45	4·54	4·23	6·23	5·26	4·11	2·62
Al_2O_3	14·63	14·64	15·52	15·70	16·20	16·80	18·23	12·93	13·28	12·27	12·10	15·90	18·98
$Fe_2O_3^{cor}$	3·71	3·53	3·24	3·08	3·00	2·93	3·06	3·55	3·40	3·69	3·85	3·07	2·87
FeO^{cor}	9·02	8·60	7·87	7·49	6·88	6·47	5·39	8·63	8·28	8·99	9·36	7·46	4·07
MnO	0·19	0·16	0·22	0·21	0·20	0·23	0·18	0·21	0·21	0·17	0·19	0·23	0·22
MgO	5·89	5·82	5·35	5·23	4·92	4·79	3·65	8·78	8·74	10·35	8·18	5·31	2·47
CaO	11·56	12·22	11·70	11·02	11·04	12·12	8·59	13·11	12·53	11·96	15·88	11·89	7·05
Na_2O	2·71	2·59	3·56	4·32	4·41	4·44	4·01	3·33	3·09	4·08	3·04	4·61	5·97
K_2O	1·62	1·27	2·14	1·23	1·24	0·97	2·57	0·90	0·80	0·94	0·99	1·71	3·75
P_2O_5	0·73	0·84	1·00	1·19	1·20	1·37	0·84	1·08	1·15	0·97	0·76	1·19	0·63
Total	99·93	98·15	98·87	98·40	99·30	98·42	98·99	99·20	98·91	99·05	98·71	98·85	98·97
$Fe_2O_3^{measured}$	4·76	9·48	4·52	6·81	4·73	5·70	6·34	6·76	5·39	4·73	6·67	4·10	4·70
$FeO^{measured}$	8·18	3·56	7·00	4·40	5·68	4·74	2·73	6·01	6·80	8·22	7·06	6·91	2·55
FeO^{tot}	12·46	12·10	11·07	10·53	9·94	9·53	8·44	12·09	11·65	12·48	13·06	10·60	6·78
Volatiles	0·70	2·04	2·44	2·22	3·42	4·16	3·14	1·97	2·47	1·27	1·55	3·47	1·64
Rb ppm	33	39	44	33	58	68	90	32	43	38	21	58	95
Ba	523	606	849	807	728	1024	1436	675	711	928	548	919	1091
Pb	4	3	5	6	6	7	8	5	6	7	7	7	9
Sr	888	1053	1427	1404	1351	1461	1731	1248	1184	1749	1093	1716	1606
Y	33	34	39	39	41	45	44	40	39	39	31	40	30
Zr	327	363	376	469	459	461	590	392	344	589	307	428	548
Nb	82	104	121	140	131	169	176	111	137	148	75	139	125
Zn	133	119	134	119	122	143	134	128	135	108	124	114	130
Cu	97	93	50	41	19	28	81	112	50	132	48	20	91
Co	47	58	55	44	41	28	39	48	68	53	68	47	24
Ni	52	70	33	38	35	6	13	138	157	31	100	31	5
Sc	24	23	9	13	11	3	6	25	20	13	35	8	3
V	472	407	314	333	308	–	241	339	308	345	428	331	238
Cr	26	36	16	51	19	–	15	321	274	62	185	36	7
Ga	–	26	29	26	28	–	30	24	24	32	28	28	31
La	58	69	76	86	80	106	103	87	88	96	56	87	84
Ce	125	141	168	170	173	211	206	182	182	208	123	177	150
Pr		15·95		19·87	19·81		21·86	18·50			13·81	20·82	15·88
Nd	65	71	78	83	82	94	91	86	86	89	66	82	56
Sm	*12·00*	**12·31**		**13·75**	**14·31**		**14·59**	**13·79**	*15·00*		**11·51**	**14·48**	**9·12**
Eu	3·60	**3·63**		**4·12**	**4·22**		**4·30**	**4·07**	*4·40*		**3·45**	**4·24**	**2·63**
Gd		**11·94**		**13·47**	**13·97**		**14·70**	**13·27**			**10·93**	**14·10**	**9·53**
Tb	*1·50*	**1·55**		**1·70**	**1·81**		**1·85**	**1·69**	*1·80*		**1·42**	**1·76**	**1·15**
Dy		**7·70**		**8·58**	**9·14**		**9·31**	**8·61**			**7·03**	**8·96**	**5·82**
Ho		**1·24**		**1·39**	**1·45**		**1·52**	**1·39**			**1·11**	**1·45**	**0·99**
Er		**3·33**		**3·74**	**3·89**		**4·19**	**3·75**			**2·86**	**3·97**	**2·95**
Tm		**0·38**		**0·45**	**0·47**		**0·52**	**0·43**			**0·34**	**0·47**	**0·39**
Yb	*2·50*	**2·31**		**2·72**	**2·88**		**3·24**	**2·64**	*2·60*		**1·98**	**2·92**	**2·53**
Lu	*0·33*	**0·32**		**0·39**	**0·40**		**0·45**	**0·36**	*0·36*		**0·28**	**0·40**	**0·37**
Cs		**0·61**		**1·25**	**0·88**		**0·79**	**0·43**			**0·31**	**0·77**	**0·69**
Hf	*8·00*	**8·77**		**10·16**	**10·52**		**12·27**	**8·87**	*7·00*		**8·48**	**8·87**	**10·12**
Ta	5·10	**5·09**		**6·62**	**6·49**		**7·89**	**5·19**	*7·40*		**3·80**	**6·43**	**4·20**
Pb	**2·20**	**3·32**		**4·63**	**4·09**		**6·17**	**3·51**	**3·42**		**2·62**	**5·37**	**8·03**
Th	*6·0*	*7·3*	*7·2*	*10·4*	*9·1*	*13·8*	*12·3*	*8·8*	*8·5*	*13·6*	*5·9*	*11·6*	*13·2*
U	1·3	1·5		2·2	2·4		2·9	2·2	1·9		1·6	3·3	3·7

Sample:	110062	114816	109558	109502	109557	110033	111768	111840	109556	109508	109563	109545	109546
Group:	COVA	COVA	COVA	COVA	COVA	COVA	COVA	COVA	COVA	COVA	COVA	COVA	COVA
SiO_2 wt %	42·56	42·55	44·14	43·29	42·42	42·34	44·77	42·11	42·51	41·76	44·84	46·14	47·82
TiO_2	3·55	3·67	3·26	4·21	4·36	4·32	3·81	5·10	5·32	4·33	4·01	3·30	3·54
Al_2O_3	10·75	11·84	11·46	11·85	13·66	13·92	13·39	13·29	14·36	13·48	15·67	16·52	18·02
$Fe_2O_3^{cor}$	3·67	3·44	3·21	3·51	3·63	3·45	3·32	3·72	3·62	3·62	3·13	3·07	3·31
FeO^{cor}	8·92	8·37	7·80	8·54	8·83	8·40	8·07	9·04	8·80	8·80	7·62	6·25	5·72
MnO	0·18	0·19	0·18	0·19	0·21	0·19	0·20	0·22	0·22	0·27	0·21	0·20	0·27
MgO	13·27	12·77	11·72	10·14	7·74	7·65	7·53	7·24	6·58	5·99	5·27	4·25	3·56
CaO	12·26	11·48	12·20	12·75	12·01	12·65	11·39	12·29	12·40	11·92	10·66	9·14	9·49
Na_2O	2·25	3·83	3·61	3·26	4·33	2·85	3·93	4·43	3·03	5·14	4·52	6·79	3·42
K_2O	1·17	0·63	0·74	0·69	0·97	1·64	1·83	0·92	0·53	1·66	1·62	2·18	2·39
P_2O_5	0·56	0·66	0·67	0·88	0·78	0·73	0·71	1·13	1·01	1·69	0·91	0·75	1·02
Total	99·13	99·43	98·98	99·32	98·94	98·14	98·95	99·47	98·37	98·66	98·45	98·60	98·54
$Fe_2O_3^{measured}$	3·81	4·71	6·50	5·34	5·81	12·22	8·15	5·00	11·51	6·37	5·89	4·78	5·55
$FeO^{measured}$	8·92	7·37	4·99	7·07	7·04	0·63	4·14	8·02	2·13	6·53	5·41	4·81	4·05
FeO^{tot}	12·30	11·61	10·84	11·87	12·27	11·62	11·47	12·52	12·49	12·26	10·71	9·11	9·04
Volatiles	0·58	1·13	1·09	1·35	1·16	0·16	3·17	1·00	2·71	1·43	2·35	0·90	3·60
Rb ppm	22	38	24	33	33	28	54	14	37		63	44	82
Ba	283	665	633	640	772	345	733	618	559	878	978	1074	1408
Pb	2	5	1	2	3	2	6	2	3	16	3	4	7
Sr	715	1006	941	1063	881	947	940	1098	1116	2042	1404	1425	2783
Y	24	28	27	32	28	30	29	36	34	34	36	34	48
Zr	200	291	279	342	294	282	290	367	369		478	528	742
Nb	50	78	65	86	68	73	74	92	101	202	110	112	195
Zn	119	104	124	99	131	147	139	137	153	130	129	133	141
Cu	64	54	78	58	52	84	69	83		43	44	18	39
Co	92	62	76	82	62	64	40	44	69	53	58	79	26
Ni	328	320	266	198	78	84	84	60	52		24	21	8
Sc	32	22	25	24	23	28	19	22	25	10	13	9	4
V	320	291	288	332	365	335	315	421	371	284	295	228	245
Cr	781	679	673	565	189	195	205	144	57	72	20	19	10
Ga	20	21	19	22	21	24	25	25	26		26	29	30
La	36	60	48	63	55	48	48	63	66	114	77	76	140
Ce	75	113	97	130	122	99	95	139	134	241	147	141	256
Pr	**9·35**	**11·93**		**15·40**	**13·84**	**12·49**			**15·70**	**28·85**	**16·68**		
Nd	40	56	49	67	63	52	48	73	69	116	70	63	105
Sm	**8·59**	**9·36**	*8·91*	**12·09**	**11·83**	**10·46**	*10·00*		**11·96**	**20·78**	**12·53**	*10·60*	*17·40*
Eu	**2·64**	**2·89**	*2·84*	**3·63**	**3·48**	**3·27**	*2·90*		**3·53**	**6·01**	**3·77**	*3·57*	*5·27*
Gd	**8·23**	**9·27**		**11·58**	**11·05**	**10·23**			**11·60**	**19·53**	**12·55**		
Tb	**1·12**	**1·19**	*1·14*	**1·52**	**1·47**	**1·36**	*1·30*		**1·46**	**2·42**	**1·62**	*1·51*	*2·27*
Dy	**5·77**	**6·07**		**7·35**	**7·39**	**6·97**			**7·45**	**11·74**	**8·11**		
Ho	**0·93**	**0·98**		**1·16**	**1·23**	**1·16**			**1·19**	**1·77**	**1·30**		
Er	**2·41**	**2·59**		**3·04**	**3·29**	**3·09**			**3·22**	**4·70**	**3·53**		
Tm	**0·29**	**0·29**		**0·34**	**0·38**	**0·35**			**0·39**	**0·51**	**0·43**		
Yb	**1·69**	**1·82**	*1·83*	**2·10**	**2·30**	**2·24**	*1·90*		**2·34**	**3·15**	**2·56**	*2·27*	*0·49*
Lu	**0·23**	**0·26**	*0·23*	**0·30**	**0·34**	**0·31**	*0·30*		**0·32**	**0·41**	**0·36**	*0·34*	*0·49*
Cs	**0·27**	**0·43**	*0·79*	**0·48**	**0·52**	**0·27**			**0·48**	**0·92**	**0·79**	*1·06*	*2·90*
Hf	**5·63**	**6·64**	*6·24*	**8·33**	**8·26**	**7·21**	*7·00*		**8·79**	**15·54**	**10·87**	*10·80*	*13·80*
Ta	**2·47**	**3·53**	*3·98*	**4·33**	**3·89**	**3·51**	*4·10*		**4·99**	**9·00**	**5·15**	*5·69*	*9·41*
Pb	**1·82**	**3·84**		**2·92**	**3·06**	**1·65**	**3·22**		**2·19**	**5·71**	**4·18**		
Th	*4·1*	*6·5*	*4·2*	*6·6*	*6·1*	*5·5*	*5·8*	*5·4*	*6·9*	*11·9*	*9·3*	*8·1*	*13·4*
U	1·0	1·5		1·6	1·4	1·3	1·3		1·9	3·1	2·6		

Table 1: continued

Sample:	114811	111767	109551	106459	109568	111813	111718	106452	111712	111709	111708	111725	111705
Group:	COVA	COVA	COVA	COVA	COVA	FRA	FRA	FRA	AN	AN	AN	AN	AN
SiO_2 wt %	48·27	49·01	50·91	54·82	58·01	42·88	44·40	44·61	42·59	41·94	42·02	42·62	42·45
TiO_2	2·49	2·50	2·45	1·12	0·65	3·39	4·35	3·04	5·18	5·15	5·35	4·98	4·96
Al_2O_3	18·37	18·55	19·27	20·84	21·76	9·65	10·28	17·12	11·77	12·32	13·28	13·67	14·59
$Fe_2O_3^{cor}$	2·92	3·11	2·80	2·04	1·47	3·41	3·63	3·52	3·66	3·63	3·79	3·57	3·14
FeO^{cor}	4·49	4·40	3·78	2·13	1·44	8·29	8·84	5·15	8·90	8·83	9·22	8·69	7·63
MnO	0·24	0·20	0·21	0·18	0·17	0·19	0·19	0·28	0·18	0·19	0·21	0·20	0·22
MgO	2·87	2·45	2·22	0·80	0·49	13·56	11·14	2·62	8·17	7·74	6·81	6·53	5·26
CaO	7·23	7·04	5·95	3·94	2·27	13·60	13·09	9·33	13·11	12·68	12·87	12·12	11·22
Na_2O	7·38	7·26	7·47	8·25	6·92	2·86	1·36	8·29	4·45	3·60	4·27	3·87	5·99
K_2O	4·00	4·13	3·63	4·85	5·63	0·87	1·03	3·23	0·61	1·88	0·70	2·34	2·64
P_2O_5	0·77	0·47	0·50	0·19	0·10	0·60	0·61	0·77	0·95	0·96	1·25	1·14	1·60
Total	99·03	99·13	99·17	99·16	98·91	99·29	98·92	97·97	99·57	98·92	99·77	99·74	99·70
$Fe_2O_3^{measured}$	4·53	3·61	3·32	2·19	2·95	5·10	7·89	6·05	5·93	10·04	5·65	6·06	4·44
$FeO^{measured}$	3·11	4·06	3·39	2·01	0·16	6·92	5·31	2·97	7·00	3·17	7·78	6·53	6·52
FeO^{tot}	7·18	7·30	6·37	3·98	2·82	11·51	12·41	8·41	12·34	12·20	12·86	11·99	10·51
Volatiles	0·76	1·34	1·13	0·41	1·76	1·14	1·99	0·86	0·99	0·28	1·62	0·42	0·44
Rb ppm	92	106	63	124	133	18	26	60	33	37	39	50	62
Ba	1370	1333	1139	1514	2212	537	534	1060	524	552	754	688	940
Pb	11	4	5	8	6	4	2	8	3	4	5	5	9
Sr	2400	1467	1494	1844	1684	580	709	1882	1003	1033	1429	1354	1810
Y	32		31	31	24	23	30	56	31	36	39	39	51
Zr	632	497	488	612	625	219	281	698	354	414	505	548	618
Nb	148	127	137	147	128	45	59	189	71	82	104	100	146
Zn	122	91	81	95	121	126	165	128	142	141	142	170	143
Cu	17	11	7	2	78	75	8	98	86	67	78	43	48
Co	19	15	37	15	37	63	62	17	50	48	49	41	31
Ni	20	3	4	3	4	248	185	4	99	92	48	46	10
Sc	5	3	2	−1	2	34	43	1	28	27	24	22	9
V	225	169	190	63	38	325	323	285	433	384	419	387	420
Cr	22	6	12	1	0	766	620	5	244	179	91	90	8
Ga	30	28	23	29	27	19	20	30	23	25	26	27	30
La	114	67	93	86	95	36	51	121	61	62	90	80	111
Ce	189	115	177	131	133	79	111	239	128	142	203	183	235
Pr	**17·81**												
Nd	68	48	74	42	30	42	60	104	71	75	104	97	121
Sm	**10·28**	*9·00*			*4·07*	*7·50*	*9·00*		*17·00*	*15·00*		*18·00*	*21·00*
Eu	**3·04**	*2·60*			*1·38*	*2·48*	*3·20*		*4·00*	*4·20*		*5·10*	*5·80*
Gd	**10·90**												
Tb	**1·29**	*1·20*			*0·64*	*0·89*	*1·20*		*1·60*	*1·70*		*2·00*	*2·40*
Dy	**6·72**												
Ho	**1·11**												
Er	**3·19**												
Tm	**0·42**												
Yb	**2·74**	*2·70*				*1·43*	*1·30*		*2·20*	*2·00*		*2·50*	*2·70*
Lu	**0·41**	*0·41*			*0·37*	*0·28*	*0·33*		*0·29*	*0·30*		*0·36*	*0·42*
Cs	**1·27**				*1·88*								
Hf	**10·71**	*11·00*			*10·10*	*5·45*	*7·00*		*9·00*	*10·00*		*13·00*	*12·00*
Ta	**4·50**	*6·70*			*3·78*	*2·69*	*3·50*		*4·40*	*4·70*		*6·00*	*7·60*
Pb	**10·21**	**3·74**					**2·96**		**3·11**	**4·46**	**3·48**	**3·17**	**6·65**
Th	*16·8*	*7·0*	*10·4*	*16·7*	*12·8*	*2·7*	*4·0*	*15·7*	*5·0*	*7·0*	*7·8*	*9·0*	*12·0*
U	6·1	2·2					1·1		1·5	2·8	1·9	2·1	2·9

Sample:	111713	111832	114522	114521	111828	110049	110041	111721	111737	111717	111701	110021	111837
Group:	AN	CAD	CAD	CAD	CAD	CAD	CAD	PRC	PRC	PRC	PRC	PRC	YTAR
SiO_2 wt %	45·45	39·06	38·14	38·13	39·72	40·40	42·17	40·18	40·00	37·98	51·41	58·26	40·33
TiO_2	4·21	3·70	4·10	4·46	5·46	4·12	5·27	5·36	5·32	6·39	1·61	0·74	4·00
Al_2O_3	15·79	8·96	9·44	9·96	11·44	11·71	14·22	11·65	11·41	12·17	19·64	21·27	10·68
$Fe_2O_3^{cor}$	3·09	3·61	3·79	3·84	3·93	3·57	3·70	3·76	3·68	4·20	2·51	1·55	3·65
FeO^{cor}	7·16	8·79	−1·57	9·34	9·56	8·69	8·99	9·15	8·95	10·22	2·91	1·55	8·89
MnO	0·20	0·19	0·21	0·21	0·19	0·20	0·22	0·19	0·18	0·23	0·22	0·18	0·19
MgO	4·83	19·11	14·70	13·56	12·65	11·63	6·10	12·98	12·45	7·87	1·39	0·61	14·01
CaO	9·70	12·57	13·13	13·00	11·93	12·25	11·59	10·59	11·00	13·85	4·78	3·57	11·45
Na_2O	5·20	1·70	2·93	3·41	2·22	3·60	3·22	2·55	3·01	2·74	8·12	8·30	3·72
K_2O	2·60	0·32	1·10	1·24	0·57	0·93	2·28	1·96	2·27	1·77	5·18	2·86	1·56
P_2O_5	1·17	0·74	1·49	1·37	0·90	1·04	1·22	0·79	0·86	1·35	0·30	0·14	0·91
Total	99·40	98·74	87·46	98·53	98·59	98·14	98·98	99·18	99·13	98·77	98·09	99·02	99·40
$Fe_2O_3^{measured}$	7·31	5·59	0·00	10·21	9·35	11·95	6·01	5·29	5·00	8·14	3·42	2·65	4·31
$FeO^{measured}$	3·44	7·40	1·86	3·71	4·91	1·44	7·05	7·94	7·86	6·93	2·17	0·63	8·37
FeO^{tot}	10·01	12·43	12·78	12·89	13·33	12·08	12·46	12·70	12·36	14·25	5·25	3·02	12·25
Volatiles	0·37	2·92	1·54	0·15	1·16	0·59	0·87	1·09	0·70	1·39	1·37	2·21	0·48
Rb ppm	49	12	31	20	23	33	47	45	45	40	104	55	41
Ba	854	581	831	784	627	473	461	685	651	644	1493	1152	701
Pb	5	4	7	4	4	4	4	6	6	7	22	9	6
Sr	1505	815	1686	1580	957	1338	1199	1049	1094	1171	2645	2439	1134
Y	43	23	42	41	31	34	37	36	35	49	43	22	33
Zr	480	219	328	351	290	370	398	478	468	639	1412	835	351
Nb	107	81	113	113	77	98	111	93	92	120	226	114	82
Zn	117	135	130	141	138	147	146	149	171	169	106	131	132
Cu	77	62	66	65	49	56	46	54	55	14	4	69	48
Co	32	71	75	88	64	90	95	66	65	51	7	38	65
Ni	17	523	371	331	284	259	29	268	244	53	4	4	357
Sc	9	29	26	29	30	29	21	28	29	29	0	1	28
V	359	320	252	283	381	295	388	332	400	424	161	66	344
Cr	8	822	619	587	444	424	26	467	474	63	3	3	604
Ga	28	19	19	18	23	24	26	23	25	28	41	29	22
La	82	49	129	120	62	91	73	75	74	107	160	110	72
Ce	176	95	254	249	138	166	157	157	160	226	238	163	147
Pr		12·44				19·53						15·94	16·80
Nd	90	48	115	115	67	80	81	78	81	119	75	46	74
Sm	*17·00*	**9·62**		*18·80*		*14·13*	*14·50*		*14·00*	*17·00*	*13·00*	*6·62*	13·03
Eu	*4·30*	***2·88***		*5·45*		*4·09*	*4·50*		*4·40*	*5·90*	*3·50*	*1·85*	3·75
Gd		**9·27**				**13·62**						**7·83**	**12·38**
Tb	*1·80*	**1·18**		*2·09*		*1·66*	*2·03*		*1·70*	*2·40*	*1·60*	**0·81**	**1·55**
Dy		**5·65**				**8·30**						**4·29**	**7·61**
Ho		**0·87**				**1·28**						**0·78**	**1·19**
Er		**2·18**				**3·42**						**2·40**	**3·15**
Tm		**0·24**				**0·39**						**0·35**	**0·35**
Yb	*2·90*	**1·39**		*2·43*		**2·38**	*3·17*		*2·40*	*2·50*	*4·20*	**2·45**	**2·09**
Lu	*0·40*	**0·19**		*0·35*		**0·34**	*0·39*		*0·31*	*0·37*	*0·68*	**0·40**	**0·29**
Cs		**0·24**		*0·41*		**0·61**	*0·44*					**1·20**	**0·48**
Hf	*10·00*	**5·73**		*8·19*		**8·74**	*9·20*		*11·00*	*15·00*	*23·00*	**14·41**	**8·38**
Ta	5·20	**3·81**		6·02		**4·21**	7·12			*7·20*	*6·10*	**2·98**	**3·67**
Pb	**4·34**	**2·25**				**2·64**			**3·12**	**4·06**	**27·07**	**15·08**	**4·18**
Th	*9·0*	*5·3*	*13·1*	*9·9*	*5·5*	*11·6*	*5·3*	*7·5*	*8·0*	*9·5*	*35·0*	*17·4*	*8·4*
U	1·9	1·4				2·9			2·0	2·3	9·3	5·1	2·1

Table 1: continued

Sample:	111764	111763	106456	111759	106455	110029	110028	110026	110030	110052	106457	111940	111827
Group:	YTAR	YTAR	YTAR	YTAR	YTAR	CORA	COROA	COROA	COROA	LAGOA	LAGOA	LAGOA	LAGOA
SiO_2 wt %	38·57	38·61	40·45	49·91	57·75	39·49	41·38	44·98	45·70	39·92	39·67	40·05	40·40
TiO_2	4·56	4·63	4·84	2·25	0·29	5·91	5·28	3·97	3·65	5·29	5·40	5·30	5·23
Al_2O_3	10·41	10·58	11·81	19·00	22·35	12·76	14·65	15·97	16·51	11·46	11·82	11·93	11·66
$Fe_2O_3^{cor}$	3·87	3·91	3·56	3·01	0·97	3·79	3·11	3·30	3·13	3·71	3·94	3·80	3·77
FeO^{cor}	9·40	9·52	8·65	3·74	0·93	9·23	7·57	6·44	5·60	9·02	9·58	9·23	9·18
MnO	0·20	0·20	0·18	0·27	0·27	0·19	0·20	0·23	0·23	0·18	0·19	0·20	0·20
MgO	13·76	13·55	11·08	1·74	0·33	8·51	5·39	4·10	3·64	13·25	11·81	11·38	11·36
CaO	11·78	12·12	12·66	6·63	1·44	11·90	11·98	9·91	8·92	10·13	10·75	11·12	11·06
Na_2O	4·30	4·11	3·05	7·58	8·19	3·77	4·84	7·33	6·01	2·91	3·71	3·10	3·52
K_2O	0·97	0·87	1·94	4·10	6·92	2·40	3·06	1·18	4·02	2·50	1·89	2·28	2·11
P_2O_5	1·06	1·11	1·21	0·44	0·06	1·08	1·42	1·10	0·96	0·93	1·13	1·10	1·11
Total	98·88	99·19	99·44	98·68	99·49	99·03	98·89	98·51	98·39	99·28	99·90	99·49	99·59
$Fe_2O_3^{measured}$	6·41	5·10	4·27	3·85	0·98	5·54	3·51	4·73	6·66	3·83	4·37	4·58	4·22
$FeO^{measured}$	7·20	8·56	8·14	3·03	1·03	7·82	7·30	5·36	2·52	9·00	9·27	8·62	8·84
FeO^{tot}	12·97	13·15	11·99	6·49	1·91	12·74	10·46	9·62	8·51	12·41	13·20	12·74	12·64
Volatiles	0·42	0·75	1·05	0·46	5·68	0·61	0·79	1·99	0·71	0·44	0·54	0·61	0·46
Rb ppm	30	9	38	116	193	51	58	70	64	55	45	52	48
Ba	684	630	741	1420	45	497	648	678	767	530	723	771	776
Pb	5	7	6	12	18	5	6	10	8	3	4	5	7
Sr	1142	1135	1245	3281	144	1306	1759	2013	1993	1037	1214	1218	1164
Y	34	33	34	72	22	38	48	57	48	30	37	35	36
Zr	366	367	397	1158	1513	543	656	1040	934	377	469	472	445
Nb	98	99	89	329	150	110	154	215	186	95	110	105	102
Zn	145	114	199	177	147	149	149	111	133	122	134	146	146
Cu	59	63	14	11	53	67	24	24	45	45	51	58	58
Co	61	59	60	8	53	81	54	42	38	117	78	85	59
Ni	341	316	199	4	5	98	16	14	7	321	217	219	217
Sc	25	24	29	0	0	32	17	9	5	26	25	25	25
V	337	340	374	225	27	382	350	263	255	335	336	352	389
Cr	490	516	489	4	4	138	7	13	10	344	191	317	299
Ga	21	24	22	37	40	28	30	32	29	22	23	23	26
La	77	77	81	187	119	87	125	160	152	68	81	83	81
Ce	163	165	165	369	158	182	248	302	302	140	173	179	172
Pr						**21·94**		**34·64**	**34·45**			**18·74**	**19·91**
Nd	81	80	83	147	26	91	117	125	127	70	86	85	87
Sm	*14·00*			*23·00*		**16·55**	*19·80*	**22·35**	**22·17**	*12·60*		**13·99**	**14·98**
Eu	*4·10*			*5·80*		**4·77**	*5·91*	**6·37**	**6·35**	*3·80*		**4·05**	**4·41**
Gd						**15·60**		**21·48**	**21·82**			**13·14**	**14·09**
Tb	1·70			2·40		**1·92**	*2·47*	**2·69**	**2·61**	*1·67*		**1·62**	**1·76**
Dy						**9·44**		**13·29**	**13·10**			**8·15**	**8·59**
Ho						**1·44**		**2·13**	**2·10**			**1·23**	**1·34**
Er						**3·82**		**5·94**	**5·89**			**3·30**	**3·45**
Tm						**0·43**		**0·71**	**0·72**			**0·38**	**0·40**
Yb	*2·10*			*4·30*		**2·55**	*4·43*	**4·31**	**4·35**	*2·54*		**2·29**	**2·38**
Lu	*0·30*			*0·64*		**0·36**	*0·49*	**0·61**	**0·62**	*0·32*		**0·31**	**0·32**
Cs						**0·56**	*0·72*	**1·13**	**1·14**	*0·58*		**0·50**	**0·51**
Hf	*8·00*			*16·00*		**13·05**	*14·00*	**21·01**	**20·77**	*9·04*		***10·83***	***10·72***
Ta	*5·80*			*13·00*		**5·03**	*8·52*	**8·29**	**9·09**	*5·67*		**5·09**	**4·98**
Pb	**3·63**			**10·68**		**4·50**		**10·25**	**8·30**			**4·25**	**4·12**
Th	*7·9*	*8·8*	*9·2*	*26·0*	*29·4*	*10·2*	*11·4*	*21·2*	*22·5*	*6·2*	*8·9*	*9·0*	*8·8*
U	1·0			5·3		2·8		5·3	6·1			2·5	2·5

Trace elements in italics are by INAA, in bold by ICP-MS and the rest by XRF.

Aarhus University. An acceleration voltage of 15 kV and a beam current of 15 nA were used. Except for alkali-rich minerals, the electron beam was focused to 2–4 μm diameter. Energy dispersive analysis was used for most elements; Na, Cr and Ni were analysed by wavelength dispersive methods. ZAF corrections were performed using the Tracor Northern software. Standardization was performed using international natural and industrial mineral standards. Typical uncertainties are 2–5% for the major oxides and <1% of the total. Detection limits are about 0·1% oxide.

Sr–Nd–Pb isotope analysis

Chips of rock were leached for 1 h in hot 6N HCl and dissolved in concentrated HF + HNO_3 (in the ratio 10:1). Pb was extracted in two passes in 6N HCl from ion exchange (AG1 × 8, 100–200#) columns of Pb complexed in 1M HBr. Pb was loaded on Re filaments in silica gel and phosphoric acid and run on a VG 54-30 TIMS instrument in the static mode with filament temperatures of 1180–1270°C. Many of the Pb isotope analyses were duplicated by total rock analyses from dissolution of chips. Only results with within-run statistics better than 1 SEM (standard error of the mean) = 0·2% were accepted. If duplication resulted in large differences, a third or fourth analysis was performed and an eventual outlier discarded. The resulting reproducibility for 23 different samples was: $1\sigma(^{206}Pb/^{204}Pb) = 0{\cdot}006$ (excluding two analyses), $1\sigma(^{207}Pb/^{204}Pb) = 0{\cdot}003$ (excluding three analyses) and $1\sigma(^{208}Pb/^{204}Pb) = 0{\cdot}011$ (excluding five analyses). These uncertainties are actually smaller than the reproducibility of the standard NBS981 used for mass fractionation corrections, which amounted to, on average, $0{\cdot}12 \pm 0{\cdot}01(1\sigma)\%$/AMU (for all three ratios, $N = 20$) relative to the values of Todt *et al.* (1993). Two or three NBS981 standards were run with each sample batch and used for corrections for that batch. We estimate that the reproducibility of NBS981 is our analytical uncertainty. Total chemical procedure blanks were 50–200 pg and insignificant compared with >6 ng dissolved sample Pb.

Sr was extracted using a cut from 2M HCl passing through the anion exchange columns and cleaned using Sr-spec©. REE were collected from the columns after Sr. Nd was then extracted from the REE fraction by ion exchange on Teflon-coated resin using 0·25N HCl. Sr was loaded in 1M phosphoric acid on Ta filaments and Nd loaded in 0·1M HCl on Ta filaments in a triple-filament arrangement with a centre Re filament for high T (1850–1900°C) ionization. Both Sr and Nd were run dynamically with a three-peak jump sequence. Sr results were corrected for mass fractionation using the exponential law and $^{86}Sr/^{88}Sr = 0{\cdot}1194$. Nd was linearly corrected to $^{146}Nd/^{144}Nd = 0{\cdot}7219$. ^{87}Rb interference on Sr was corrected using ^{85}Rb, and ^{144}Sm on Nd using ^{147}Sm. Age corrections of isotope ratios would be insignificant and were not applied.

WHOLE-ROCK GEOCHEMISTRY

Rock classification

According to the total alkalis vs silica diagram (Fig. 4) (Le Maitre, 1989), most samples are nephelinites or basanites–tephrites and need to be classified using CIPW norms according to the revised IUGS nomenclature (Le Bas, 2000). One problem with this approach is that the unknown degree of secondary oxidation of Fe may lead to significant deviation of the actual norm from the pristine norm. We have calculated CIPW norms after correcting Fe to the lower limit of oxidation using the minimum of measured Fe^{3+}/Fe^{total}, which increases systematically from 0·27 in samples with >5% MgO to 0·50 in the phonolites. There is a clear trend towards decreasing silica and increasing alkalis from the OV picrobasalts towards the young mafic volcanic rocks, including basanites, nephelinites and melilite nephelinites. Evolved rocks trend towards phonolite with very few trachytic compositions. The most evolved rocks belong to the intermediate (COVA) and young volcanic phases.

Major elements

Representative major element compositions are given in Table 1. The complete geochemical dataset is available in Electronic Appendix A, which can be downloaded from http://www.oupjournals.org/. MgO contents in 329 analysed samples range from 19 to 0% (analyses reported as wt % on a volatile-free basis unless otherwise indicated) and are used as reference variable in major element variation diagrams (Table 1; Fig. 5). For samples with >5% MgO, there is a broad range of SiO_2 contents between 37 and 45%, whereas for <5% MgO, there is a well-defined trend towards phonolitic compositions with around 57% SiO_2. CaO shows a major inflection around 8% MgO. With decreasing MgO, FeO and TiO_2 decrease from 8% MgO among the rocks most rich in FeO and TiO_2, and from around 6% MgO among rocks with the lowest levels of FeO and TiO_2, which are the OV. The same type of variation is seen for P_2O_5, where the high-P_2O_5 AN group shows a decrease with falling MgO from around 6% MgO, whereas the OV group starts to decrease in P_2O_5 only when MgO falls below 4–5%. There is a remarkably broad range of compositions at high MgO where the temporal rock groups can be identified, although there are considerable overlaps and several samples do not conform to the main group characters. An additional group is geochemically identified among the OV and is called the 'enriched old volcanic rocks' (EOV).

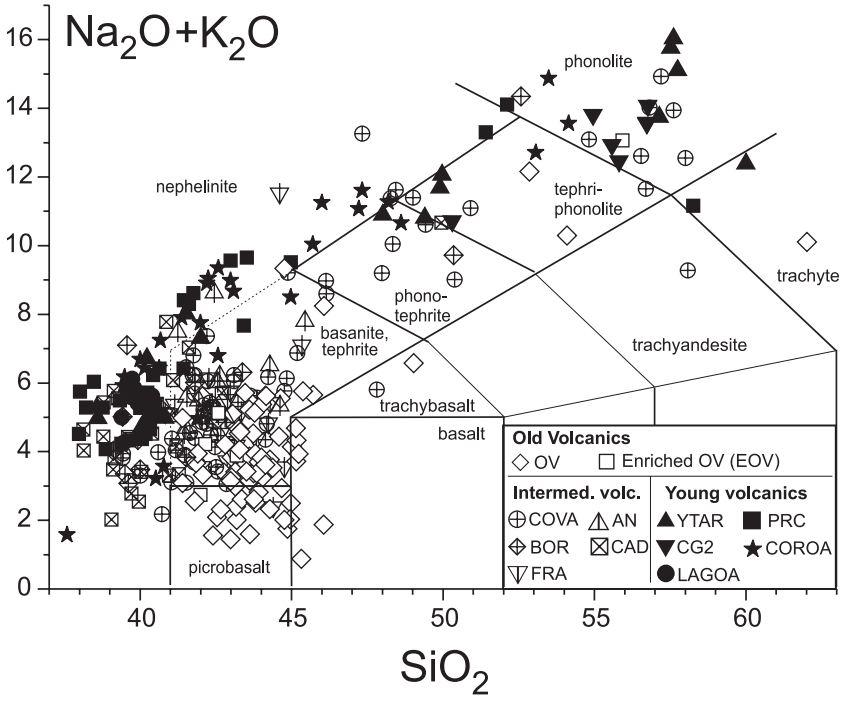

Fig. 4. Total alkalis vs silica classification diagram (Le Maitre, 1989) for Santo Antão volcanic rocks. The groupings and abbreviations are as in Fig. 2.

Alteration of samples

Volcanic rocks are typically highly permeable and subject to reaction with infiltrating hydrothermal fluids or meteoric water. Because volcanic glass is hygroscopic, and there is a large variation in the proportion of glass in the samples, high volatile contents (LOI) may indicate hydration of the glass but not, necessarily, significant post-magmatic mobilization of major or trace elements. Hydrated samples with >2·5% volatiles do not systematically show abnormal contents of fluid-mobile elements (Na, K, Rb, Ba) compared with the trends in variation diagrams (Figs 4–6), in plots vs an immobile element such as Al_2O_3 (not shown), and do not show other signs of alteration, such as elevated Fe^{3+}/Fe^{2+} ratios. Samples (~5% of the dataset) with very high volatile contents, or with Fe^{3+}/Fe^{2+}, K/Rb or Na_2O/Al_2O_3 ratios deviating from the main range have not been used in the discussion below.

Trace elements

The volcanic products from Santo Antão show relatively high abundances of mantle incompatible elements that increase with decreasing MgO (Table 1; Fig. 6). Only Zr, Hf, Rb, Cs and Th increase to the phonolite stage; REE, Y, Nb, Ta, Sr, Ba, Pb and U decrease at low MgO values. Inflections in the trends occur at varying MgO contents for different elements reflecting the onset of crystallization of various minerals. Sr decreases with falling MgO from 2% MgO, whereas the Nb, Ba and Ga trends inflect at ~1% MgO. Levels of incompatible trace elements in the high-MgO rocks show considerable variations between the groups identified, e.g. La 30–130, Zr 150–600, Nb 50–150, Rb 10–70, Ba 250–1000 and Sr 500–2000 ppm (Table 2; Fig. 6).

The variations of selected compatible trace elements as a function of % MgO are presented in Fig. 7. Ni and Cr contents decrease to a few ppm at 5% MgO. The CAD, LAGOA and COROA groups have 100–400 ppm Cr at 12% MgO, whereas OV, COVA and FRA have 500–800 ppm Cr. There is the same qualitative difference for Ni. OV and FRA have higher Sc at high MgO than other groups. Sc decreases for all groups for MgO <9–10%. V decreases below ~7% MgO.

Primitive mantle-normalized incompatible element patterns for the most primitive Santo Antão volcanic rocks show an overall picture for averages of old, intermediate and young rocks with MgO = 10–14 wt % (Fig. 8) of strongly fractionated moderately incompatible elements including the HREE, a maximum at Nb and Ta and variable negative K anomalies and an increase in abundance of incompatible elements with time. The enrichment of Nb varies from 60–210 × PM (Primordial Mantle; Sun & McDonough, 1989) for all samples, and, on average, the enrichment in the OV samples is about half of that in the samples of the young groups for all very incompatible elements. The negative anomaly for K (K/K*; K* is interpolated from adjacent elements in

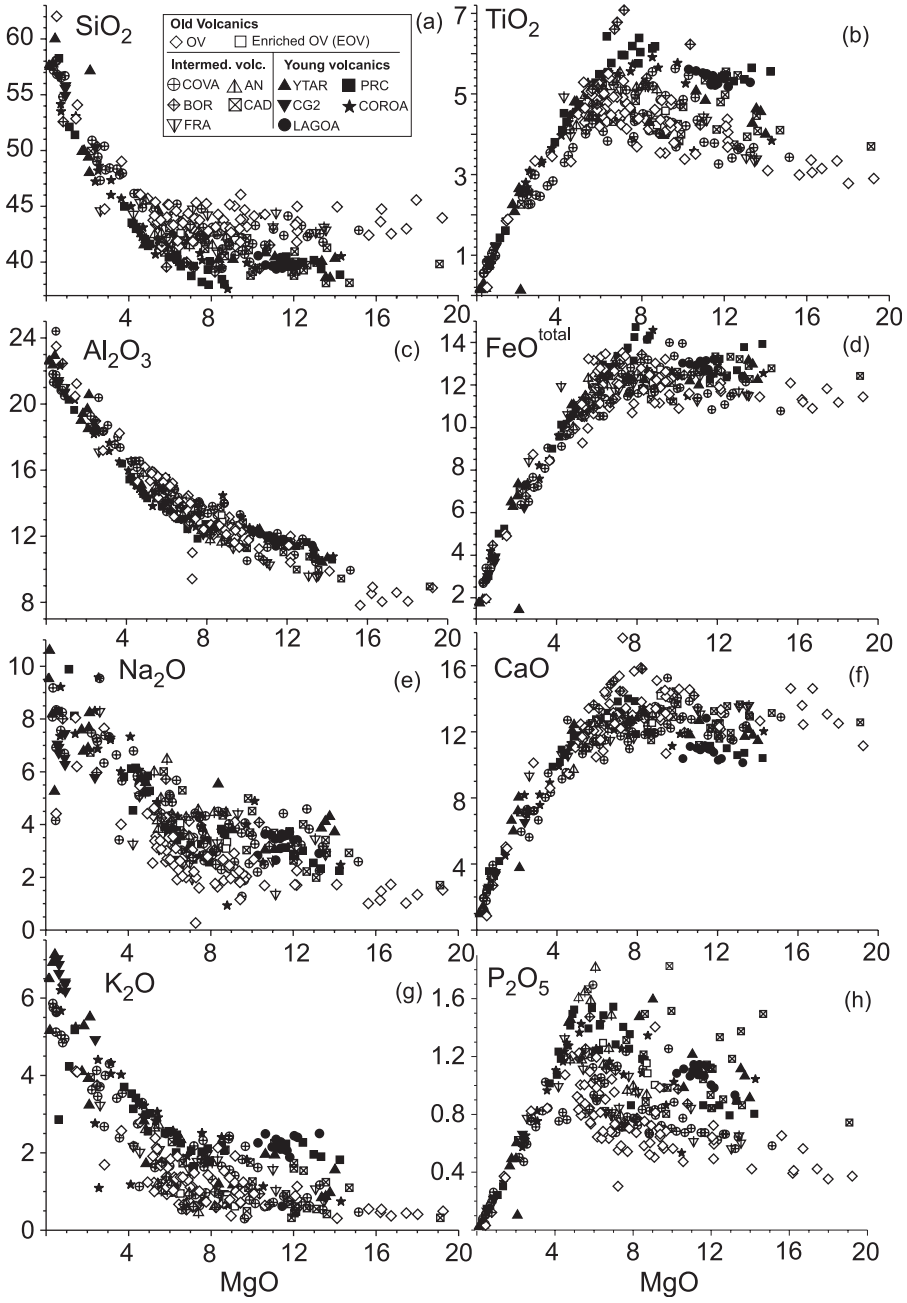

Fig. 5. Major element variation (wt % oxides) vs MgO (a–h) for Santo Antão volcanic rocks. The groupings and abbreviations (Fig. 2) are discussed in the text.

Fig. 8) is, on average, 0·5 for the young volcanic rocks and 0·3 for the intermediate and OV. The abundances of HREEs are low, e.g. $Lu_{PM} \sim 4$.

Distinction of the temporal groups

Of the most primitive samples (MgO >8%), the OV rocks have the highest SiO_2 contents (43–45·5%; Fig. 5a) and lowest incompatible element contents (e.g. Figs 5 and 6: lowest TiO_2, P_2O_5, La and Nb) and constitute a well-defined group. They are further characterized by their relatively low La/Nb (0·6–0·7), Sr/Nb (9–12), Rb/Nb (0·2–0·4), Ba/Nb (5–8) and high Ce/Pb (35–40) ratios relative to other Santo Antão high-MgO rocks (Table 1).

The intermediate age rocks ($SiO_2 \approx$ 40–43%) of the COVA group are more alkaline and incompatible element-enriched (Fig. 8) than the OV and have higher Sr/Nd (≈16–20), Sr/Nb (≈12–15), La/Nb (≈0·7–0·8)

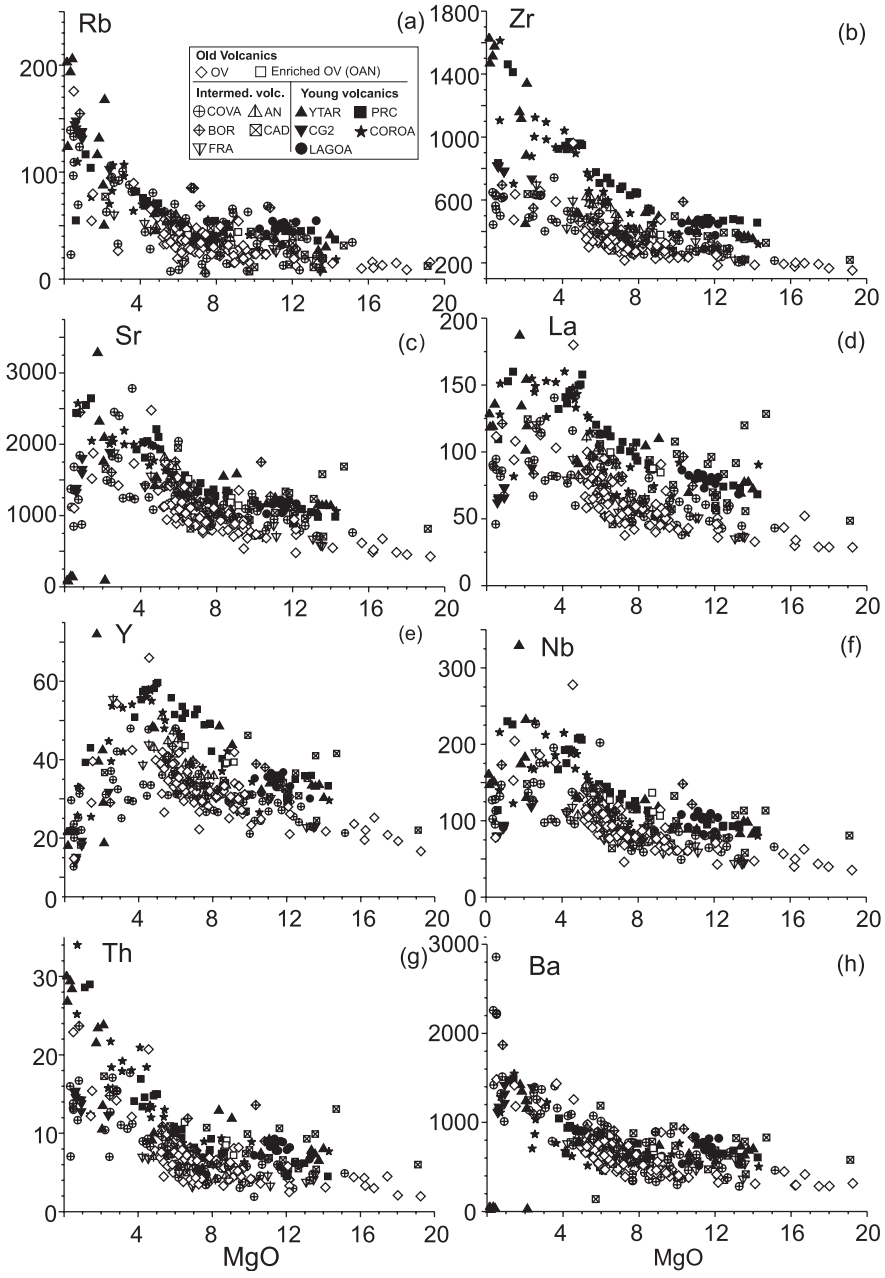

Fig. 6. Incompatible element variation (ppm) vs wt % MgO: (a) Rb; (b) Zr; (c) Sr; (d) La; (e) Y; (f) Nb; (g) Th; (h) Ba, in ppm; symbols as in Fig. 2.

and Rb/Nb (≈0·3–0·8) ratios (Table 1). The BOR volcanic group includes the first nephelinites to be erupted on Santo Antão and these show even greater enrichment in very incompatible elements than the COVA samples (Figs 5 and 6). Geochemically, the FRA group is intermediate between the COVA group and the more enriched AN group.

The CAD group nephelinites and melilite nephelinites display a large range of compositions with SiO_2 contents as low as 38%. Their LREE enrichment reaches the extreme for Santo Antão (Fig. 6d and e), and they have high La/Nb ratios (0·8–1·1). Furthermore, Ba/Nb in CAD is not higher than in OV and COVA. LAGOA has Sr/Nd = 13–15, whereas COROA and PRC have 10–14. All the latter three have low Sr/Nb (10–12) and relatively high La/Nb (0·7–0·9; one sample has 1·1).

Mineral chemistry

Phenocryst phases were analysed in representative rocks, and selected mineral analyses are presented in Table 2.

Table 2: Selected phenocryst compositions by electron microprobe analysis

Mineral:	Clinopyroxene					Olivine			Kaersutite		Chromite		Titanomagnetite		
Group:	OV	OV	OV	YTAR	COVA	CAD	LAGOA	OV	COVA	COVA	OV	OV	COVA	OV	COVA
Sample no.:	111743	111811	111757	111808	109568	111827	111935	111757	109563	109568	109905	111757	109568	111822	109568
Rock type:	picr	tephr	basa	teph-ph	phon	mela-ne	tephr	basa	tephr	phon	basa	basa	phon	basa	phon
MgO_{rock}	12·2	6·2	12·2		0·5	11·4	5·5	12·2	5·3	0·5	11·2	12·2	0·5	9·6	0·5
SiO_2	49·40	40·05	45·31	47·86	45·06	40·82	40·88	39·06	38·00	38·36	0·24	0·20	0·28	0·20	0·11
TiO_2	1·55	7·09	3·26	2·39	1·69	0·01	—		6·06	3·95	3·87	17·30	24·25	13·41	2·96
Al_2O_3	3·57	10·60	6·95	3·87	7·13	0·01	—		13·91	13·11	15·74	9·30	6·3	7·77	2·81
FeO_{tot}	4·99	8·34	5·93	7·86	14·38	9·02	9·84	16·34	9·89	18·55	29·04	55·19	61·62	65·50	81·77
MnO	0·01	0·26	0·01	0·36	0·65	0·19	0·18	0·34	0·14	0·66	0·32	0·85	0·91	0·61	5·84
MgO	15·20	10·28	13·28	12·48	7·30	49·49	48·81	43·11	13·51	7·83	12·05	4·61	3·09	6·22	1·29
CaO	22·58	22·60	22·05	23·20	21·90	0·14	0·28	0·39	12·23	11·29	0·11	0·01	0	0·01	0·01
Na_2O	0·26	0·67	0·55	0·62	1·55	0·01	—		2·46	2·53	0·00	0·01	0·06	0·01	0·01
K_2O	0·01	0·01	0·08	0·01	0·01	0·01	—		1·59	1·71	0·01	0·01	0	0·01	0·01
NiO	0·05	0·01	—	0·01	—	0·33	0·28	0·18			0·19	0·05	—	0·10	—
Cr_2O_3	0·31	0·04	—	0·09	0·07	0·01	—	0·07			37·62	10·84	0·85	2·12	0·02
Sum	97·89	99·91	97·40	98·72	99·74	99·97	100·27	99·47	97·79	98·00	99·19	98·31	97·42	95·93	94·85
FeO_{cor}	3·14	3·57	2·37	4·13	6·56						19·35	41·09	48·77	34·61	26·76
Fe_2O_{3cor}	2·06	5·30	3·96	4·16	8·69						10·76	15·67	14·31	34·33	61·23
New sum	98·10	100·45	97·8	99·14	100·61						100·27	99·88	98·88	99·37	101·07
Cations	Assuming 6 oxygens and 4 cations					Based on 4 oxygens			23 oxygens		4 oxygens and 3 cations:				
Si	1·85	1·51	1·72	1·81	1·72	1·00	1·00	0·99	5·65	5·90	0·01	0·01	0·01	0·01	0·00
Al(IV)	0·15	0·47	0·28	0·17	0·28	0·00	—	0·00	2·44	2·38	0·59	0·38	0·27	0·32	0·12
Al(VI)	0·01	0·00	0·03	0·00	0·04										
Ti	0·04	0·20	0·09	0·07	0·05	0·00	—	0·00	0·68	0·46	0·09	0·45	0·65	0·35	0·08
Mg	0·85	0·58	0·75	0·70	0·42	1·81	1·78	1·64	2·99	1·80	0·57	0·24	0·17	0·32	0·07
Fe^{2+}	0·10	0·11	0·08	0·13	0·21	0·18	0·20	0·35	1·23	2·39	0·52	1·19	1·46	1·01	0·83
Fe^{3+}	0·06	0·15	0·11	0·12	0·25	—	—	—	—	—	0·26	0·41	0·39	0·90	1·70
Mn	0·00	0·01	0·00	0·01	0·02	0·00		0·01	0·02	0·09	0·01	0·02	0·03	0·02	0·18
Ca	0·91	0·91	0·90	0·94	0·90	0·00	0·01	0·01	1·95	1·86	0·00	0·00	0	0·00	0·00
Na	0·02	0·05	0·04	0·05	0·11	0·00	—	0·00	0·71	0·75	0·00	0·00	0	0·00	0·00
K	0·00	0·00	0·00	0·00	0·00	0·00	—	0·00	0·30	0·34	0·00	0·00	0	0·00	0·00
Ni	0·00	0·00	—	0·00	—	0·01	0·01	0·00			0·00	0·00	—	0·00	—
Cr	0·01	0·00	—	0·00	0·00						0·94	0·30	0·02	0·06	0·00
Sum	4·00	4·00	4·00	4·00	4·00	3·00	3·00	3·00	15·97	15·97	3.00	3.00	3.00	3.00	3.00
$Mg\text{-no.}/Fe_{tot}$	84	69	80	74	48	91	90	83			52	17	10	24	8
$Mg\text{-no.}/Fe^{2+}$	89	84	91	84	67					Cr-no.	83	44		15	0
										Usp			0·63	0·28	0·04

Table 2: continued

Mineral:	Haüyne			Plagioclase			Sanidine		Nepheline		Titanite		
Group:	PRC	COVA		OV	OV	COVA	CG2	CG1	OV		OV	CG3	CG1
Sample no.:	110024	109568		111743	109971	109568	111680	111999	109803		109803	109688	109999
Rock type:	mela-ne	phon		picr	tephr	phon	phon	phon	teph-ph		teph-ph	phon	phon
MgO_{rock}	4·1	0·5		12·2	6·1	0·5	0·6	0·07	1·2		1·2	0·14	0·07
SiO_2	33·05	36·11		45·91	50·51	61·41	60·18	64·16	43·45		29·91	29·71	28·4
Al_2O_3	28·39	29·60		32·84	30·16	23·65	20·37	18·65	34·58		1·43	1·25	1·41
Fe_2O_{3tot}	0·49	0·53		0·78	0·63	0·45	0·25	0·28	0·6		1·52	1·23	2·17
CaO	8·99	6·11		16·43	12·76	4·68	0·98	0·13	1·62		27·71	27·71	28·61
BaO	—	—		—	0·1	—	2·66	0·21					
Na_2O	13·39	6·47		2·08	4·19	7·43	3·76	5·19	16·55		0·05	0·07	0·03
K_2O	0·89	0·39		0·18	0·24	1·87	8·22	8·03	4·98		—	0·02	0·03
Cl	0·30	0·81				0·01							
SO_4	15·14	14·21				0·01							0·1
TiO_2+MgO+MnO		0·03	0·03	0·19		0·37			0·02	TiO_2	36·27	27·02	24·13
MgO				0·13		0·01					0·07	0·04	—
MnO				0·01		0·01					0·07	0·09	0·09
Sum	100·72	94·27		98·43	98·59	99·92	96·42	96·65	101·81		97·02	87·53	85·47
Cations	24 oxygens in tetrahedrons				Based on 8 oxygens				32 ox		based on Si = 4		
Si	5·96	6·10		2·14	2·32	2·75	2·89	3	8·2		4	4	4
Al	6·04	5·90		1·8	1·64	1·25	1·15	1·03	7·69		0·26	0·20	0·24
Fe^{3+}	0·07	0·07		0·03	0·02	0·02	0·01	0·01	0·07		0·16	0·12	0·23
Ca	1·74	1·11		0·82	0·63	0·22	0·05	0·01	0·33		3·99	4·00	4·32
Ba					0·00	0·00	0·05	0					
Na	4·68	2·12		0·19	0·37	0·65	0·35	0·47	6·06		0·01	0·02	0·01
K	0·20	0·08		0·01	0·01	0·11	0·5	0·48	1·2		—	0·00	0·00
Ti				0·01	—	—	—	—	—		3·65	2·74	2·56
Sum	18·69	15·38		4·99	5·00	5·00	5·00	5·00	23·55		12·06	11·08	11·35
Cl^-	0·06	0·16	Or+Cel	1		11	58	50	0·83	Na/Na+K			
SO_4^{2-}	1·71	1·50	Ab	18		66	37	49					
			An	81		23	5	1					

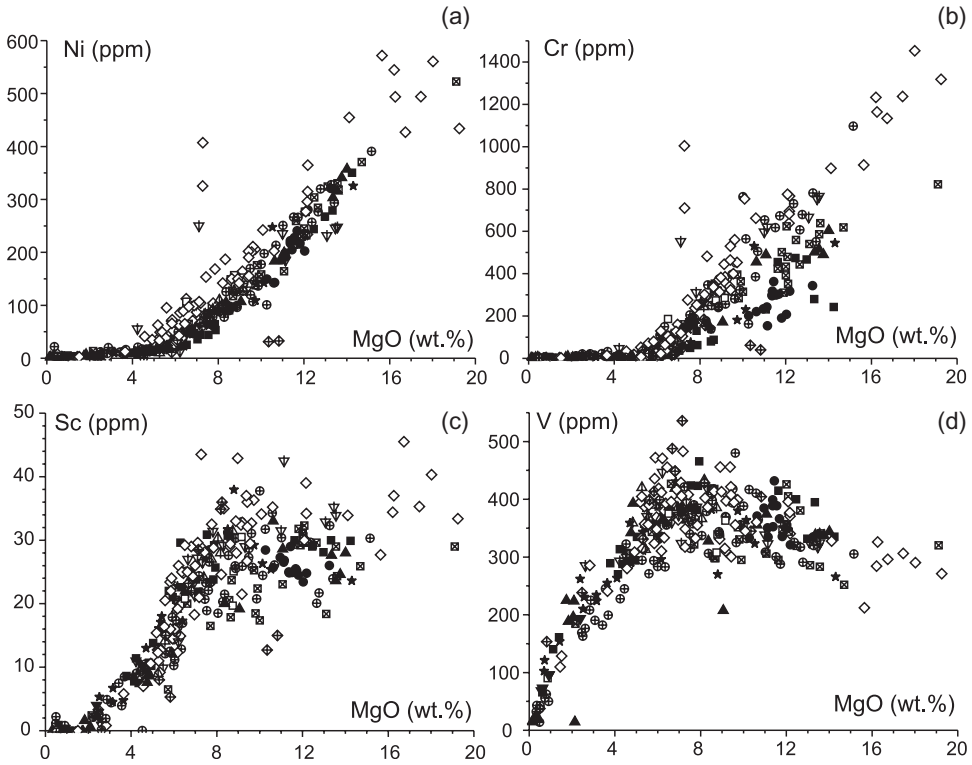

Fig. 7. Compatible trace element variation vs wt % MgO: (a) Ni; (b) Cr; (c) Sc; (d) V, in ppm. Symbols as in Fig. 2.

Clinopyroxenes show a continuous range and variation from diopside-rich with 1·2% Cr_2O_3 (3 vol. % Cr-diopside component) and Mg-number (based on $Fe^{2+} + Fe^{3+}$) = 89 to ferro-salite (Mg-number = 42) with 10 vol. % acmite and 10 vol. % other ferri-components ($Fe^{3+}_{vi}Fe^{3+}_{iv}$ and $Fe^{3+}_{vi}Al_{iv}$). Clinopyroxenes in the intermediate composition lavas are Ti-salites with up to 10 vol. % of the $CaTiAl_2O_6$ molecule and rich in Fe^{3+} (calculated $Fe^{3+}/Fe^{total}_{mean} \approx 0{\cdot}5$). TiO_2 reaches a maximum of 7·1%. Low-pressure crystallization is indicated by very low Al^{3+}_{vi} values (<0·1 and commonly 0). Abrupt zonation with core–mantle differences in a small fraction of the phenocrysts may represent a break in composition of up to half the entire range for Santo Antão clinopyroxenes.

Olivine phenocrysts are in the range $Fo_{91–74}$ with most >Fo_{80}. Almost all of the most forsteritic olivines (>Fo_{88}) have 0·2–0·4% CaO. Ni in olivine phenocrysts correlates with Mg-number and reaches >3000 ppm. There is only a general and very broad correlation between the MgO in host rocks and mol. % Fo in olivine. Olivines display a compositional variation in individual samples of ΔFo = 5–15. In 111832, olivine is in the range $Fo_{90–81}$.

Amphiboles are mostly kaersutites but pargasite–ferropargasite (lower Ti) occurs in the phonolites and tephriphonolites. They cover a wide compositional range (Mg-number 75–42). TiO_2 contents (6·6–3·7%) decrease with decreasing Mg-number. K_2O/Na_2O ratios are mostly in the range 0·5–0·7.

The most common oxide in the intermediate rocks is titanomagnetite, although chromite is present in many of the more primitive samples. Both magnetite and chromite, however, occur in rocks of various stages of evolution, suggesting magma mixing. The titanomagnetite variation follows the Fe–Ti trend of Barnes & Roeder (2001). There is a clear trend of decreasing ulvöspinel component from up to Usp_{80}–Mag_{20} in rocks with ~12% MgO to Usp_5–Mag_{95} in rocks with ~1% MgO. Most analyses have a (titano-)maghemite component of ~10 vol. %, probably resulting from oxidation during cooling. Chromite has up to 42 % Cr_2O_3, which correlates with Mg-number in the interval 20–65. MnO in magnetite increases to >6% in some phonolites.

Haüynes are relatively rich in Ca and S for this sodalite group mineral. The Na/(Na + K + Ca) ratio in Santo Antão haüyne increases with host rock evolution from nephelinite to phonolite; this is accompanied by an increase in the Cl/SO_4 ratio (Table 2).

Some basanite series rocks have plagioclase in the compositional range $An_{87–26}$. Plagioclase in phonolites is $An_{39–23}$ and sodic varieties grade into anorthoclase. Zoning is both normal and reverse, but mostly optically undetectable with ΔAn < 4%, but ranging to 11%. Sanidine is typically $Or_{50–60}$ but wide ranges ($Or_{40–82}$) occur in

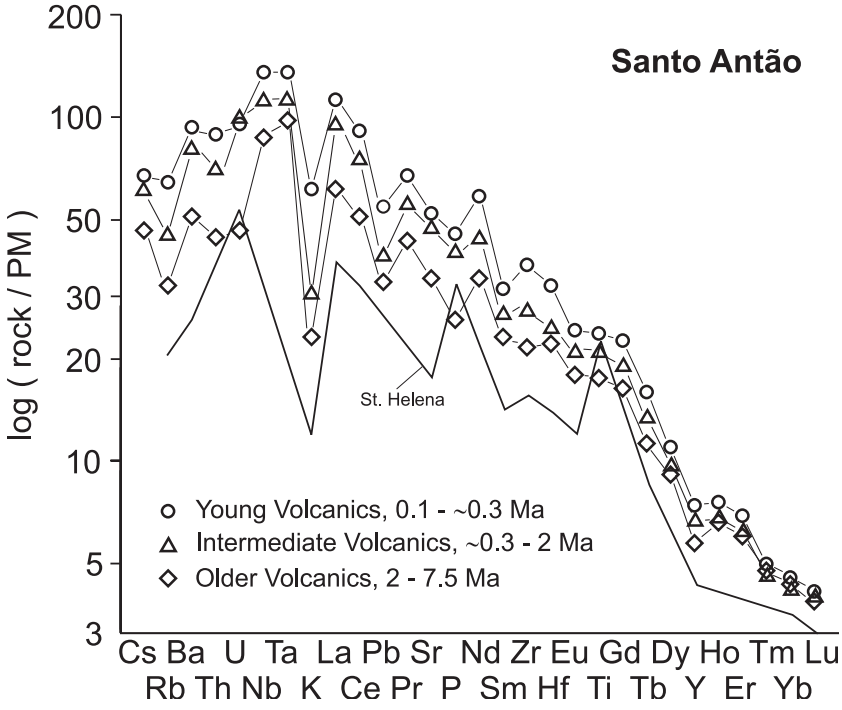

Fig. 8. Primitive mantle normalized incompatible element patterns of averages of primitive rocks from Santo Antão with MgO = 10–14 wt % divided into the temporal groups: Young ($N = 26$), Intermediate ($N = 42$) and Old Volcanic rocks ($N = 7$). The main difference between the groups is an increase in incompatible element abundance. The Santo Antão samples are more enriched in the most incompatible elements than the plotted sample 215 from the HIMU island St Helena (Chaffey *et al.*, 1989). Primitive mantle normalizing values from Sun & McDonough (1989).

the evolved nephelinites, tephriphonolites and phonolites of the nephelinite series. Rare nepheline is around $Ne_{84}Ks_{16}$.

Sr–Nd–Pb isotopic compositions

The Sr, Nd and Pb isotope compositions of selected samples from the Santo Antão volcanic sequence are presented in Table 3 and cover the ranges: $^{87}Sr/^{86}Sr$ 0·70299–0·70333; $^{143}Nd/^{144}Nd$ 0·51297–0·51282; $^{206}Pb/^{204}Pb$ 19·17–19·89; $^{207}Pb/^{204}Pb$ 15·58–15·65 and $^{208}Pb/^{204}Pb$ 38·79–39·66 (Fig. 9). The new data for Santo Antão considerably extend the range of Pb isotopic compositions for the Cape Verdes reported by Gerlach *et al.* (1988), whereas two of their samples—NA15 and NA80—have slightly lower $^{87}Sr/^{86}Sr$ and higher $^{143}Nd/^{144}Nd$ (Fig. 9a). Because the data of Gerlach *et al.* (1988) lack stratigraphical constraints, they will not be considered further in this work. There is a negative correlation between $^{87}Sr/^{86}Sr$ and $^{143}Nd/^{144}Nd$ and a positive correlation between $^{208}Pb/^{204}Pb$ and $^{206}Pb/^{204}Pb$ (Fig. 9c and d). However, neither $^{207}Pb/^{204}Pb$, $^{143}Nd/^{144}Nd$ nor $^{87}Sr/^{86}Sr$ correlates with $^{206}Pb/^{204}Pb$ (Fig. 9b, c and e). Overall, the Santo Antão volcanic rocks have Sr and Nd isotopic compositions between those of Central Atlantic N-MORB and the southern Cape Verde Islands (Fogo and Santiago in Fig. 9), whereas Pb isotopes are more radiogenic than either.

The isotopic compositions of the Santo Antão magmas have changed over time and the various temporal groups can, to some extent, be identified by their isotopic compositions, although there is considerable overlap. The OV extend to the highest $^{87}Sr/^{86}Sr$, $^{206}Pb/^{204}Pb$ and $^{208}Pb/^{204}Pb$ and most unradiogenic Nd, whereas the intermediate AN and COVA groups have the most MORB-like Sr and Nd. The most unradiogenic Pb is found in the intermediate CAD group. The COROA, PRC and LAGOA groups of the young volcanic rocks have intermediate Sr and Nd isotopic compositions, but trend towards higher $^{207}Pb/^{204}Pb$ than the older rocks (Fig. 9c and f). Intermediate BOR and FRA group rocks have the most uranogenic Pb with the lowest time-integrated Th/U (Fig. 9d; Table 3).

All measured μ ($^{238}U/^{204}Pb$ ratios) are high, mostly 26–43, with a total range of 18–71 and median of 35, but show no correlation with Pb isotope ratios or sample groups. This range of μ is high relative to MORB (average $\mu = 11 \pm 5$; White, 1993) and comparable with many OIB ($\mu = 20$–43; Thirlwall, 1997). The decoupling of μ and the isotopic composition of Pb are common features in both MORB and OIB (White, 1993; Thirlwall, 1997).

Table 3: Isotopic composition of Sr, Nd, Pb and He in Santo Antão volcanic rocks

Sample	$^{87}Sr/^{86}Sr$		$^{143}Nd/^{144}Nd$	$^{206}Pb/^{204}Pb$		$^{207}Pb/^{204}Pb$			$^{208}Pb/^{204}Pb$			Δ7/4	Δ8/4	R/Ra[1]
Old Volcanic rocks														
OV														
106454	0·703275		0·512895	19·811		15·622			39·560			−1·7	1·8	
111753	0·703267		0·512856	19·652		15·595			39·366			−2·6	−2·0	
109965	0·703318		0·512818	19·590		15·585			39·307			−3·0	−0·4	
109564				19·544		15·583			39·225			−2·7	−3·1	
111750	0·703262		0·512898	19·688		15·594			39·438			−3·1	0·8	
111743	0·703332		0·512882	19·884	19·890	19·878	15·599	15·602	15·596	39·648	39·658	39·637	−4·7	−1·9	
111757	0·703207		0·512890	19·692	19·622	19·761	15·598	15·600	15·595	39·402	39·346	39·457	−2·8	−3·3	
111822	0·703276		0·512861	19·566	15·600					39·272			−1·2	−1·0	3·2
111762				19·789			15·599			39·505			−3·7	−4·7	
111756	0·703168		0·512901	19·566	19·502	19·630	15·583	15·585	15·580	39·275	39·281	39·269	−2·9	−0·7	
111748	0·703259		0·512869	19·842	19·830	19·853	15·606	15·604	15·608	39·595	39·579	39·610	−3·6	−2·1	
111751	0·703277		0·512862	19·818	19·814	19·821	15·601	15·601	15·601	39·555	39·554	39·555	−3·8	−3·2	
114531	0·703256	0·703230	0·512867	19·451			15·616			39·142			1·7	−0·1	
111745				19·834	19·832	19·836	15·597	15·599	15·594	39·569	39·577	39·560	−4·5	−3·8	
109521	0·703178				19·568		15·575			39·220			−3·7	−6·5	
109957	0·703200													
109527	0·703213		0·512923	19·561			15·597			39·233			−1·4	−4·3	
109962	0·703045		0·512894	19·675			15·592			39·381			−3·2	−3·3	
106453	0·703174		0·512920	19·658			15·573			39·236			−4·9	−15·7	
109952	0·703184		0·512884	19·776			15·586			39·416			−4·9	−12·0	
EOV														
114528	0·703229			19·702			15·638			39·540			1·1	9·3	
114533	0·703253		0·512870	19·673			15·598			39·408			−2·6	−0·4	
Intermediate Volcanic rocks														
BOR														
109901	0·703037		0·512944	19·927			15·605			39·338			−4·6	−38·1	
109994	0·703127		0·512900	19·694			15·597			39·314			−2·9	−12·3	
109995	0·703138		0·512879	19·539			15·580			39·147			−2·9	−10·3	
109997	0·703074			19·871			15·607			39·288			−3·8	−36·3	

[1]R/Ra is $^{3}He/^{4}He$ sample normalised to the air value $1.39*10^{-6}$ and the results are from Christensen et al. (2000).

Table 3: continued

Sample	$^{87}Sr/^{86}Sr$	$^{143}Nd/^{144}Nd$		$^{206}Pb/^{204}Pb$			$^{207}Pb/^{204}Pb$				$^{208}Pb/^{204}Pb$				Δ7/4	Δ8/4	R/Ra[1]
COVA																	
110062	0·702959	0·512946	19·610	19·626	19·590[4]	19·615	15·611	15·612	15·610[4]	15·611	39·152	19·166	19·130[4]	19·161	−0·5	−18·0	11·7
114816	0·703046		19·360				15·636				38·979				4·6	−5·4	
109558	0·703024																
109502	0·703105	0·512908	19·544				15·575				39·145				−3·5	−11·1	
109557	0·703080	0·512949	19·505				15·579				39·051				−2·6	−15·8	
110033	0·703123	0·512912	19·678				15·636				39·288				1·2	−13·0	
111768	0·703252	0·512932	19·536	19·538	19·533		15·593	15·591	15·594		39·087	39·086	39·087		−1·6	−15·9	
111840	0·703036	0·512934	19·748	19·736	19·759		15·613	15·610	15·616		39·301	39·432	39·170		−1·9	−20·1	
109556	0·703147	0·512918	19·625					15·599			39·136				−1·9	−21·8	
109508	0·703115	0·512936	19·604					15·590			39·199				−2·6	−12·9	
109563	0·702988	0·512934	19·530					15·595			39·089				−1·3	−15·0	
109545	0·702985	0·512909	19·536					15·586			39·082				−2·3	−16·4	
109546	0·703073	0·512917	19·689					15·591			39·244				−3·4	−18·7	
114811	0·703023		19·686	19·701	19·671			15·594	15·602	15·586	39·206	39·204	39·207		−3·1	−22·2	
111767	0·702972	0·512968	19·386	19·388	19·384			15·582	15·593	15·571	39·206	39·029	38·958		−1·0	−7·1	
109551	0·703055	0·512943	19·757					15·589			39·210				−4·4	−30·3	
106459	0·703008	0·512683	19·489					15·584			39·051				−1·9	−13·9	
109568	0·703024																
FRA																	
111813	0·703237	0·512913	19·892					15·628			39·297				−1·9	−37·9	
111718	0·703162	0·512911	19·731	19·736	19·726			15·631	15·632	15·629	39·312	39·320	39·303		0·1	−17·0	
106452	0·703085	0·512952															
AN																	
111712	0·703002	0·512985	19·705	19·702	19·707			15·606	15·601	15·611	39·184	39·168	39·200		−2·1	−26·6	
111709	0·703020	0·512947	19·715	19·714	19·705		15·611	15·620	15·609	15·604	39·184	39·212	39·181	39·160	−1·7	−27·4	
111708			19·623				15·610					39·166			−0·8	−18·5	
111725	0·703005	0·512933	19·498	19·501	19·494		15·591	15·598	15·584		39·060	39·036	39·060	39·011	−0·7	−14·4	
111705	0·703040	0·512967	19·687	19·690	19·685	19·691	15·605	15·612	15·599	15·605	39·191	39·220	39·172	39·191	−2·0	−23·8	
111713	0·703003	0·512949	19·570	19·572	19·568		15·593	15·592	15·593		39·066	39·067	39·065		−2·1	−22·3	

Sample	$^{87}Sr/^{86}Sr$		$^{143}Nd/^{144}Nd$		$^{206}Pb/^{204}Pb$		$^{207}Pb/^{204}Pb$					$^{208}Pb/^{204}Pb$			Δ7/4	Δ8/4	R/Ra[1]
CAD																	
111832	0·703164	0·703174	0·512905	19·173			15·548			38·820					−2·2	1·3	9·2
114522				19·759			15·619			39·413					−1·4	−10·3	
114521	0·703119		0·512903	19·774			15·624			39·447					−1·1	−8·7	
111828	0·703116		0·512901	19·746			15·605			39·350					−2·6	−15·0	
110049	0·703121		0·512927	19·688			15·613			39·225					−1·2	−20·5	
110041	0·703093		0·512919	19·165			15·600			38·789					3·2	−0·8	
Younger Volcanic rocks																	
PRC																	
111721	0·703020		0·512916	19·610			15·631					39·232				1·4	−10·3
111737	0·703093	0·703026	0·512892	19·607	19·604	19·610	15·618		15·620		15·615	39·191	39·198	39·183	0·2	−14·1	
111717	0·703104		0·512948	19·625	19·634	19·616	15·623	15·620	15·626			39·195	39·214	39·175		0·5	−15·9
111701	0·703100		0·512918	19·663	19·679	19·646	15·636	15·647	15·624			39·277	39·321	39·232	1·5	−10·3	
110021	0·703044		0·512912	19·322			15·596					38·895			1·0	−9·2	
YTAR																	
111837				19·691			15·620					39·293			−0·6	−14·0	13·8
111764	0·703127		0·512921	19·773			15·603					39·356			−3·1	−17·7	
111763	0·703108		0·512916	19·763			15·611					39·379			−2·2	−14·1	
106456				19·413			15·593					38·988			−0·2	−11·0	
111759	0·703059		0·512911	19·690	19·687	19·692	15·598	15·602	15·594			39·254	39·267	39·240	−2·7	−17·8	
106455	0·703226		0·512929	19·439			15·605					39·012			0·7	−11·7	
COROA																	
110029	0·703088		0·512903	19·590			15·617					39·186			0·2	−12·5	
110028	0·703046		0·512899	19·583			15·619					39·188			0·5	−11·5	
110026	0·703111		0·512915	19·632			15·644					39·291			2·5	−7·1	
110030	0·703081		0·512915	19·615			15·632					39·229			1·5	−11·3	
LAGOA																	
110052	0·703068		0·512881	19·653	19·641	19·665	15·621	15·611	15·630			39·248	39·235	39·248	−0·1	−13·9	
106457	0·703095		0·512904	19·634			15·616					39·220			−0·3	−14·4	
111940				19·630			15·620					39·220			0·1	−14·0	9·1
111827	0·703050			19·449			15·621					39·028			2·2	−11·3	7·0

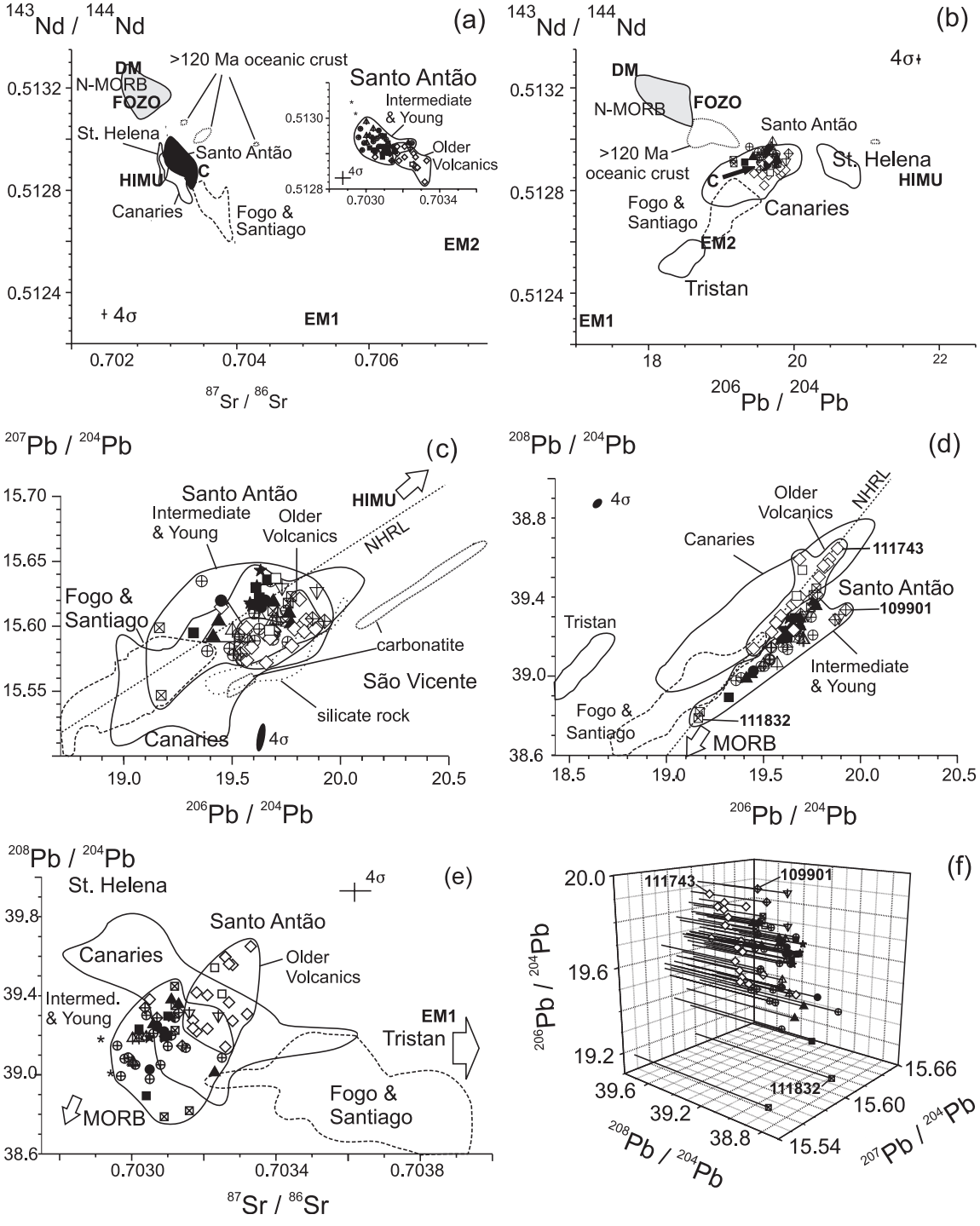

Fig. 9. Isotopic composition of Sr, Nd and Pb from Santo Antão, Fogo, Santiago, the Canary Islands, St Helena, the Canaries and Tristan da Cunha. (a) $^{143}Nd/^{144}Nd$ vs $^{87}Sr/^{86}Sr$; (b) $^{143}Nd/^{144}Nd$ vs $^{206}Pb/^{204}Pb$; (c) $^{207}Pb/^{204}Pb$ vs $^{206}Pb/^{204}Pb$; (d) $^{208}Pb/^{204}Pb$ vs $^{206}Pb/^{204}Pb$; (e) $^{208}Pb/^{204}Pb$ vs $^{87}Sr/^{86}Sr$; (f) $^{208}Pb/^{204}Pb$ vs $^{207}Pb/^{204}Pb$ vs $^{206}Pb/^{204}Pb$. Also shown in (a) and (b) is the composition of Central Atlantic N-MORB, Central Atlantic oceanic crust older than 120 Ma, the mantle end-members DM, FOZO, C, EM1, EM2 and HIMU. Data sources: Santo Antão (Table 1; NA15, NA80: Gerlach *et al.*, 1988); South Cape Verde Islands: Fogo (Kokfelt *et al.*, in preparation), Santiago (our unpublished data), São Vicente (Jørgensen & Holm, 2002, and in preparation), Central Atlantic (10–24°N) N-MORB (Dosso *et al.*, 1993), St Helena (Chaffey *et al.*, 1989), Tristan da Cunha (Le Roex *et al.*, 1990), Canaries (Hoernle *et al.*, 1991; Simonsen *et al.*, 2000). NHRL, the Northern Hemisphere Reference Line (Hart, 1984), Oceanic crust >120 Ma (Janney & Castillo, 2001), mantle end-members (Hoffman, 1997). Three Santo Antão samples with extreme compositions are marked. See discussion for details. Symbols as in Fig. 2. *NA15 and NA80 from Gerlach *et al.* (1988).

Compared with other Atlantic hotspots, the Cape Verde Islands trend towards Tristan da Cunha [an EM1-type OIB (Zindler & Hart, 1986)] in Sr–Nd–Pb isotopic space at higher $^{143}Nd/^{144}Nd$ than the Canaries and St Helena hotspots (Fig. 9a), and lower $^{143}Nd/^{144}Nd$ than the Iceland trend (not shown). $^{208}Pb/^{204}Pb$ in samples from the southern Cape Verde Islands trend towards unradiogenic Pb compositions above the NHRL (Northern Hemisphere Reference Line, Hart *et al.*, 1992) (Fig. 9d). Santo Antão OV samples trend towards radiogenic Pb below the NHRL for $^{207}Pb/^{204}Pb$ and lie well correlated on the NHRL for $^{208}Pb/^{204}Pb$, whereas the intermediate and young samples lie on the NHRL for $^{207}Pb/^{204}Pb$ and below for $^{208}Pb/^{204}Pb$ (Fig. 9c and d). The Canaries and Santo Antão overlap in Pb isotopic composition. Whereas the Canaries are situated between St Helena [HIMU-type OIB (Zindler & Hart, 1986)] and the southern Cape Verde Islands in all diagrams in Fig. 9, the Santo Antão rocks have a component of variation perpendicular to the Canaries trend in Fig. 9e ($^{208}Pb/^{204}Pb$ vs $^{87}Sr/^{86}Sr$).

DISCUSSION

We first discuss magmatic evolution and the relative roles of fractional crystallization, magma mixing and crustal contamination. Mineral compositions are used for quantification of the liquid line of descent of the magmas and the primary magmatic compositions are derived. Mantle melting is subsequently discussed and the primary magmas are characterized. We then turn to the systematic changes in mantle melt compositions during the evolution of Santo Antão and identify the local end-members that explain the variation and relate these to global mantle components. Finally, we address plume–lithosphere processes and speculate on the origin of the Cape Verde mantle components.

Evidence for mineral–melt disequilibria

There is a lack of equilibrium between some of the phenocrysts of olivine and clinopyroxene and their host rocks as illustrated by an up to threefold variation of Fe/Mg_{ol} and up to tenfold variation of Fe/Mg_{cpx} in individual rocks. This cannot be a result of changes in melt composition during closed-system fractional crystallization because clinopyroxene zonation is abrupt and commonly reverse. Neither could the olivines conceivably have formed from melts at elevated pressures >1 GPa, where $K_{ol/melt}$ is higher (Ulmer, 1989), because low-pressure crystallization is invariably indicated by the low Al contents of all clinopyroxenes. Although some samples have accumulated crystals and this can explain apparent host rock–mineral disequilibrium, others with too Fe-rich or too Mg-rich olivines in rocks with only modest amounts of phenocrysts cannot be explained in this way. This, together with the reverse zonation of some clinopyroxenes in many rocks, the occurrence of Fe–Ti oxides in chromite-bearing MgO-rich rocks, and chromite in relatively evolved magmas with 7–8% MgO, indicates that many crystals are xenocrysts. Green clinopyroxene cores in relatively primitive lavas are commonly identical to equilibrium phenocrysts in phonolites. The rock trends, such as FeO–MgO and CaO–MgO (Fig. 5), however, allow only a small fraction of phonolite in any mixture with primitive magma and mixing seems, in general, not to be volumetrically important for Santo Antão magmas. It seems likely that the xenocrysts were generally mobilized from semi-solid cumulates by rising magma, or sank into relatively primitive dense magma in a stratified magma chamber from overlying more evolved, buoyant magma.

Magmatic differentiation

Olivine

The wide spectrum of volcanic rocks, from picrites to phonolites, on Santo Antão demonstrates the operation of fractional crystallization. The most magnesian olivine phenocrysts ($Fo_{88\text{-}91}$ with Ni = 1800–3400 ppm) have higher CaO contents than typical mantle olivine (Larsen & Pedersen, 2000). This suggests that essentially unmodified mantle melts were emplaced into the shallow crust. The wide compositional range of olivines in many samples indicates that truly comagmatic suites may not be found, as implied by the occurrence of mineral disequilibrium discussed above. Constant whole-rock SiO_2 and FeO^{total} within the various volcanic groups for MgO > 10%, accompanied by rising TiO_2 and CaO and decreasing Ni with falling MgO, attest to forsteritic olivine control. Olivine is accompanied by traces of chromite and Cr decreases strongly with MgO. Samples with >11% MgO have 1–40 vol. % phenocrysts and many of these are probably xenocrystal. Simple calculations of the MgO content of the melt by subtraction of olivine phenocryst compositions from the host whole-rock compositions yield a maximum of 12·4% MgO for the matrix. This implies that primary melts may have had at least 12% MgO.

Clinopyroxene

The decrease in whole-rock Sc and CaO starting at 8–10% MgO shows that clinopyroxene began to fractionate at this stage. It is, therefore, clear that mainly olivine controlled the major element variation for MgO >8%. Ti substitution in clinopyroxene controls the Al variation and reflects the magmatic evolution of Ti, whereas Al in clinopyroxene is uncorrelated with Al in the magmas. Moreover, the variation in Al/Ti ratio from 2 to 4 in the most primitive diopsides is similar to the variation of this ratio in the primitive melts. $K_d(Ti)_{cpx/rock}$

values were calculated for clinopyroxenes found to be in approximate equilibrium with their host rocks (assuming $K_d(Fe/Mg)_{cpx/rock} = 0{\cdot}20$–$0{\cdot}35$). There is an increase in $K_d(Ti)_{cpx/rock}$ from around 0·5 to 0·6 [higher than reported values of 0·2–0·4 (e.g. Hart & Dunn, 1993; Halliday *et al.*, 1995)] in the interval 8–6% MgO. Ti becomes compatible in the more evolved magmas with <6% MgO, reaching $K(Ti)_{cpx/melt} \approx 2$ in the phonolites. The maximum TiO_2 content in these clinopyroxenes occurs when Mg-number is around 70 (67–73). The maximum whole-rock TiO_2 occurs in rocks with Mg-number (Fe^{total}) = 44 (42–45). This allows the distribution of Fe/Mg to be calculated; $K(Fe^{total}/Mg)_{cpx/melt}$ $\sim 0{\cdot}33 \pm 0{\cdot}03$, which is somewhat higher than the value of $0{\cdot}23 \pm 0{\cdot}05$ reported by Grove & Bryan (1983) and Sack & Carmichael (1984). The difference in partitioning of Zr and Hf between clinopyroxene and melt is also noteworthy. Below 8% MgO, the Zr/Hf ratio steadily increases from around 41 to 60–70 in phonolites, indicating that Hf is less incompatible than Zr, as also reported by Hart & Dunn (1993).

The wide range of element concentrations at MgO >9%, reaching fourfold variation for some incompatible elements, cannot be explained by fractionation of the mineral phases present. This is evidence that parental melt compositions were far from constant.

Other phases

The spinel crystallization gap expected between the crystallization of chromite and titanomagnetite (Irvine, 1967; Sack & Ghiorso, 1991) is missing and probably reflects the highly oxidized nature of the magmas; this is evident from the high Fe^{3+}/Fe^{2+} ratio in the bulk rocks ($Fe^{3+}/Fe^{total}_{median} = 0{\cdot}44$, $Fe^{3+}/Fe^{total}_{min} = 0{\cdot}26$) and clinopyroxenes ($Fe^{3+}/Fe^{total}_{median} = 0{\cdot}59$, $Fe^{3+}/Fe^{total}_{min} = 0{\cdot}20$). Chromite ceases to crystallize when clinopyroxene starts and subsequently clinopyroxene accommodates Cr. The continuous spinel crystallization could be explained if titanomagnetite was already a (possibly minor) liquidus phase at this early stage of evolution (~8% MgO), which is clearly indicated for the most silica-undersaturated magmas by inflections in variation diagrams for SiO_2, FeO, TiO_2 and V (Figs 5 and 7). This indicates that the majority of the magmas were more oxidized than the OV magmas that fractionated Fe–Ti oxides from melts with 5–6% MgO. Mg-number (Fe corrected) decreases over the entire range of MgO contents but only slightly in the interval 6–3% MgO. This would indicate that, at this stage, Fe–Ti oxides make up a large proportion of the crystal fractionate. Major element mass balance calculations show that ~7% Fe–Ti oxide crystals and ~33% ferromagnesian minerals, mainly clinopyroxene, could have been extracted from the magma in this MgO interval. With compositions close to the host melts, large amounts of amphibole would need to fractionate to significantly change melt compositions, but only small amounts can be accommodated in incompatible element modelling and amphibole rarely constitutes a large proportion of the phenocryst assemblage. This is in accord with the lack of evidence for noteworthy amphibole fractionation in the variation diagrams (Figs 5 and 7). The initiation of apatite fractionation is clearly marked by the inflection in the P_2O_5 trend at 5–6% MgO. Titanite fractionation is probably responsible for the trend in the young volcanic rocks of declining Nd, Y and HREE and stable levels of La and Ce from 4–5% MgO (Fig. 6). Whereas plagioclase is rarely present in the evolved rocks, sanidine does occur and clearly fractionated in magmas with <1% MgO, as demonstrated by the decreasing Sr and Ba contents. Nb is relatively low in some phonolites and is decoupled from HREE variation. This probably reflects the fractionation of pyrochlore, although this phase has not been observed petrographically.

The evolved magmas

Rb and Th remain incompatible throughout the fractionation range. Rb is used as an index of differentiation because the XRF analytical precision for Rb is far better than that for Th in the primitive rocks (Th is analysed by INAA in only a third of the samples), and the trend for Rb (Fig. 6a) is as good as for other incompatible elements. We have assumed that any evolved compositions that occur within a sequence of volcanic rocks with closely related geochemical features belong to the same magmatic suite. The locations of inflections in variation diagrams reflect the onset of crystallization of various phases in the evolving magmas. The wide range of magma compositions observed can be divided into two broad trends: one for magmas derived from nephelinitic parent magmas (the nephelinite trend), and one for the basanitic parent magmas (basanite trend). These magma differentiation trends become much more distinct at the most evolved end of the compositional spectrum (Fig. 10a). At 65 ppm Rb (≈5% MgO, Fig. 6), Y (Fig. 10d), Ce, Nd, HREE and Zn all become compatible in many nephelinite-trend magmas, as discussed above, and at ≈75 ppm Rb for some basanite-trend magmas. At ≈115 ppm Rb, decreasing Ba and Sr mark the start of sanidine crystallization; La, Nb and Ta become compatible and Nb/Ta increases, probably marking the start of titanite fractionation. Plagioclase did not fractionate in significant amounts for the majority of the Santo Antão magmas and sanidine fractionated only during extremely advanced stages of crystallization (with <1% MgO). The proportion of felsic fractionating phases increased at around 5% MgO (Fig. 3) and 70 ppm Rb, but this is not evident in Fig. 6. However, a decrease in SiO_2/Al_2O_3 (not shown) from 4–5 at high MgO to ~2·8 for MgO < 5% is caused by the co-fractionation of olivine and clinopyroxene which ceases at this stage of

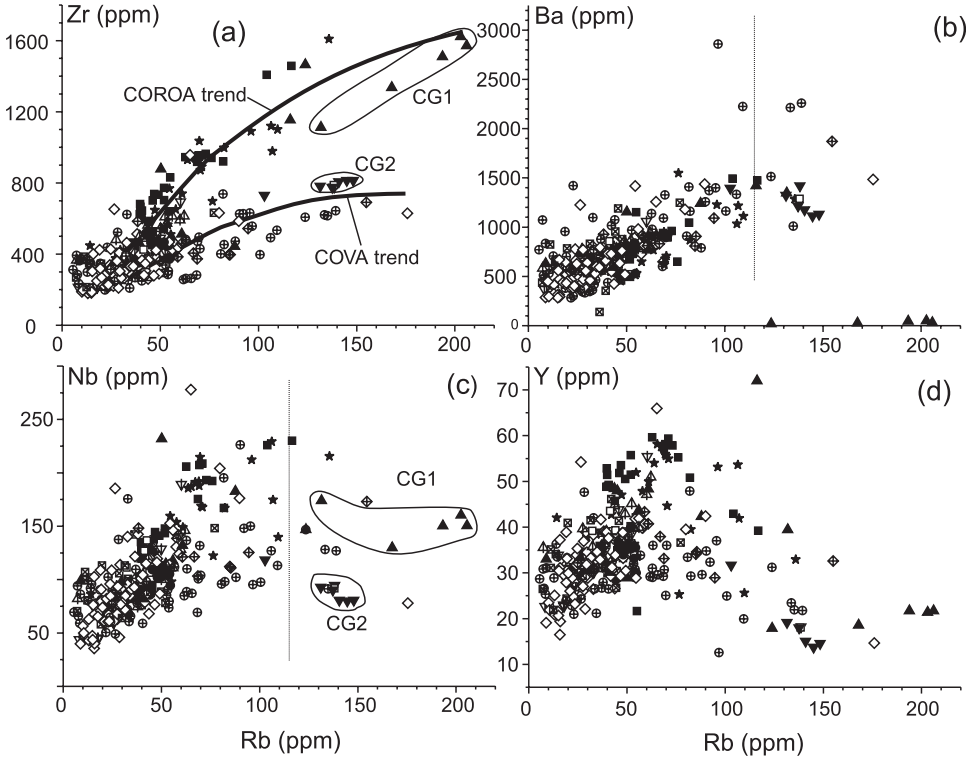

Fig. 10. Variation of Zr, Ba, Nb and Y vs Rb (ppm). Older and intermediate age rocks follow the basanite trend (COVA), whereas most younger and more enriched rocks follow the nephelinite trend (COROA) (see text for explanation). Vertical lines in (b) and (c) mark inflections discussed in the text. Fields for the Cão Grande pumices CG1 and CG2 from Western Santo Antão are marked in (a) and (c). Symbols as in Fig. 2.

evolution, after which SiO_2/Al_2O_3 remains fairly constant at 2·4–2·8.

Modelling magmatic differentiation processes

We have adopted a broad approach for discussion of the liquid line of descent of the Santo Antão magmas. In general terms, one may consider that there are two dominant magma types at Santo Antão: a younger nephelinitic low-silica type (LAGOA, COROA, PRC, CAD & BOR) and an older basanitic type (OV, OAN, COVA, AN & FRA) with distinctly higher SiO_2 and less enrichment in incompatible elements (Figs 5 and 6). Both magma series evolve towards phonolite, but the nephelinite trend is characterized by high Zr and Th, with up to twice the amounts in the basanite trend at all stages of magmatic evolution (Fig. 6). It is evident that the CG1 (Cão Grande pumice no. 1) sequence of phonolitic pumice belongs to the nephelinite trend, whereas the subsequent CG2 (Cão Grande pumice no. 2) represents a late example of a basanite-trend evolved magma-type which is otherwise typical for the COVA and FRA groups (Fig. 10a).

Two models for the liquid line of descent demonstrate the evolution of the two main magma series. The melilite nephelinites–phonolites of the nephelinite trend (COROA, PRC) and the basanites–phonolites of the basanite trend (OV, COVA) span the entire range of geochemical variation for most elements, and we have modelled the evolution of two primitive melt compositions. Fractional crystallization of the magmas was modelled in steps of 1% crystallization for chosen parental magma compositions, melilite nephelinite 110052 and basanite 111750. The equilibrium mineral compositions were calculated for each step based on mineral/melt distribution coefficients for Fe/Mg, and the mineral compositions parameterized as functions of Fe/Mg based on the measured mineral compositions. This allows the large and non-monotonous variation in, for example, TiO_2 and Al_2O_3 in clinopyroxene and spinel minerals to be appropriately incorporated into the fractionation modelling. The fractionating mineral assemblage was assessed from the observed phenocryst assemblages (Fig. 3) and whole-rock geochemical features, such as inflections on variation diagrams (Fig. 4). The results for fractionation in the interval ~12–5% MgO are reported in Table 4. For the most evolved rocks, magmatic evolution may be monitored by the incompatible elements Rb (Fig. 10) and Th; these results are reported in Table 4. For the nephelinite parental melt, 12% olivine fractionation is modelled before 8% fractionation of the

Table 4: Calculated liquid line of descent and fractionation assemblages for the two rock series of Santo Antão

Remaining melt (%)	Crystallized (%)	MgO at start (wt %)	Observed Rb[1] (ppm)	Relative abundance of minerals in fractionate (wt %)					
				Olivine	Clinopx	Fe–Ti-ox	Amph	Haüyne	Apatite
Nephelinite–phonolite/the COROA trend									
100	12	11·6	45	100					
88	3	6·9	51	23	68	9			
85	5	6·5	53	18	55	27			
80	5	6·0	56		64	18	18		
75	10	5·7	60		54	13	22	11	
65	5	5·0	69		51	12	20	10	6
60	40	4·8	75						
20		0·1	225						
Basanite–phonolite/the COVA trend									
100	10	12·2	29	100					
90	5	8·3	29	50	50				
85	5	7·1	31	33	67				
80	5	6·2	33		67	11	22		
75	5	5·9	35		60	20	20		
70	15	5·6	37		67	11	22		
55	15	4·4	47		63	11	21		5
40	19	2·5	65						
21		0·5	135						

[1]Average Rb in rocks with approximately the given MgO.

assemblage olivine + clinopyroxene + magnetite with an increasing relative amount of magnetite. Amphibole, haüyne and apatite fractionation set in after 20, 25 and 35% crystallization, respectively (Table 4). After 40% fractionation, the remaining melt has 4·8% MgO. For the basanite parental melt, Fe–Ti oxide fractionation starts relatively late: 10% olivine is followed by 10% olivine + clinopyroxene, and then 25% clinopyroxene + Fe–Ti oxide + amphibole. After another 15% fractionation of the same assemblage plus apatite 2·5%, MgO remains in the melt (Table 4). Around 80% fractionation is required to produce both the COVA phonolite (114829/COVA) from a parental OV basanitic magma and the phonolitic Plinian pumice (e.g. 106455/YTAR) from a young nephelinitic parental magma.

Negligible crustal contamination

Because of the very high levels and large variability of lithophile elements in the most primitive magmas, considerable amounts of crustal contamination may have occurred without leaving an imprint on the trace element chemistry. Additionally, there is no correlation between isotopic composition and the degree of magmatic evolution. Janney & Castillo (2001) showed that Atlantic oceanic crust older than 120 Ma was plume-contaminated with an overall EM1 isotopic composition. The sea-floor beneath Santo Antão is slightly younger than 118 Ma, which is the age of magnetic anomaly M0 (Harland *et al.*, 1990) that runs immediately east of the island (Williams *et al.*, 1990). The samples of Jurassic sea-floor reported by Gerlach *et al.* (1988) from Maio and Santiago do not have isotopic compositions like those of Janney & Castillo (2001). The Santo Antão rocks do not trend towards isotopic compostions with the character of any of these sea-floor samples.

In the primitive rocks, Ce/Pb ranges from 28 to 63 (primitive mantle, PM ≈ 25; Sun & McDonough, 1989), K/Nb = 26–323 and Th/Nb = 0·05–0·1 (Th/Nb_{PM} = 0·12; Sun & McDonough, 1989). Continental crust and clastic sediments typically have lower Ce/Pb (<10), higher K/Nb (>1000) and higher Th/Nb (>0·4) (Rudnick & Fountain, 1995). The local basement is thought to be mainly basaltic but a Mesozoic sediment cover is present on some of the Cape Verde islands because of the proximity to the African continent (Mitchell-Tomé, 1976; Stillman *et al.*, 1982; Ali *et al.*, 2003).

Hydrothermally altered oceanic crust has high $^{87}Sr/^{86}Sr$ relative to $^{143}Nd/^{144}Nd$ because of very high Sr/Nd and $^{87}Sr/^{86}Sr$ (~0·709) in seawater. No samples have particularly high $^{87}Sr/^{86}Sr$ compared with

$^{143}Nd/^{144}Nd$ in Fig. 9a. It is therefore clear that neither trace elements nor Sr, Nd and Pb isotopes suggest any significant influence from continental or altered oceanic crustal material on the composition of Santo Antão magmas.

Mantle melting

Range of variation of primitive magma compositions

To model the composition of the mantle source of the magmas, we have attempted to remove the effects of crystal fractionation and accumulation in the magmas to enable us to obtain estimates of the primary mantle-derived melt compositions. The possible effects of alteration on the Fe^{3+}/Fe^{2+} ratios in the volcanic rocks, and the common occurrence of xenocrysts and/or accumulated olivine or clinopyroxene phenocrysts, make the identification of primary mantle-derived magma compositions from Fe/Mg ratio considerations rather unreliable. However, using a lower limit of $Fe^{3+}/Fe^{total} = 0{\cdot}27$ (for samples with MgO > 5%) as representative for the melts, and assuming $Fo_{\geq 88}$ in mantle olivine, the Fe/Mg_{wr} ratios indicate that rocks with less than ~9% MgO cannot represent melts in equilibrium with mantle peridotite. More magnesian mantle olivine or partial melting at high pressure with less fractionation of Fe^{2+}/Mg (Ulmer, 1989) would yield melts with higher MgO contents. On the other hand, the primary melts would have less MgO if they were more oxidized than inferred, as the high FeO^{total} caused by Fe^{2+}/Mg fixed in equilibrium with mantle olivine would cause calculation of too high MgO. Primitive compositions bracketed by Mg-number (for $Fe^{3+}/Fe^{total} = 0{\cdot}27$) = 65–76, Ni = 150–300 ppm and Cr = 250–1000 ppm have MgO = 9–15%. Earlier, we showed that the Santo Antão melts had up to at least 12·4% MgO. A moderate 5 vol. % subtraction or addition of equilibrium olivine will change the % MgO in the magmas by around 2%. Because the liquidus assemblages of most magmas with >~9% MgO are dominated by olivine, samples with MgO ≥9% should, therefore, resemble primitive mantle melts, except for the content of MgO and trace elements compatible in olivine and chromite.

Klein & Langmuir (1987) introduced a method for recalculation of evolved basaltic compositions to primitive compositions with 8% MgO. In order to compare rocks at different stages of evolution, we have chosen to recalculate the bulk-rock analyses to 12% MgO, and believe that for most elements, the results provide a reasonable approximation to the composition of the primary mantle melts. Magmas with >6·5% MgO appear to have had a relatively simple liquid line of descent (Table 4; Figs 5–7) and we have corrected 187 such rock compositions (103 with >9% MgO) by incrementally adding in 1% steps equilibrium olivine, clinopyroxene and titanomagnetite crystals in proportions as derived above for nephelinite and basanite, respectively, according to the two fractionation schemes in Table 4 or, for samples with >12% MgO, subtracted olivine (Fig. 11). The total correction for a bulk-rock analysis constituted either addition of 0–20% olivine ± clinopyroxene ± Fe–Ti oxide (Table 4), or subtraction of up to 20% olivine. Elements which are incompatible in this MgO range have been corrected accordingly. The corrections reduce element variation within the groups considerably, e.g. for TiO_2 in the OV, the range is lowered by 1% and the variance by 33% relative.

The corrected analyses have large variations in incompatible element concentrations [La_{12} = 31–138 ppm = 45–200 × primitive mantle (PM)]. Samples with >20% phenocrysts ($N = 38$) are highlighted in Fig. 11d; phenocryst accumulation effects seem to remain in only a few of the corrected analyses. The wide range of mantle–melt compositions is confirmed by the occurrence of olivine $Fo_{89–91}$ in many rocks with measured MgO ~ 12% (Fig. 11a).

There is a negative correlation between SiO_2 corrected to 12% MgO (hereafter referred to as Si_{12}) and Fe_{12} (Fig. 11a), Ti_{12} (Fig. 11b), P_{12} (Fig. 11c), La_{12} (Fig. 12d), Y_{12}, Nb_{12}, Th_{12} and Zr_{12}. There is also a positive correlation between pairs of most of these elements. There is a somewhat broader negative correlation of Si_{12} with Na_{12}, Sr_{12} and Pb_{12}, and no correlation with Ba_{12}, Rb_{12}, Ca_{12}, Al_{12} and K_{12}. These correlations are evidence for a coherent variation of many elements with time, and indicate that the major part of melt generation can be explained by rather few processes and materials.

Source mineralogy and depth of melt extraction

The systematic geochemical variation within the fractionation-corrected compositions shows that the more silica-undersaturated (i.e. low Si_{12}) rocks are also the most incompatible element-enriched and that there is a continuum of compositions between two end-members: a melilite nephelinite with $Si_{12} = 38$ (e.g. 114522/CAD, Table 1) and a basanite with $Si_{12} = 45$ (e.g. 111743/OV, Table 1) (Fig. 11a). All the nephelinitic rocks are relatively young, whereas all the OV rocks are basanitic. Because low Si_{12} is coupled with high FeO_{12} and unrelated to Ca_{12} content, there is no indication that the Santo Antão melts have a significant carbonatite component, although carbonatites occur on several of the Cape Verde islands. Highly alkaline melts, however, can be produced from CO_2-bearing mantle with amphibole or phlogopite at high pressures (Eggler, 1989; Wyllie, 1989; Hirose, 1997). The highly magnesian olivines, $Fo_{91–89}$, in rocks with both high and low Fe_{12} (Fig. 11a) are a clear indication that the most Fe-rich melts were not derived from a more Fe-rich mantle

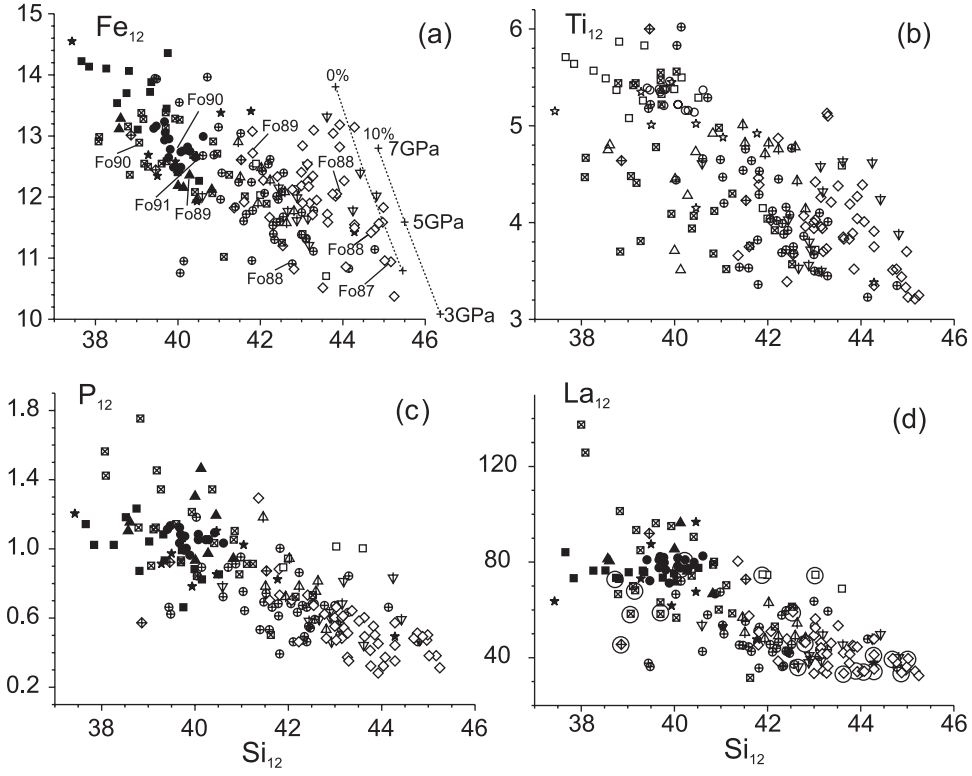

Fig. 11. Compositional variation of the most primitive samples corrected for fractional crystallization to 12% MgO. (a) FeO^{total} (labelled Fe_{12}) vs SiO_2 (labelled Si_{12}). Rocks with the most magnesian olivine phenocryst compositions in rocks with −12 wt % MgO are marked. Experimental melt compositions from melting of peridotite at 3, 5 and 7 GPa are shown for 10% partial melting and extrapolated to 0% melting (Walter, 1998). The effect of fractionation from 12 to 8% MgO for each sample corresponds roughly to the size of the data point. (b) Ti_{12} vs Si_{12}; (c) P_{12} vs Si_{12}; (d) La_{12} vs Si_{12}. Samples with >20% phenocrysts are highlighted with a circle. Symbols as in Fig. 2.

source. Instead, melts with low Si_{12} and high Fe_{12} are inferred to be derived from rather small degrees of partial melting at high pressure, consistent with the compositional trends of melts from high-pressure experiments (e.g. Hirose & Kushiro, 1993; Hirose, 1997; Walter, 1998). It should be noted that Fe^{total} in these experimental melts is significantly lower than that of the Santo Antão primitive magmas, possibly because no experiments yielded <10% melt. Al_{12} and Ca_{12}/Al_{12} ratios (Fig. 12) for the corrected Santo Antão high Fe_{12} compositions partially coincide with the experimental melt compositions at 3–4 GPa for 10% pyrolite melting (Walter, 1998) and extrapolations to zero per cent melting. The trend of the Santo Antão melts is sub-parallel to the vector for variation in degree of melting, whereas fractionation vectors are oblique to the trend. This may indicate that the Santo Antão melts were extracted from the mantle at 3–4 GPa (90–120 km) by variable degrees of partial melting. It is evident, however, that the experimental data cannot explain the full range of Santo Antão primitive magma variation (Fig. 12). Samples with high Ca_{12}/Al_{12} ratios of >1·4 are OV rocks with 15–25% clinopyroxene phenocrysts and crystal accumulation may readily explain the high values. However, sample 111820 with $Ca_{12}/Al_{12} = 1{\cdot}35$ is aphyric and thus a melt composition. Consequently, those Santo Antão corrected magma compositions with high Ca_{12}/Al_{12} plotting above the line for the initial melt compositions in Fig. 12 may indicate a relatively high clinopyroxene/garnet ratio in the melting mode compared with the experiments of Walter (1998). Comparison of the Santo Antão samples (fractionation corrected) with the melting experiments of Walter (1998) with respect to TiO_2 indicates low degrees of melting (<10%), or a source with $TiO_2 > 2 \times$ pyrolite.

The fractionation of HREE in the magmas is smaller ($Sm/Yb_{rock} < 9$ and $Tb/Yb_{rock} < 1{\cdot}0$; Fig. 13) than expected for melts in equilibrium with residual assemblages very rich in garnet (Putirka, 1999). Eclogite or pyroxenite sources therefore seem to be excluded, favouring a lherzolitic mantle source.

In Fig. 13, we compare the REE contents of Santo Antão fractionation corrected primitive melts with mantle melts modelled by decompression and aggregated incremental non-modal batch melting of an upwelling mantle source with a porosity of 0·3%. A first model mantle source (PMDM in Fig. 13) was calculated as a mixture of depleted mantle (DM) and primitive mantle (PM) in proportions based on the Nd isotopic

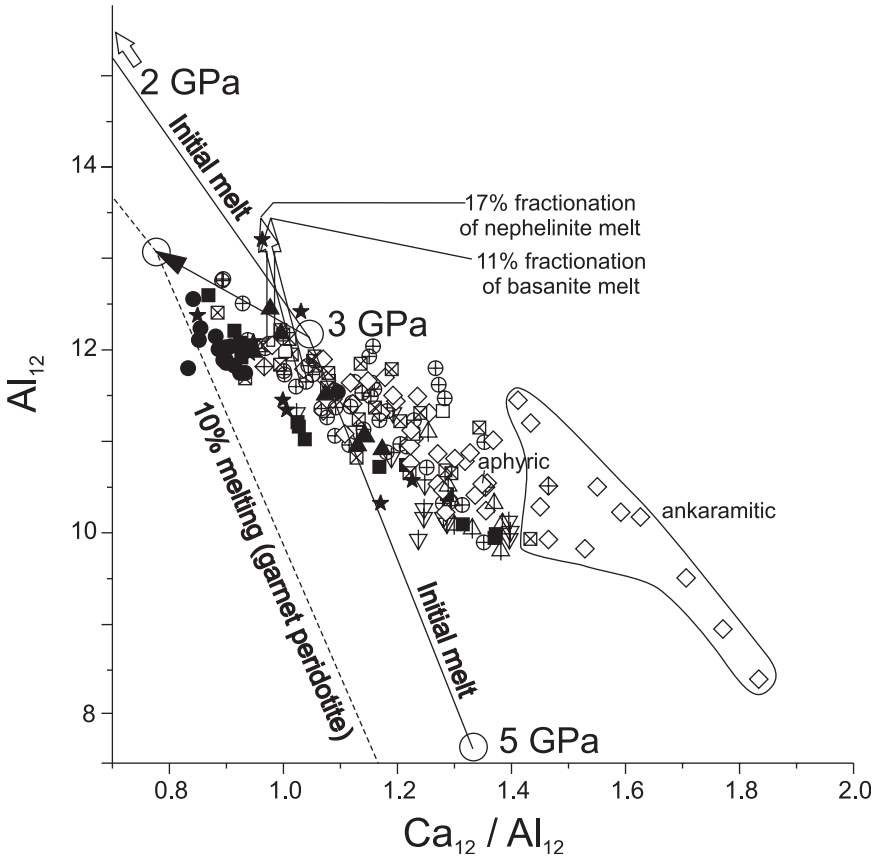

Fig. 12. Al_2O_3 vs CaO/Al_2O_3 for fractionation-corrected compositions (labelled Al_{12} vs Ca_{12}/Al_{12}). Comparison between fractionation-corrected compositions and experimentally derived melts for pressures of <3–5 GPa by (1) 10% melting (Walter, 1998)—dashed line, and (2) melt compositions extrapolated by us to zero per cent melting—continuous line. The Santo Antão volcanic rocks overlap with small degree melts from experiments at 3–4 GPa. Open arrows show the effect of fractionation of the magma from 12 to 8% MgO. Black arrow indicates compositional change by increasing melting at 3 GPa (garnet peridotite), using data of Walter (1998) and our extrapolation. The field marked 'ankaramitic' includes rocks with accumulations of up to 40% clinopyroxene phenocrysts. Sample 111820 is marked 'aphyric' and is an example of a melt composition with high Ca_{12}/Al_{12}. See text for discussion. Symbols as in Fig. 2.

composition of the sample, following the approach of McKenzie & O'Nions (1995) (see also Appendix B). The mantle source and melting modes are according to McKenzie & O'Nions (1995) and have 10% garnet at high P; we also show results for mantle with 5 and 20% garnet. Three model mantle compositions are used: one intermediate between depleted and primitive mantle, a melt-enriched mantle and a third comprising addition of 1 ‰ Cape Verde carbonatite to a depleted mantle protolith. Melt compositions derived by model mantle rising through the garnet–spinel transition are shown in Fig. 13b.

The modelled REE systematics suggest that the Santo Antão melts were derived by melting of 1–4% peridotite in the garnet stability field or at the transition to the spinel peridotite field. The negative correlation within the various groups between Sm_{12}/Yb_{12} ratio and Yb_{12} in Fig. 13b indicates that melt extraction may have taken place close to the garnet–spinel transition, where Yb is released as garnet is eliminated from the source. The relative positions of the groups indicate that the young volcanic rocks require a more enriched source than the OV because they have higher Sm_{12}/Yb_{12} for the same degree of melting than the older rocks (OV or COVA). This is strong evidence that a cusp on the solidus at the garnet–spinel transition is the locus for much of the melting under Cape Verde. The curves in Fig. 13b are calculated for a rising mantle that melts by decompression with a melting rate according to Langmuir *et al.* (1992) and using the partitioning coefficients of Halliday *et al.* (1995), Appendix B. For this model with $T_{pot} = 1470°C$, the garnet–spinel transition takes place 88–95 km below the surface (McKenzie & Bickle, 1988), which is in accordance with the depths indicated in Fig. 12. Use of the high $K_d(\text{M-HREE})_{\text{clinopyroxene/melt}}$ values of Blundy *et al.* (1998) will have a significant effect on the inferred source concentrations, but little effect on implied melting pressures. A carbonatite-enriched source cannot produce the

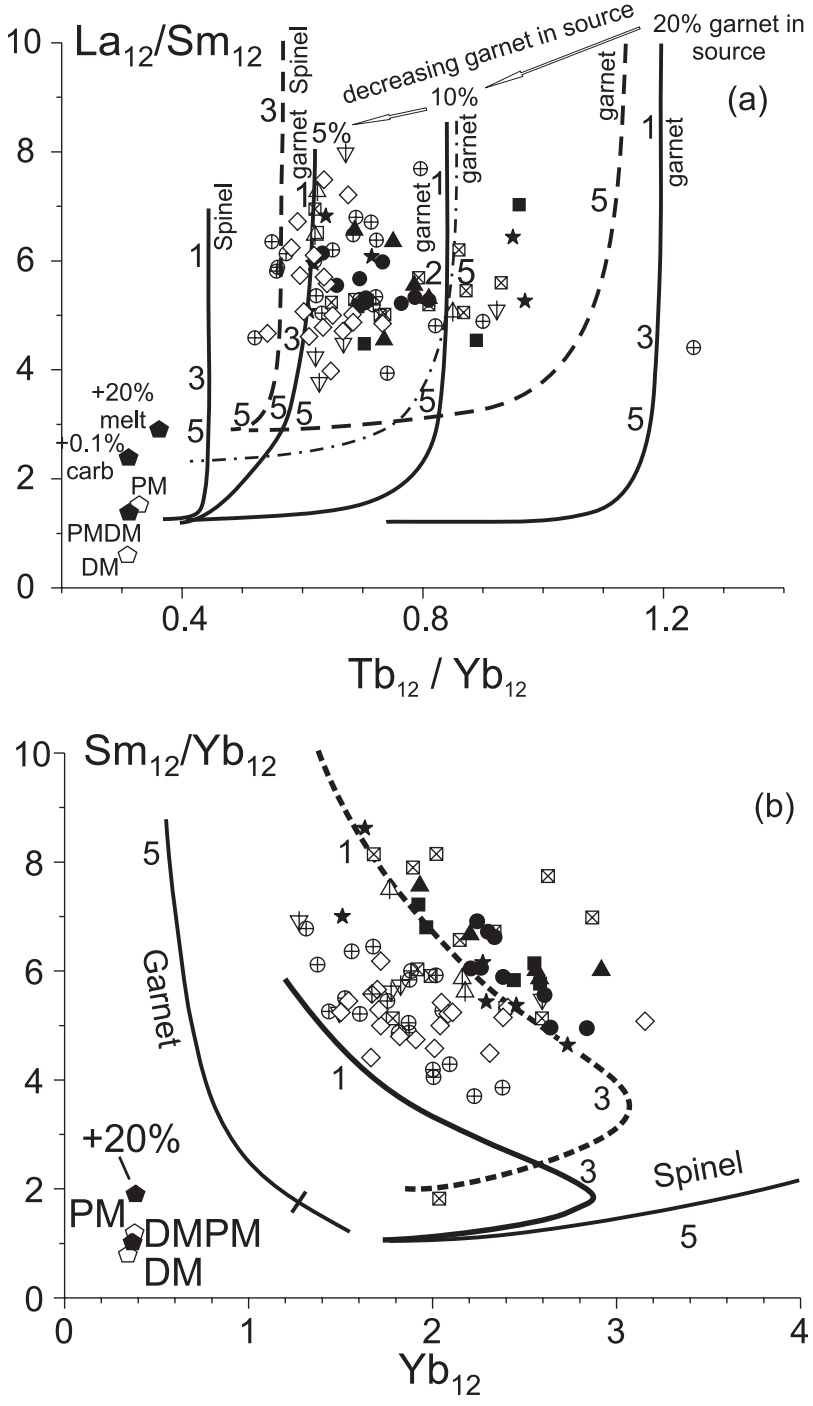

Fig. 13. Variation of (a) La_{12}/Sm_{12} vs Tb_{12}/Yb_{12} and (b) Sm_{12}/Yb_{12} vs Yb_{12} for fractionation-corrected primitive compositions. For a model mantle intermediate between PM (primitive mantle) and DM (depleted mantle), PMDM (45% PM + 55% DM), melt trajectories are shown as continuous curves in (a) for melts entirely derived in the garnet and the spinel stability field, respectively. A second model mantle was calculated by addition to PMDM of 20% melt derived by 5% melting of a garnet peridotite MORB source (+20% melt); melts of this source are shown with dashed curves. A third model mantle is DM-enriched by 1‰ Cape Verde carbonatite—dot–dash curves show melts derived with residual garnet. Numbers next to curves mark the percentage of partial melting by aggregated incremental non-modal batch melting. Melting curves for garnet peridotite PMDM are shown for mantle with 5, 10 and 20% garnet, and 10% garnet for the '+20%' and '0·1% carbonatite' sources. (b) Trajectories of decompression melting curves for upwelling mantle (PMDM—continuous curve, and DM+20% melt—dashed curve) crossing the garnet–spinel transition of a peridotite with 10% garnet. Melting of PMDM entirely in the garnet and spinel stability fields is shown by curves marked 'garnet' and 'spinel', respectively. See text for discussion. Symbols are as in Fig. 2.

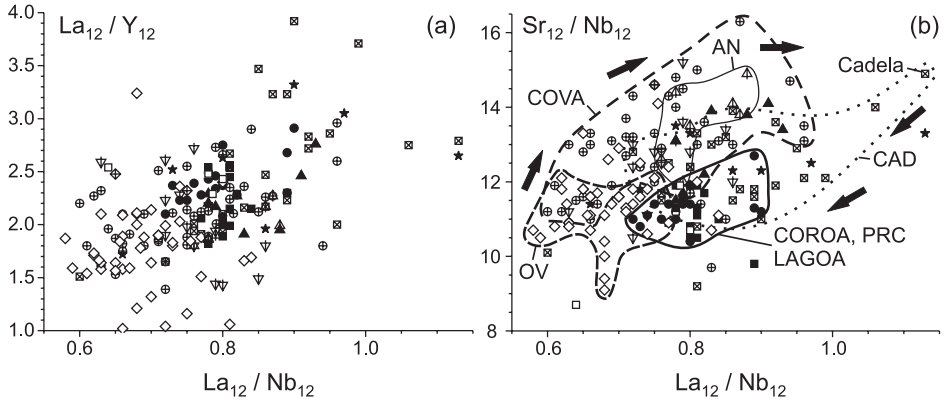

Fig. 14. (a) La_{12}/Y_{12} vs La_{12}/Nb_{12} for fractionation-corrected compositions. The samples display a positive correlation. Variation of La/Nb is evidence for compositional variation in the source, as this ratio is not expected to fractionate during melting. The least incompatible element-enriched samples of the OV generally have the lowest La/Nb. (b) Sr_{12}/Nb_{12} vs La_{12}/Nb_{12} for fractionation-corrected compositions. The melt compositions change with time, as indicated by the arrows. The marked fields represent 90% of the samples within a group. Symbols are as in Fig. 2.

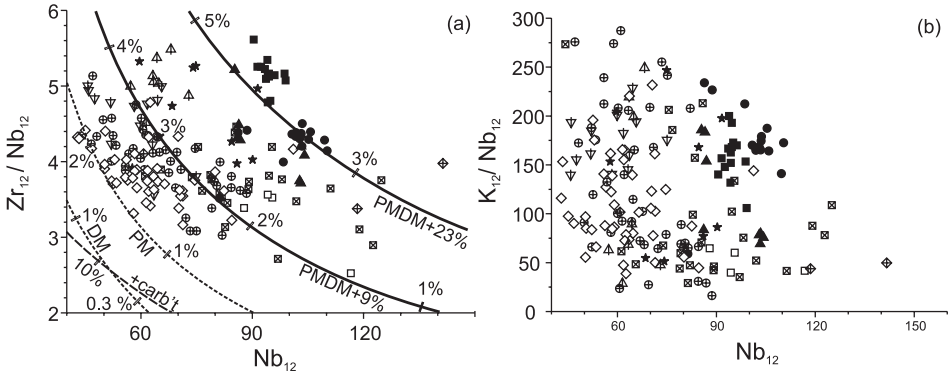

Fig. 15. (a) Zr_{12}/Nb_{12} vs Nb_{12} for fractionation-corrected compositions. Model melts from variably incompatible element-enriched sources indicate that Santo Antão melts were derived from 2–5% melting of sources variously enriched by silicate melt and not by carbonatite. Curves are marked with source compositions: DM, depleted mantle; PM, primitive mantle; PMDM +9/+23%, a mixture of 45% PM + 55% DM to which is added 9/23%, respectively, of silicate melt derived from DM with residual garnet; carb't, 0·1% carbonatite added to DM. A carbonatite-enriched source generates melts with high Nb and low Zr/Nb compared with a silicate-enriched source. Details of the melting modelling as for Fig. 14. See also text for discussion. (b) K_{12}/Nb_{12} vs Nb_{12} for fractionation-corrected compositions. There is no correlation but an overall increase of K_{12}/Nb_{12} with decreasing Nb_{12} for the sample groups suggesting melting of sources with a residual K-bearing mineral. See text for discussion. Symbols as in Fig. 2.

Santo Antão melt compositions, because calculated melts with the appropriate La_{12}/Sm_{12} of 4–8 (Fig. 13a) have too low Sm_{12}/Yb_{12} for any values of Yb_{12}. The twofold variation of La_{12}/Nb_{12} in the Santo Antão magmas is broadly correlated with a twofold variation of La_{12}/Y_{12} (Fig. 14a). This clearly demonstrates that relative La enrichment in the source (Fig. 13a) is a significant cause of variation and additional complexity (i.e. a source with elevated La/Sm) should be added to improve modelling of the data in Fig. 13a, and this may explain why slightly less melting is indicated in Fig. 13b than in Fig. 13a.

Source enrichment and extent of melting

Correlations in mantle-derived melts between incompatible trace element ratios, such as La/Nd and Zr/Nb, may reflect differences in melt–crystal partitioning of these elements and thus be related to the degree of melting; they could, however, also reflect compositional variation in the mantle source. The relationship between mantle source composition and degree of melting is highlighted in a diagram of Zr_{12}/Nb_{12} vs Nb_{12} (Fig. 15a) where melting trajectories have been modelled as for the REEs above. The curvatures of the calculated melting trajectories depend on the ratio of the partition coefficients for Zr and Nb and are expected to be rather constant, whereas the positions of the curves depend on the Zr and Nb contents of the source. We have modelled the mantle sources to make the calculated melts fit the Santo Antão data (Fig. 15). It is evident that the majority of samples in each group could have been generated within a limited range of melting of a specific source.

The OV require the least-enriched source (low Nb_{12}), although still more enriched than primitive mantle, whereas the young COROA and LAGOA volcanic rocks appear to be derived from a highly incompatible element-enriched source. An intermediate source enrichment is indicated for the COVA and BOR groups (2–0·7 Ma) (Fig. 15). The source enrichment was by silicate melts rather than carbonatitic fluids, because Cape Verde carbonatites are enriched in Nb and have too low Zr/Nb ratios to generate both relatively high Zr/Nb and high Nb, unless much larger degrees of melting took place than indicated by the REE (average composition of selected pristine Cape Verde carbonatites: 154 ppm Nb, Zr/Nb = 0·4; Jørgensen, 2003). Although it is evident from Fig. 15 that the COROA and LAGOA rocks are not comagmatic, they could be derived from similar sources by different degrees of melting; the AN and CAD melts could be derived from a less-enriched source by relatively large (3–5%) and small (1–3%) degrees of melting, respectively. Additional evidence in support of variable degrees of melting being a major factor in explaining the Zr_{12}/Nb_{12} variation comes from a well-defined negative correlation between La_{12}/Nd_{12} and Zr_{12}/Nb_{12} ratios (not shown) for samples situated along the model melt curves in Fig. 15 and from the groupings of data in Figs 13 and 14. Si_{12} shows no systematic variation with degree of melting as derived from Zr–Nb modelling, when comparing the relative positions of the sample groups in Figs 11 and 15. Constant silica in small-degree melts would imply that the melts were derived over a relatively small depth range.

Highly incompatible element ratios, or ratios of elements with near identical incompatibility, are expected to be little or unfractionated relative to the mantle source, and the variation of ratios such as La_{12}/Nb_{12}, Sr_{12}/Nb_{12}, Ba_{12}/Nb_{12}, K_{12}/Nb_{12}, Sr_{12}/Nd_{12}, Sm_{12}/Hf_{12}, Zr_{12}/Hf_{12} and Nb_{12}/Ta_{12} would therefore indicate compositional variation in a lherzolitic source. In the primitive rocks, measured Zr/Hf = 40 ± 3 and Nb/Ta = 18 ± 2 are close to primordial mantle values (Sun & McDonough, 1989) and show no variation related to sample groups. La_{12}/Nb_{12}, on the other hand, shows a twofold range of variation between 0·57 and 1·13 (Fig. 14a). In general, rocks most enriched in incompatible elements have the highest La_{12}/Nb_{12} ratios (i.e. the LAGOA, COROA, PRC and CAD groups). The same trend is evident for La_{12}/Sr_{12} ratios, and this further indicates that the La variation could be a source feature, because Sr is significantly less incompatible than La and would be relatively sensitive to the degree of melting. It appears that the relative enrichment in some groups is related to higher LREE/HFSE, and perhaps LREE/LILE ratios, although other LILE such as Ba, and especially K and Rb, show uncorrelated variations. The Sr_{12}/Nb_{12} ratios (Fig. 14b) reach a low value of 8·6 in the OV but there is complete overlap of OV with the COROA and LAGOA groups, which mainly have Sr_{12}/Nb_{12} = 10–12 (but higher La_{12}/Nb_{12}). The northern CAD and AN groups, which on the basis of their Zr/Nb ratios are inferred to be derived by contrasting degrees of melting, are both distinguished by relatively high Sr_{12}/Nb_{12} (up to 15), which is still lower than PM (primitive mantle) or MORB values of ~30. This indicates that there is a general enrichment in Nb in all the Santo Antão rocks, and a relative enrichment of Sr in CAD and AN, and that CAD, COROA and LAGOA are even more enriched in LREE. Sr/Nd in all samples is around mantle values of ~15 (Sun & McDonough, 1989) and ranges between 10 and 20. It has been suggested that low Sr/Nd ratios in alkaline Icelandic lavas are derived from basaltic mantle sources (Chauvel & Hemond, 2000), but no such component is indicated for Santo Antão.

A potassic phase in the mantle source

The majority of the studied samples (75%) show a correlation between measured Rb and K (r^2 = 0·8) and have an average K/Rb = 345 ± 16, which is not very different from the primordial mantle value of 394 (Sun & McDonough, 1989), and are thought to be only very slightly altered. Most of the remaining samples have relatively low K contents and may have undergone significant secondary alteration. A similar distribution was found by Gerlach *et al.* (1988) for samples from five of the Cape Verde Islands. However, K_{12}/Nb_{12} ratios among the freshest samples vary widely (26–323), which is typical for HIMU OIB (Fig. 8; Thirlwall, 1997) and consistently lower than K/Nb_{PM} = 350 and K/Nb = 450 in Mid-Atlantic MORB (Dosso *et al.*, 1993). There is no clear correlation between Nb_{12} and K_{12}/Nb_{12} ratios (Fig. 15b) but a decrease in range of K_{12}/Nb_{12} with Nb_{12}. A residual potassic phase in the source may, therefore, explain the variation, but quantification is not possible. Other anomalous trace element ratios in the Santo Antão volcanic rocks, such as high Th/U (4–79), Ce/Pb (40–60) and U/Pb ($\mu = {}^{238}U/{}^{204}Pb$ = 18–71), may also be caused by such a phase.

Temporal changes in composition of the mantle source

Within the context of relatively radiogenic Pb isotope compositions, there is a significant time-related change in the isotopic (Sr–Nd–Pb) and elemental compositions of the Santo Antão magmas, which is marked by the successive appearance of additional isotopic components that mixed with, or superceded, those which contributed to the previously erupted magmas. Overall, Pb isotope ratios in the source and in the Santo Antão volcanic rocks developed in mantle regions with relatively high μ (also

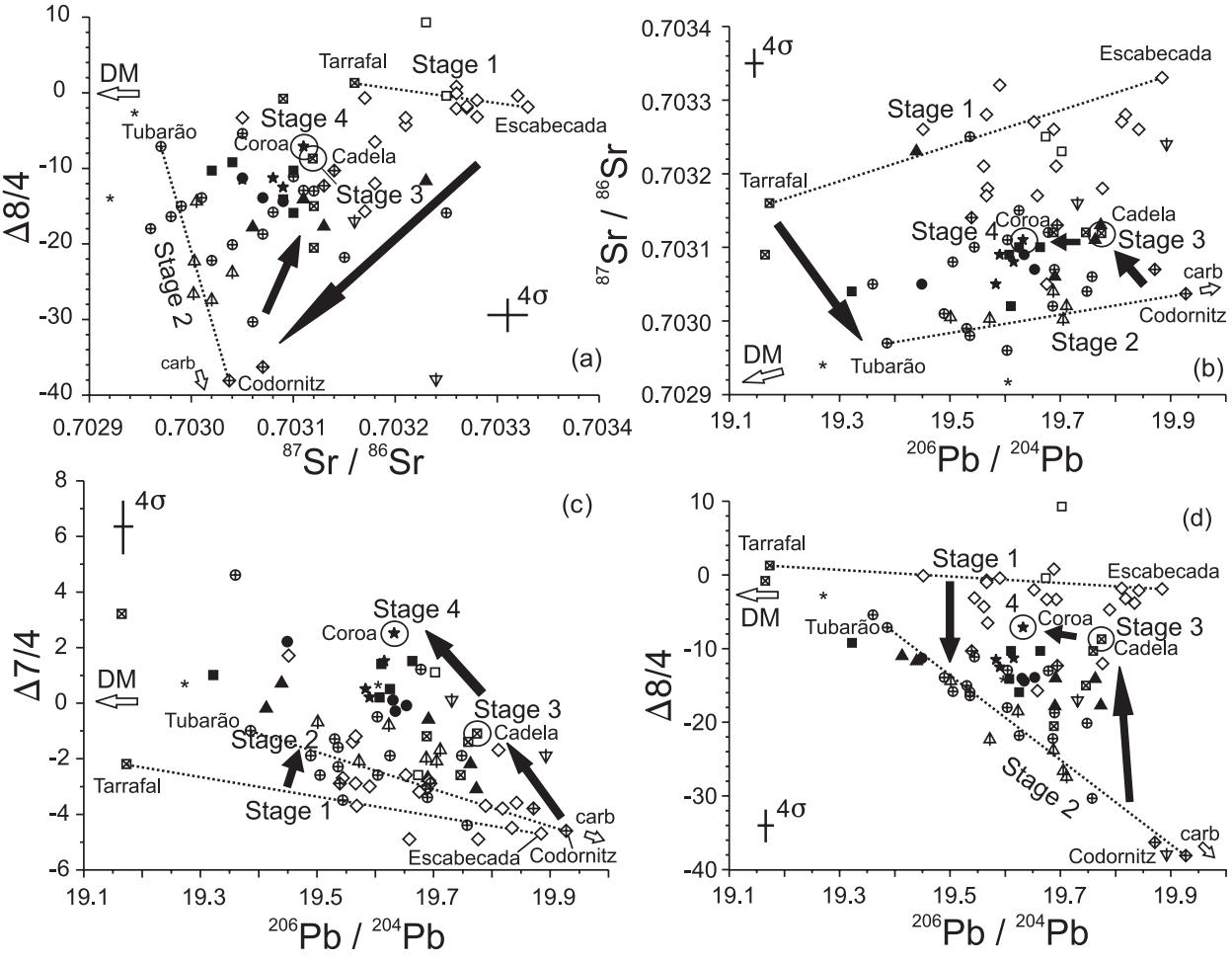

Fig. 16. Isotope variation in the Santo Antão volcanic rocks with suggested approximate mixing lines and end-members. (a) Δ8/4 vs $^{87}Sr/^{86}Sr$; (b) $^{87}Sr/^{86}Sr$ vs $^{206}Pb/^{204}Pb$; (c) Δ7/4 vs $^{206}Pb/^{204}Pb$; (d) Δ8/4 vs $^{206}Pb/^{204}Pb$. Δ7/4 and Δ8/4 are the deviations from the NHRL [northern hemisphere reference line (Hart, 1984)] of $^{207}Pb/^{204}Pb$ and $^{208}Pb/^{204}Pb$, respectively. OV are dominated by mixing trend E–T: Escabecada (111743)–Tarrafal (111832), Stage 1. This mixing grades (black arrow) from E–T via the groups COVA and BOR into AN, which is dominated by mixing trend C–T: Codornitz (109901)–Tubarão(111767), Stage 2. The dominant source composition changed again (black arrow) through Stage 3, defined by the Cadela end-member (114521), to Stage 4, defined by the Coroa end-member (110026), which is dominant in the COROA, PRC and LAGOA groups. The mixing trend in (a) is shown dotted because the hyperbolic curvature is tentative (see text). Direction to the end-member for the São Vicente carbonatite end-member is marked 'carb'. Symbols as in Fig. 9.

reflected in the melts themselves: μ_{magmas} = 18–71, median 35) compared with N-MORB (6–10; Thirlwall, 1997), and with time this resulted in the observed high $^{206}Pb/^{204}Pb$ ratios of 19·1–19·9. The deviation of the Pb isotope composition of the Santo Antão volcanic rocks from the Northern Hemisphere Reference Line (NHRL; Hart, 1984), expressed as Δ8/4 and Δ7/4 (Figs 9 and 16), may be an indication of the age of source fractionation of U/Pb and U/Th.

Much of the range of Sr–Nd–Pb isotopic variation within the old and intermediage age Santo Antão rocks appears to be confined between two end-member compositions which we term Escabecada and Tarrafal (Table 5). The OV constitute a distinct group that trends between these end-members (Figs 9d and 16); we refer to this as Stage 1 in the evolution at Santo Antão. The Escabecada end-member is represented by 111743/OV (Figs 9d and 16) with radiogenic Sr and Pb, unradiogenic Nd and large negative Δ7/4 and Δ8/4 around zero. The Tarrafal end-member has less radiogenic Sr and Pb and more radiogenic Nd, and may be represented by the relatively young sample 111832/CAD from the top of the Tarrafal profile (Fig. 2). Within the lower Escabecada profile of the OV (Fig. 2), the older rocks tend to have more radiogenic Sr and Pb and unradiogenic Nd than the younger (Fig. 17). Age determinations from this part of the profile—top: 3·04 ± 0·17 (2σ) Ma and bottom: 2·74 ± 0·08 Ma (Plesner *et al.*, 2002; Holm *et al.*, unpublished)—indicate that the eruption period for the 40 lava flows in the profile was relatively short

Table 5: Geochemical and isotopic compositions of the major temporal rock groups and end-members

Major groups	Typical values						End-member compositions							
	Melting (%)	Si_{12} (wt %)	P_{12} (wt %)	Nb_{12} (ppm)	La/Nb	Sr/Nb	End-members	Stage no.	$^{87}Sr/^{86}Sr$	$^{143}Nd/^{144}Nd$	$^{206}Pb/^{204}Pb$	$^{208}Pb/^{204}Pb$	Δ7/4	Δ8/4
OV	1–2	43–46	0·3–0·5	40–70	0·6–0·8	9–12	Escabecada 111743/OV	1	0·70333	0·51288	19·88	39·65	−5	−2
							Tarrafal 111832/CAD	1	0·70316	0·51291	19·17	38·8	−2	+1
COVA	2–3	40–43	0·4–0·8	80–125	0·7–0·8	12–15	Tubarão 111767/COVA	2	0·7030	0·51297	19·39	39·0	−1	−7
AN	3–4	42–43	0·7 0·9	60–80	0·8–0·9	12–14	Codornitz 109901/BOR	2	0·7030	0·51294	19·93	39·3	−5	−38
CAD	2–4	38–40	0·8–1·8	80–125	0·8–1·1	11–14	Cadela 114521/CAD	3	0·7031	0·51290	19·77	39·4	−1	−9
COROA	4–5	38–39	0·8–1·2	90–100	0·8–0·9	10–12	Coroa 110026/COROA	4	0·7031	0·51292	19·63	39·5	+3	−7
LAGOA	3–4	39–40	0·9–1·1	100–110	0·7–0·8	10–12								

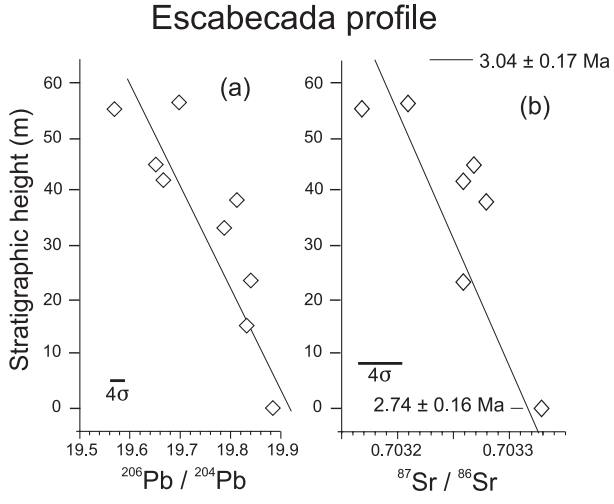

Fig. 17. Temporal evolution of a sequence of lavas within OV: Stratigraphic height (m) vs (a) $^{206}Pb/^{204}Pb$ and (b) $^{87}Sr/^{86}Sr$ for representative samples of the lower Escabecada profile (Fig. 2), which has a thickness of 60 m and consists of 40 lavas. The bottom lava is the Escabecada end-member (111743). Age data are from Plesner *et al.* (2002) and our unpublished data.

(statistically only $\leq$30 kyr). The rocks are not comagmatic but show a clear change over time from the Escabecada end-member isotopic composition towards the Tarrafal end-member composition. The considerable variation over a short time interval in the Escabecada profile indicates that both end-members contributed to the magmas at essentially the same time. The curvature of a mixing hyperbola in Fig. 16a and b is a function of the Sr/Pb ratios of the end-members and is a straight line if Sr/Pb ratios of the end-members are the same. We have connected the end-members with straight lines (mixing line Escabecada–Tarrafal (E–T) in Fig. 16) for simplicity and because Sr/Pb ratios of the end-members are not expected to be very different, judging from the end-member melt compositions, $Sr/Pb_{111743} = 292$ and $Sr/Pb_{111832} = 362$ (Table 1). However, small degrees of melting and possible exotic residual phases in the mantle make inferred source Sr/Pb uncertain.

Although a change in isotopic composition after Stage 1 is clear from Fig. 9a and d–f, the transition is better illustrated by a series of diagrams with the variables Δ7/4 and Δ8/4 (Fig. 16). Over time, the Santo Antão magmas appear to have been derived progressively from more trace element-enriched sources with less radiogenic Sr and more radiogenic Nd and increasingly negative Δ8/4, whereas Δ7/4 increased somewhat (Fig. 16). The COVA group (1·4–0·7 Ma) illustrates this and constitutes an intermediate evolutionary stage. Stage 2 was reached at the end of the change portrayed by the COVA group. Stage 2 is distinctly defined by the the Codornitz–Tubarão two-component mixing (Fig. 9d; C–T mixing line in Fig. 16), which includes the compositionally distinct western AN volcanic rocks (0·5–0·3 Ma) with large negative Δ8/4 (Fig. 16d). The end-members of this trend are extreme compositions for Santo Antão and are developed at Tubarão (111767/COVA) with very unradiogenic Sr, together with radiogenic Nd and the HIMU-type high $^{206}Pb/^{204}Pb$ of Codornitz (109901/BOR) with $\Delta 8/4 = -38$ (Figs 9d and 16). The Codornitz sample has

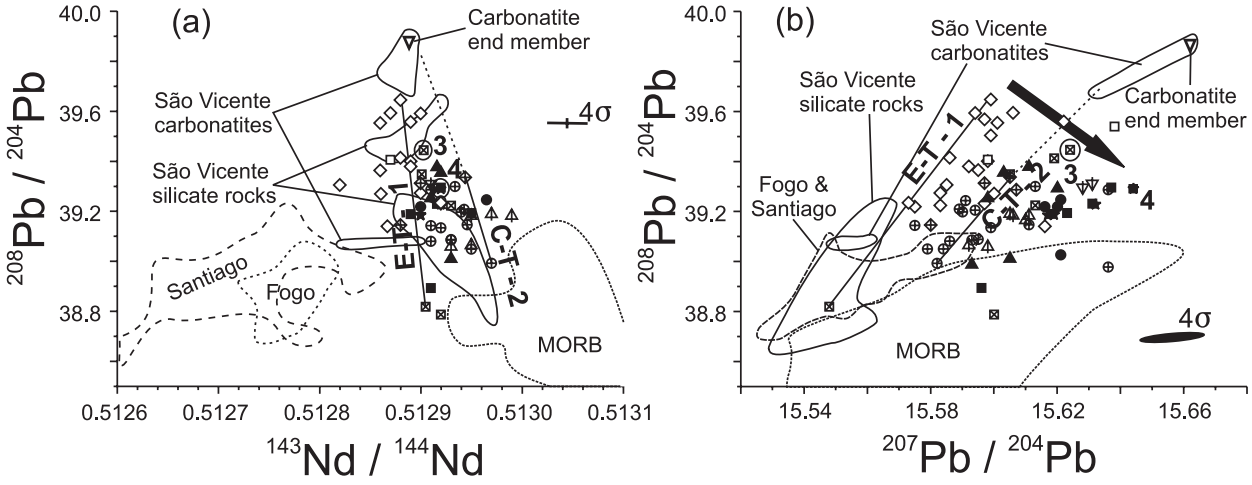

Fig. 18. Comparison of the isotopic composition of Santo Antão volcanic rocks. Also shown are Stages 1–4, the compositions of MORB and samples from other Cape Verde islands including the carbonatites of the neighbouring São Vicente together with Santiago and Fogo from the southern part of the archipelago. (a) $^{208}Pb/^{204}Pb$ vs $^{143}Nd/^{144}$ Nd; (b) $^{208}Pb/^{204}Pb$ vs $^{207}Pb/^{204}Pb$. Lines 'E–T' (Stage 1) and 'C–T' (Stage 2) connect the end-members in (a) and are mixing lines in (b); Stages 1–4 are defined in Fig. 16 and the text. Arrow in (b) shows the general evolution on Santo Antão as defined in Fig. 16. The extensions of trend 'C–T' (dashed line) coincide with the end-member for São Vicente carbonatites. Data sources and symbols as in Fig. 10.

an age of ~1·2 Ma and represents the earliest and strongest imprint of this HIMU type of radiogenic Pb. The AN group constitutes the end of an evolution starting from OV that seems to represent the exchange of one set of end-members for another, as shown by the black arrow from Stage 1 to Stage 2 in Fig. 16. The CAD, FRA and YTAR groups (0·7–0·2 Ma) mark the appearance of a new component with a clear trend towards less negative Δ7/4 (Stage 3 in Fig. 16). The earliest CAD lavas are interpreted as the products of very small degrees of melting (down to 2%) and have the highest incompatible element enrichment on the island, with up to 125 ppm Nb_{12} and 1·8% P_{12} (Figs 11 and 13–15). We term this the Cadela end-member. AN and FRA melts were derived by a larger degree of melting than most other Santo Antão magmas (Fig. 15) and have higher Sr_{12}/Nb_{12}, La_{12}/Nb_{12}, Sr_{12}/Nd_{12}, Rb_{12}/Nb_{12} and Ba_{12}/Nb_{12} ratios than OV (Fig. 14).

The most recent development of the isotopic composition of the Santo Antão magmas is an extension of the trend from AN to CAD towards higher Δ7/4 (Stage 4 in Fig. 16). The PRC, COROA and LAGOA group rocks (0·3–0·1 Ma) are characterized by positive Δ7/4 and intermediate Sr, Nd and $^{206}Pb/^{204}Pb$ ratios and trend toward the Coroa end-member. The young nephelinites and melilite nephelinites (Si_{12} = 38–41·5, Fe_{12} = 12–14·5) of the Coroa and Lagoa area (Fig. 2) were derived by varying degrees of melting of highly enriched sources (Figs 11 and 13–15) but did not reach the extreme incompatible element enrichment of some CADs. Distinct Sr_{12}/Nb_{12}, Sr_{12}/Nd_{12} and La_{12}/Nb_{12} in LAGOA, COROA and PRC indicate different source compositions for these contemporaneous groups.

Implications in relation to mantle end-member components

The OV is characterized by higher $^{87}Sr/^{86}Sr$ than the (old) HIMU mantle end-member component (e.g. St Helena; Zindler & Hart, 1986) and for the Escabecada end-member (111743), both Pb and Sr isotopes indicate that it cannot have been derived by recent mixing of MORB and HIMU mantle (Fig. 9). A young HIMU-type source (Thirlwall, 1997) is required to explain the large negative Δ7/4 (down to −5) of the OV (Fig. 16c) and could be achieved by a change in μ from 10 to 20 in a MORB source 1·3 Gyr ago. The relationship between thorogenic Pb and radiogenic Sr and unradiogenic Nd for the Escabecada end-member (Figs 9 and 16) is evidence against the presence of an EM1 component. In the southern Cape Verde islands, an important part of the EM1 character is the relatively unradiogenic Pb (Fig. 9) and it is clear from the variation among the OV (Stage 1 in Figs 9 and 16) that any EM1 contribution in these rocks is insignificant. Unlike EM2, which is thought to be derived from old continental crust, the OV has relatively low La_{12}/Nb_{12} and Rb_{12}/Nb_{12}, which indicates that contribution from any EM2 source was minor. The radiogenic Sr and unradiogenic Nd of the OV could imply contribution from a HIMU source, perhaps as a minor clastic sediment component in the subducted oceanic crust, as suggested by Thirlwall (1997), and giving this end-member a flavour of EM2.

The Tarrafal end-member, with its radiogenic Sr and unradiogenic Pb and Nd, could be a mixture between MORB mantle and EM (I or II), and thus be the only end-member at Santo Antão with a possible relationship to the southern Cape Verde Islands, but its relative position in Fig. 18a indicates that any EM component is minor, because, in this diagram, sample 111832 is the most MORB-like of any Santo Antão rocks.

The radiogenic Pb in the Codornitz end-member requires a lowering in the past of Th/U relative to sources with present-day $\Delta 8/4 = 0$, such as that of the OV. A model calculation shows that if μ was increased from 10 to 20 at 1·3 Ga, the development of a $\Delta 8/4$ value of -40 requires simultaneous lowering of the Th/U ratio from 4·0 to 3·65. It is also noteworthy that the general evolution with time since the eruption of the OV is towards lower $^{87}Sr/^{86}Sr$ and is accompanied by higher $^{143}Nd/^{144}Nd$. It is not, therefore, a trend towards St Helena HIMU-like compositions (Fig. 9). Isotopically, the carbonatites of nearby São Vicente trend towards an end-member composition with very radiogenic Pb ($^{206}Pb/^{204}Pb > 20{\cdot}65$; Fig. 9b) with both very negative $\Delta 7/4 = -7$ and $\Delta 8/4 = -70$ (Jørgensen & Holm, in preparation). The Codornitz end-member for Stage 2 lies on this trend (Fig. 16d). The extension of the C–T mixing curve for Stage 2 for Pb, Sr and Nd includes the carbonatite end-member composition for São Vicente (Figs 16 and 18; Jørgensen & Holm, in preparation). Important contributions from the carbonatite source for Santo Antão volcanic rocks were thus restricted to intermediate times (1·4–0·3 Ma). The strong influence of the carbonatite end-member on the isotopic composition, in particular Pb, is not accompanied by clear elemental evidence, as was concluded earlier for all Santo Antão samples. More specifically, Cape Verde carbonatites have low Zr/Nb (<1) and high Nb/Ta (67, median), whereas the Codornitz end-member samples have high Zr/Nb (4·0–4·8) and chondritic Nb/Ta, except for 109997/BOR with Nb/Ta = 23. We therefore suggest that the Codornitz-type melts were generated from mantle metasomatized by the same carbon-rich material that in some cases formed the carbonatite source, but in this case was part of a lherzolitic mantle that yielded strongly silica-undersaturated melt at high P_{CO_2}.

The Tubarão end-member of the C–T mixing has relatively unradiogenic Sr, Pb and radiogenic Nd and has $\Delta 7/4$ and $\Delta 8/4$ close to zero. The Tubarão end-member may, therefore, have a significant component of recycled depleted oceanic crust. However, assuming a model age of 1·3 Ga (as indicated by Pb isotopes), the rather low $^{143}Nd/^{144}Nd$ can be modelled only if Sm/Nd_{MORB} was as low as 0·15, requiring this depleted component at some stage to have been a partial melt of garnet peridotite in order to significantly decrease its original high MORB-like Sm/Nd-ratio. In one scenario, the Tubarão source could have been generated if DM-derived melts metasomatized the base of thick lithosphere which was subsequently delaminated and sank into the asthenosphere to be included in the Cape Verde mantle plume.

Isotopically, the Cadela end-member of Stage 3, such as the extremely incompatible element-enriched 114522/CAD (Tables 1 and 3), is intermediate between the Codornitz and Coroa end-members (Fig. 16).

The most recent development of the isotopic composition of Santo Antão magmas is an enhancement of the trend from AN to CAD. The PRC, COROA and LAGOA group rocks of Stage 4 are characterized by positive $\Delta 7/4$ and intermediate Sr, Nd and $^{206}Pb/^{204}Pb$ ratios. Positive $\Delta 7/4$ requires an increase >2 Gyr ago of μ in the source, i.e. an old HIMU source. The data may suggest that the old HIMU component in the Coroa end-member was the main contributor to the change in source enrichment in general for Santo Antão volcanic rocks in AN times because the increase in $\Delta 7/4$ from -5 to $+2$ (Fig. 16c) broadly correlates with enrichment as modelled by Zr and Nb (Fig. 15). However, the more complex variation with time demonstrated by, for example, La/Nb and Sr/Nb (arrows in Fig. 14b) probably indicates that the volcanic rocks record a changing interaction between, or contribution from, more than two source components.

The Coroa end-member could not have been generated by mixing with any of the other Santo Antão end-members (Fig. 16). It requires an ancient (>2 Gyr) increase of U/Pb. Modern Central Atlantic N-MORB with reported positive $\Delta 7/4$ is not uncommon (Dosso *et al.*, 1993) but it has much lower $^{206}Pb/^{204}Pb$. The positive $\Delta 7/4$ in the Coroa end-member may reflect a source influenced by subduction of either old continental sediments or oceanic crust >2 Gyr ago.

The Coroa end-member composition was definitely not important in the early Santo Antão melts. It is highly unlikely that Coroa melts were mobilized from the lithosphere only at a late stage of the evolution after magmas had passed through for a time-span of more than 7 Myr. We, therefore, consider it likely that the Coroa end-member isotopically was the third part of the mantle plume to yield melts below Santo Antão.

The contrast between north and south Cape Verde Islands

The differences between the HIMU components in the mantle sources of the southern Cape Verde islands and Santo Antão, and the lack of an EM1 component in the source for both Santo Antão and São Vicente volcanic rocks (discussion above; Jørgensen & Holm, 2002), show that grossly different mantle components were involved in the formation of the northern and southern Cape

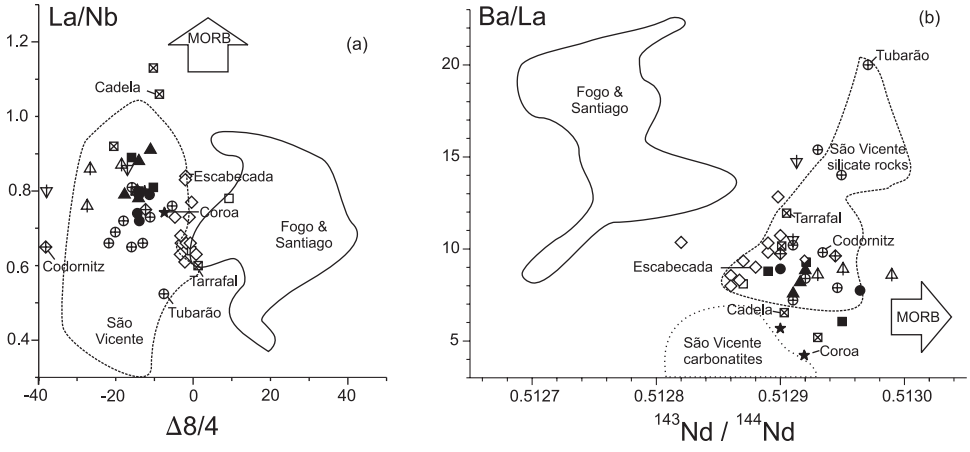

Fig. 19. (a) La_{12}/Nb_{12} vs Δ8/4 and (b) Ba_{12}/La_{12} vs $^{143}Nd/^{144}Nd$ in samples from Santo Antão, São Vicente, Santiago and Fogo. The end-member samples are marked. Data sources and symbols as in Fig. 10.

Verde Islands. This is emphasized in Fig. 19. Although the range of La/Nb ratios is similar in the two parts of the archipelago, they have very different Δ8/4 and trends among the Santo Antão rocks are not directed towards the compositions of the southern islands (Fig. 19a). We plot measured trace element ratios in order to obtain all isotope data presented in the diagram. This is not a problem because Ba, Nb and La are all very incompatible in the MgO range of these samples. The relationships between Ba/La and $^{143}Nd/^{144}Nd$ display the same pattern (Fig. 19b). The end-members involved in this seem unrelated to the main EM1-type source component with high Ba/La and low $^{143}Nd/^{144}Nd$ for the southern Cape Verde islands. This leads us to suggest that the plume stem is zoned in a similar way (cross-sectional) to that proposed for the Galapagos plume by Hoernle *et al.* (2000), and could involve two adjacent plume stems. Alternatively, the EM1 component could represent old continent-derived material included in the oceanic lithosphere, as suggested by Kokfelt *et al.* (1998).

Indications for the origin of the source components

Low to moderate $^{3}He/^{4}He$ ratios were found in samples of the southern island of Fogo and in Santo Antão, and suggest that a HIMU component was part of the source of both the southern and northern islands and that it originated in the lower mantle (Christensen *et al.*, 2001). The absence of high $^{3}He/^{4}He$ ratios (Christensen *et al.*, 2001) indicates that the proposed mantle components C (Hanan & Graham, 1996) and FOZO (Hart *et al.*, 1992) are not important in Santo Antão rocks, although their Sr–Nd–Pb isotopic compositions are indistinguishable (Fig. 9a and b).

Low La/Nb is characteristic of HIMU OIB (e.g. Weaver, 1991; Vidal, 1992) and has been suggested

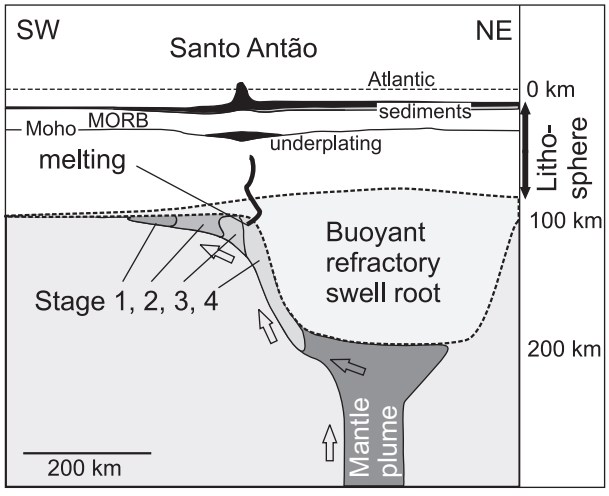

Fig. 20. Model for the successive generation of melts from significantly different sources: Stage 1: Escabecada and Tarrafal end-members; Stage 2: Codornitz and Tubarão end-members; Stage 3: Cadela end-member; Stage 4: Coroa end-member. The plume is thought to be (i) inhomogeneous in cross-section, which is responsible for compositional variation between the islands of the Cape Verdes, and (ii) have a changing composition of the rising material, which explains the time-related variation on Santo Antão. In this model, the Cape Verde Rise is centered over the plume stem. The swell root grows to the depths of devolatilization of the plume material and develops laterally with melt extraction. See text for discussion.

to be a feature of subducted oceanic crust incorporated in mantle plumes (e.g. Hofmann, 1997). As part of the Cape Verde plume, we invoke a young (≈1·3 Gyr) HIMU source with a component of continentally derived sediments in order to explain the high $^{87}Sr/^{86}Sr$ in the OV. Because of the moderate μ of the melts, the radiogenic Pb could not have developed in the relatively young (∼0·12 Gyr) oceanic lithosphere, whether it be N-MORB or plume-derived with an EM1-type isotopic composition as found by Janney & Castillo (2001).We have already mentioned that the most obvious candidate for a

lithospheric source—the Coroa end-member composition—was probably derived from the Cape Verde plume. Therefore, and in accordance with Gerlach *et al.* (1988), Davies *et al.* (1989), Christensen *et al.* (2001) and Jørgensen & Holm (2002), we ascribe the HIMU materials to the plume. There is no indication of lithospheric or old continental EM1 or EM2 material in the Santo Antão melts, except maybe as a minor component of the Tarrafal end-member.

A model

The Cape Verde Rise is thought to be a hotspot swell and has been proposed to be of thermal origin (Crough, 1978) or to have an additional component of buoyancy from the rising plume (Sleep, 1990). Phipps Morgan *et al.* (1995) proposed that the effect of formation of a swell root of buoyant residue after melt extraction is also important. Compared with the unmelted plume material, the swell root will be more viscous because of devolatilization (Hirth & Kohlstedt, 1996). With a stationary lithosphere, we propose that the rising plume material is deflected by the swell root and that it only crosses its solidus at the edge of the swell. This could explain the position of the Cape Verde Islands towards the edge of the Cape Verde Rise (Fig. 1). In such a scenario (Fig. 20), the volcanism on one island will be caused by melts derived from plume material moving in an inclined fashion under the lithosphere-swell root and laterally away from the centre of the plume stem. We therefore propose that the changing source compositions, as defined by the elemental and isotopic composition of the Santo Antão magmas, reflect a sequence of source domains originally rising in a layered plume. The thickness of the 120 Ma Santo Antão lithosphere is expected to be 100–125 km (Parsons & McKenzie, 1978). The depth of melting in the plume will depend on the thickness of the lithospheric lid; this may either have decreased by erosion from the hot plume material over probably 20 Myr, or may have increased by the growth of a swell root. The depth of melt extraction, estimated as 90–120 km from geochemical arguments, is probably realistic.

The existence of such complex zonation in the plume, comprising both the north–south division and the layering for the northern part, would (1) require that little interaction took place between the different components of the rising plume or between these and the ambient mantle, as confirmed by the insignificance of the DM component in Santo Antão rocks, and (2) reflect heterogeneity in the sublithospheric mantle. We have not modelled the velocity of the deflected plume material that would be required to constrain the scale of the source inhomogeneity indicated by Santo Antão magmas.

The Stage 1 volcanism on Santo Antão (OV) and the early volcanism on the neighbouring island of São Vicente (Jørgensen & Holm, 2002) show considerable compositional overlap. However, the later trends diverge as the São Vicente carbonatites were emplaced in the crust after eruption of the Old Volcanic rocks where they contaminated subsequent magmas of the Intermediate Volcanic rocks on their way to the surface. Intermediate age volcanic rocks on São Vicente have very high Sr/Nd (18–25) and P/Zr up to 4 × PM (Jørgensen & Holm, 2002). These have no counterparts on Santo Antão, in accordance with the absence of carbonatites there. The Coroa type enrichment with positive Δ7/4 (Stage 4) is not present on São Vicente. A major part of the difference between the two islands may be explained if plume material first yielded carbonatite magmas and subsequently, when the carbonatite-depleted source passed under Santo Antão, yielded the intermediate age volcanic rocks that have the same isotopic trend as the São Vicente carbonatites. Alternatively, additional source inhomogeneity is indicated.

SUMMARY OF CONCLUSIONS

Magma compositions on Santo Antão from 7·5 to 0·1 Ma changed from an early basanite–phonolite series to a more incompatible element-enriched (melilite) nephelinite–phonolite series. Crustal contamination of the magmas was insignificant. Primary, mantle-derived melts are inferred to have around 12% MgO and olivine $Fo_{88–91}$ is present in many primitive rocks on Santo Antão. The samples have HIMU OIB-like incompatible element patterns with a primary fourfold range of variation in the degree of enrichment of the mantle incompatible trace elements Rb, Ba, Th, K, Nb, La and P (e.g. La: 50–200 × PM). According to modelling and comparison with experimental results, the melts were extracted at depths of around 90 km at the transition between garnet- and spinel-lherzolite mantle facies by 1–4% partial melting.

Modelling of incompatible element abundances in the most primitive magmas shows that variable degrees of melting are only part of the cause of the geochemical variation. Important differences between the magmas must be related to mantle source variation over time. From the eruption of the old volcanic rocks (OV group, 7·5–2 Ma) during Stage 1 through intermediate age (2–0·3 Ma) groups COVA, BOR to AN at Stage 2, the melts were derived from more enriched sources with higher Sr/Nb, La/Nb and Zr/Nb, and the melts tend to have been generated by slightly higher degrees of melting. The late intermediate age group CAD (0·7–0·3 Ma) of very silica-undersaturated melts were derived by lower degrees of melting of a source additionally enriched, possibly by melts with MORB features such as high La/Nb (to 1·15) and Zr/Nb, Stage 3. The young volcanic rocks (<0·3 Ma) at Stage 4 are also strongly silica-undersaturated but are derived by slightly larger

degrees of melting than CAD melts and show a decrease in La/Nb but similar source enrichment. The strong negative K anomaly in the most primitive magma compositions seems related to residual phlogopite in the source. High Ce/Pb in the volcanic rocks probably rules out significant contributions to the sources from continent-derived materials, as also indicated by the isotopic compositions.

Isotopically, the OV group is explained by two-component mixing of components with relatively radiogenic Sr and unradiogenic Nd (Stage 1). The Escabecada end-member with the most radiogenic Pb of Santo Antão is a typical young HIMU source ($\Delta 8/4 \approx 0$ and $\Delta 7/4 \approx -5$) with a model age of 1·3 Ga.

Gradual changes in subsequent COVA, and in particular AN, melts display the shift to mixing between two other components: Tubarão and Codornitz (Stage 2). The latter is also a young HIMU source of 1·3 Ga model age, but with $\Delta 7/4 \approx -5$ and $\Delta 8/4 \approx -38$ and less radiogenic Sr and more radiogenic Nd. This mixing trend is identical to that of many Cape Verde carbonatites. Major and trace elements, on the other hand, do not show a carbonatitic influence on these melts (e.g. their high FeO, TiO_2 and Zr/Nb), and the Codornitz end-member source could be residual after earlier extraction of carbonatite. The Tubarão end-member may be derived from mantle metasomatized by melts derived from garnet-bearing depleted mantle (DM).

The latest magmas on Santo Antão (Stage 3 and 4) are related to an old HIMU-type ($\Delta 7/4 > 0$) source of moderate μ, the Coroa end-member. The CAD source is intermediate between Coroa and Codornitz and must have approximately the same old HIMU isotopic composition as Coroa. The location of this end-member above the NHRL indicates that the enrichment took place >2 Gyr ago.

We find it most likely that all three HIMU end-members were derived from the mantle plume, and suggest that the two relatively depleted end-members were also plume derived. Santo Antão volcanic rocks show no indication of the EM1-type source prominent in southern Cape Verde islands (Gerlach *et al.*, 1988). The petrogenesis of the Santo Antão magmas seems to indicate that early partial melting involved a mantle source of mainly two components (Stage 1), followed by melts from a different source which also involved two components (Stage 2). This second source was eventually replaced by a third (Cadela, Stage 3) which is either part of a two-component source, or preceded a fourth source (Coroa, Stage 4). Because the lithosphere is virtually stationary, it is inferred from this progression that a sequence of mantle materials yielded melts below Santo Antão. We explain this by the rise of a mantle plume which was inhomogeneous and layered along the stem. Strong inter-island variation at the Cape Verdes is thought to reflect a lateral component of zonation in the plume.

ACKNOWLEDGEMENTS

We are grateful for comments on various drafts of the manuscript from Helene Duprat, Rikke Sølling, Tanja Grandvuinet, Lise Pedersen, Jesper Jørgensen and Mads Faurschou Knudsen. Laboratory assistance from Maria Jankowsky, Birthe Møller, Tobi Lehrer, Berit Wenzell and Robert Frei is greatly appreciated. Thorough and constructive reviews by Karen Harpp, Catherine Chauvel, Anton le Roex and Marjorie Wilson contributed significantly to the final outcome. John Bailey, Raymond Gwozdz and Jørgen Kystol competently provided the major and trace element analyses. José Cardoso of the Danish relief organization 'Børnefonden', which keeps all children on Santo Antão in school, kindly gave logistic support. The Danish Natural Science Research Council financed the TIMS analytical facility and enabled us to do field work in the Cape Verde Islands (Grant nos 980197 and 21-01-0495).

SUPPLEMENTARY DATA

Supplementary data for this paper are available at *Journal of Petrology* online.

REFERENCES

Abouchami, W., Galer, S. J. G. & Hofmann, A. W. (2000). High precision lead isotope systematics of lavas from the Hawaiian Scientific Drilling Project. *Chemical Geology* **169**, 187–209.

Ali, M. Y., Watts, A. B. & Hill, I. (2003). A seismic reflection profile study of lithospheric flexure in the vicinity of the Cape Verde Rise. *Journal of Geophysical Research* **108**, 2239–2264.

Barnes, S. J. & Roeder, P. L. (2001). The range of spinel compositions in terrestrial mafic and ultramafic rocks. *Journal of Petrology* **42**, 2279–2302.

Bebiano, J. B. (1932). A geologia do arquipelago de Cabo Verde. *Communicacion Servicio de Geológia de Portugal* **18**, 226 pp.

Blundy, J. D., Robinson, J. A. C. & Wood, B. J. (1998). Heavy REE are compatible in clinopyroxene on spinel lherzolite solidus. *Earth and Planetary Science Letters* **160**, 493–504.

Chaffey, D. J., Cliff, R. A. & Wilson, B. M. (1989). Characterization of the St Helena magma source. In: Saunders, A. D. & Norry, M. J. (eds) *Magmatism in the Ocean Basins. Geological Society, London, Special Publications* **42**, 257–276.

Chauvel, C. & Hemond, C. (2000). Melting of a complete section of recycled oceanic crust: trace element and Pb isotopic evidence from Iceland. *Geochemistry, Geophysics, Geosystems* **1**, Paper 1999GC000002.

Chauvel, C., McDonough, W., Guille, G., Maury, R. & Duncan, R. (1997). Contrasting old and young volcanism in Rurutu island, Austral chain. *Chemical Geology* **139**, 125–143.

Christensen, B. P., Holm, P. M., Jambon, A. & Wilson, R. J. (2001). Helium, argon and lead isotopic composition of volcanics from Santo Antão and Fogo, Cape Verde Islands. *Chemical Geology* **178**, 127–142.

Class, C. & Goldstein, S. L. (1997). Plume–lithosphere interactions in the ocean basins: constraints from the source mineralogy. *Earth and Planetary Science Letters* **150**, 245–260.

Crough, S. T. (1978). Thermal origin of mid-plate hot-spot swells. *Geophysical Journal of the Royal Astronomical Society* **55**, 451–469.

Dash, B. P., Ball, M. M., Kings, G. A., Butler, L. W. & Rona, P. A. (1976). Geophysical investigation of the Cape Verde archipelago. *Journal of Geophysical Research* **81**, 5249–5259.

Davies, G. F., Norry, M. J., Gerlach, D. C. & Cliff, R. A. (1989). A combined chemical and Pb–Sr–Nd isotope study of the Azores and Cape Verde hot-spots: the geodynamic implications. In: Saunders, A. D. & Norry, M. J. (eds) *Magmatism in the Ocean Basins. Geological Society, London, Special Publications* **42**, 231–255.

De Paepe, P., Klerkx, J., Hertogen, J. & Plinke, P. (1974). Oceanic tholeiites on the Cape Verde Islands: petrochemical and geochemical evidence. *Earth and Planetary Science Letters* **22**, 347–354.

DePaolo, D., Bryce, J. G., Dodson, A., Shuster, D. L. & Kennedy, B. M. (2001). Isotopic evolution of Mauna Loa and the chemical structure of the Hawaiian plume. *Geochemistry, Geophysics, Geosystems* **2**, Paper 2000GC000139.

Dosso, L., Bougault, H. & Joron, J.-L. (1993). Geochemical morphology of the north Mid-Atlantic ridge, 10–24°N: trace element–isotopic complementarity. *Earth and Planet Science Letters* **120**, 443–462.

Duncan, R. A. & Jackson, E. D. (1977). Geochronology of basaltic rocks recovered by DSDP Leg 41, Eastern Atlantic Ocean. In: Lancelot, Y., Seibold, E., *et al.* (eds) *Initial Report of the Deep Sea Drilling Project*, **41**, Washington, DC: US Government Printing Office, pp. 1113–1118.

Eggler, D. H. (1989). Carbonatites, primary melts, and mantle dynamics. In Bell, K. (ed.) *Carbonatites: Genesis and Evolution*. London: Unwin Hyman, pp. 561–579.

Fitton, J. G., Saunders, A. D., Norry, M. J., Hardarson, B. S. & Taylor, R. N. (1997) Thermal and chemical structure of the Iceland plume. *Earth and Planetary Science Letters* **153**, 197–208.

Gerlach, D. C., Cliff, R. A., Davies, G. R., Norry, M. J. & Hodgson, N. (1988). Magma sources of the Cape Verdes archipelago: isotopic and trace element constraints. *Geochiemica et Cosmochimica Acta* **52**, 2979–2992.

Govindaraju, K. (1994) 1994 compilation of working values and sample descriptions for 383 geostandards. *Geostandards Newsletter* **18**, special issue, 158 pp.

Grove, T. L. & Bryan, W. B. (1983). Fractionation of pyroxene-phyric MORB at low pressure: an experimental study. *Contributions to Mineralogy and Petrology* **84**, 293–309.

Halliday, A. N., Lee, D.-C., Tommasini, S., Davies, G. R., Paslick, C. R., Fitton, J. G. & James, D. E. (1995). Incompatible trace elements in OIB and MORB and source enrichment in the sub-oceanic mantle. *Earth and Planetary Science Letters* **133**, 379–395.

Hanan, B. B. & Graham, D. W. (1996). Lead and helium isotope evidence from oceanic basalts for a common deep source of mantle plumes. *Science* **272**, 991–995.

Hards, V. L., Kempton, P. D. & Thompson, R. N. (1995). The heterogeneous Iceland plume: new insights from the alkaline basalts of the Snaefell volcanic centre. *Journal of the Geological Society, London* **152**, 1003–1009.

Harland, W. B., Armstrong, A. V., Cox, L. E. & Craig, A. (1990) *Geologic Time Scale 1989*. New York: Cambridge University Press.

Hart, S. R. (1984). A large-scale isotopic anomaly in the Southern Hemisphere mantle. *Nature* **309**, 753–757.

Hart, S. R. & Dunn, T. (1993). Experimental cpx/melt partitioning of 24 trace elements. *Contributions to Mineralogy and Petrology* **113**, 1–8.

Hart, S. R., Hauri, E. H., Oschmann, L. A. & Whitehead, J. A. (1992). Mantle plumes and entrainment: isotopic evidence. *Science* **256**, 517–520.

Hauri, E. H., Lassiter, J. C. & DePaolo, D. J. (1996) Osmium isotope systematics of drilled lavas from Mauna Loa, Hawaii. *Journal of Geophysical Research* **101**, 11793–11806.

Hayes, D. E. & Rabinowitz, P. D. (1975). Mesozoic magnetic lineations and the magnetic quiet zone off Northwest Africa. *Earth and Planetary Science Letters* **28**, 105–115.

Hess, P. C. (1992) Phase equilibria constraints on the origin of ocean floor basalts. In Morgen, J. P., Blackmun, D. K. & Sinton, J. M. (eds) *Mantle Flow and Melt Generation at Mid-Ocean Ridges. American Geophysical Union, Geophysical Monograph* **71**, 67–102.

Hirose, K. (1997). Partial melt compositions of carbonated peridotite at 3 GPa and the role of CO_2 in alkali–basalt magma generation. *Geophysical Research Letters* **24**, 2837–2840.

Hirose, K. & Kushiro, I. (1993). Partial melting of dry peridotites at high pressures: determination of compositions of melts segregated from peridotite using aggregates of diamond. *Earth and Planetary Science Letters* **114**, 477–489.

Hirth, G. & Kohlstedt, D. L. (1996). Water in the oceanic mantle: implications for rheology, melt extraction and the evolution of the lithosphere. *Earth and Planetary Science Letters* **144**, 93–108.

Hoernle, K., Tilton, G. & Schmincke, H.-U. (1991). Sr–Nd–Pb isotopic evolution of Gran Canaria: evidence for shallow enriched mantle beneath the Canary Islands. *Earth and Planetary Science Letters* **106**, 44–63.

Hoernle, K., Tilton, G., LeBas, M. J., Duggen, S. & Garbe-Schonberg, D. (2001). Geochemistry of oceanic carbonatites compared with continental carbonatites: mantle recycling of oceanic carbonatites. *Contributions to Mineralogy and Petrology* **142**, 520–542.

Hoernle, K., Werner R., Phipps Morgan, J., Garbe-Schönberg, D., Bryce, J. & Mrazek, J. (2000) Existence of complex spatial zonation in the Galápagos plume for at least 14 m.y. *Geology* **28**, 435–438.

Hofmann, A. W. (1997). Mantle geochemistry: the message from oceanic volcanism. *Nature* **385**, 219–229.

Holm, P. M., Hald, N. & Waagstein, R. (2000). Geochemical and Pb–Sr–Nd isotopic evidence for separated hot depleted and Iceland plume mantle sources for the Paleogene basalts of the Faroe Islands. *Chemical Geology* **178**, 95–125.

Irvine, T. N. (1967). Chromian spinel as a petrogenetic indicator. Part 2: Petrological applications. *Canadian Journal of Earth Sciences* **4**, 71–101.

Janney, P. E. & Castillo, P. R. (2001). Geochemistry of the oldes Atlantic oceanic crust suggests mantle plume involvement in the early history of the central Atlantic Ocean. *Earth and Planetary Science Letters* **79**, 291–302.

Jørgensen, J. Ø. (2003). A geochemical study of carbonatites from the Cape Verde Islands, basaltic rocks from São Vicente and fenites from Brava. (Ph.D. thesis), University of Copenhagen, 135 pp.

Jørgensen, J. Ø. & Holm, P. M. (2002). Temporal variation and carbonatite contamination in primitive ocean island volcanics from São Vicente, Cape Verde Islands. *Chemical Geology* **192**, 249–267.

Kempton, P. D., Fitton, J. G., Saunders, A. D., Nowell, G. M., Taylor, R. N., Hardarson, B. S. & Pearson, G. (2000). The Iceland plume in space and time: a Sr–Nd–Pb–Hf study of the North Atlantic rifted margin. *Earth and Planetary Science Letters* **177**, 255–271.

Klein, E. M. & Langmuir, C. H. (1987). Global corrections of ocean ridge basalts. 1: Experiments and methods. *Journal of Geophysical Research* **97**, 4241–4252.

Kokfelt, T. F., Holm, P. M., Hawkesworth, C. J. & Peate, D. W. (1998). A lithospheric mantle source for the Cape Verde Island magmatism:

trace element and isotopic evidence from the island of Fogo. *Mineralogical Magazine* **62A**, 801–802.

Kurz, M. D., Kenna, T. C., Lassiter, J. C. & DePaolo, D. J. (1995) Helium isotopic evolution of Mauna Kea Volcano: first results from the 1-km drill core. *Journal of Geophysical Research* **101**, 11781–11791.

Kystol, J. & Larsen, L. M. (1999). Analytical procedures in the rock geochemical laboratory of the Geological Survey of Denmark and Greenland. *Geology of Greenland Survey Bulletin* **184**, 59–62.

Langmuir, C. H., Klein, E. M. & Plank, T. (1992) Petrological systematics of mid-ocean ridge basalts. In: Morgen, J. P., Blackmun, D. K. & Sinton, J. M. (eds) *Mantle Flow and Melt Generation at Mid-Ocean Ridges. American Geophysical Union, Geophysical Monograph* **71**, 183–280.

Larsen, L. M. & Pedersen, A. K. (2000). Processes in high-Mg high-*T* magmas: evidence from olivine, chromite and glass in Palaeogene picrites from West Greenland. *Journal of Petrology* **41**, 1071–1098.

Lassiter, J. C., DePaolo, D. J. & Tatsumoto, M. (1996) Isotopic evolution of Mauna Kea Volcano: results from the initial phase of the Hawaii Scientific Drilling Project. *Journal of Geophysical Research* **101**, 11769–11780.

Le Bas, M. J. (2000). IUGS reclassification of high-Mg and picritic volcanic rocks. *Journal of Petrology* **41**, 1467–1470.

Le Maitre, R. W. (1989). *A Classification of Igneous Rocks and Glossary of Terms*. Oxford: Blackwell Scientific Publications, 193 pp.

Le Roex, A. P., Cliff, R. A. & Adair, J. I. (1990). Tristan da Cunha, South Atlantic: geochemistry and petrogenesis of a basanite–phonolite lava series. *Journal of Petrology* **31**, 779–812.

McKenzie, D. & Bickle, M. J. (1988). The volume and composition of melt generated by extension of the lithosphere. *Journal of Petrology* **29**, 625–679.

McKenzie, D. & O'Nions, R. K. (1995) The source region of ocean island basalts. *Journal of Petrology* **36**, 133–159.

McNutt, M. (1988). Thermal and mechanical properties of the Cape Verde Rise. *Journal of Geophysical Research* **91**, 13915–13923.

Mitchell, J. G., Le Bas, M. J., Zielonka, J. & Furnes, H. (1983). On the magmatism on Maio, Cape Verde Islands. *Earth and Planetary Science Letters* **64**, 61–76.

Mitchell-Thomé, R. C. (1976). *Geology of the Middle Atlantic Islands*. Berlin: Bornträger.

Mukhopadhyay, S., Lassiter, J. C., Farley, K. A. & Bogue, S. W. (2003). Geochemistry of Kauai shield-stage lavas: implications for the chemical evolution of the Hawaiian plume. *Geochemistry, Geophysics, Geosystems* 2002GC000342.

Natland, J. (1977). Composition of basaltic rocks recovered at sites 367 and 368, Deep Sea Drilling Project, near the Cape Verde Islands. In: Lancelot, Y., Seibold, E., *et al.* (eds) *Initial Report of the Deep Sea Drilling Project,* **41**. Washington, DC: US Government Printing Office pp. 1107–1112.

Parsons, B. & McKenzie, D. (1978). Mantle convection and the thermal structure of the plates. *Journal of Geophysical Research* **83**, 4485–4496.

Phipps Morgan, J., Morgan, W. J. & Price, E. (1995). Hotspot melting generates both hotspot volcanism and a hot spot swell? *Journal of Geophysical Research* **100**, 8045–8062.

Plesner, S., Holm, P. M. & Wilson, J. R. (2002). $^{40}Ar/^{39}Ar$ geochronology of Santo Antão, Cape Verde Islands. *Journal of Volcanology and Geothermal Research* **120**, 103–121.

Pollitz, F. F. (1991). Two-stage model of African absolute motion during the last 30 million years. *Tectonophysics* **194**, 91–106.

Putirka, K. (1999). Melting depths and mantle heterogeneity beneath Hawaii and the East Pacific Rise: constraints from Na/Ti and rare earth element ratios. *Journal of Geophysical Research* **104**, 2817–2829.

Rudnick, R. L. & Fountain, D. M. (1995). Nature and composition of the continental crust. *Reviews in Geophysics* **33**, 267–309.

Sack, R. O. & Ghiorso, S. (1991). Chromite as a petrogenetic indicator. In: Lindsley D. H. (ed.) *Oxide Minerals: Petrologic and Magnetic Significance. Mineralogical Society of America, Reviews in Mineralogy* **25**, 323–353.

Sack, R. O. & Carmichael, I. S. E. (1984). Fe^{2+}–Mg^{2+} and $TiAl_2$–$MgSi_2$ exchange reactions between clinopyroxenes and silicate melts. *Contributions to Mineralogy and Petrology* **85**, 93–115.

Serralheiro, A. (1976). A geologia da Ilha de Santiago (Cabo Verde). *Bolletin do Museu e Laboratorio Mineralógico e Ge lógco da Faculdade de Ciências* **14**, 157–369.

Simonsen, S. L., Neumann, E.-R. & Seim, K. (2000). Sr–Nd–Pb isotope and trace-element geochemistry evidence for a young HIMU source and assimilation at Tenerife (Canary Island). *Journal of Volcanology and Geothermal Research* **103**, 299–312.

Sleep, N. H. (1990). Hotspots and mantle plumes: some phenomenology. *Journal of Geophysical Research* **95**, 6715–6736.

Stillman, C. J., Furnes, H., Le Bas, M. J., Robertson, A. H. F. & Zielonka, J. (1982) The geological history of Maio, Cape Verde islands. *Journal of the Geological Society, London* **139**, 347–361.

Sun, S.-S. & McDonough, W. F. (1989). Chemical and isotopic systematics of oceanic basalts: implications for mantle composition and processes. In: Saunders, A. D. & Norry, N. J. (eds) *Magmatism in the Ocean Basins. Geological Society, London, Special Publications* **42**, 313–345.

Thirlwall, M. F. (1997). Pb isotopic and elemental evidence for OIB derivation from young HIMU mantle. *Chemical Geology* **139**, 51–74.

Todt, M. W., Cliff, R. A., Hanser, A. & Hofmann, A. W. (1993). Recalibration of NBS lead standards using a $^{202}Pb + {}^{205}Pb$ double spike. *Terra Nova* **5**(1), 396.

Ulmer, P. (1989). The dependence of the Fe^{2+}–Mg cation-partitioning between olivine and basaltic liquid on pressure, temperature and composition: an experimental study to 30 kbars. *Contributions to Mineralogy and Petrology* **101**, 261–273.

Vidal, Ph. (1992). Mantle: more HIMU in the future? *Geochimica et Cosmochimica Acta* **56**, 4295–4299.

Walter, M. J. (1998). Melting of garnet peridotite and the origin of komatiite and depleted lithosphere. *Journal of Petrology* **39**, 29–60.

Weaver, B. L. (1991). The origin of ocean island basalt end-member compositions: trace element and isotopic constraints. *Earth and Planetary Science Letters* **104**, 381–397.

White, W. M. (1993). $^{238}U/^{204}Pb$ in MORB and open system evolution of the depleted mantle. *Earth and Planetary Science Letters* **115**, 211–226.

Williams, C. A., Hill, I. A., Young, R. & White, R. S. (1990). Fracture zones across the Cape Verde Rise, N. E. Atlantic. *Journal of the Geological Society, London* **147**, 851–857.

Wyllie, P. J. (1989). Origin of carbonatites: evidence from phase equilibrium studies: In: Bell, K. (ed.) *Carbonatites: Genesis and Evolution*. London: Unwin Hyman, pp. 500–545.

Zindler, A. & Hart, S. (1986). Chemical geodynamics. *Annual Reviews in Earth and Planetary Sciences* **14**, 493–571.

Appendix A: Comparison between measured and reference values for some standards, internal analytical precision and detection limits for XRF, INAA and ICP-MS analyses

Element		XRF				INAA					ICP-MS					
		Precision (rel %) (1σ)	LLD* (ppm)	Standard		Precision (rel %) (1σ)	LLD* (ppm)	Standard			Standard measurements					
				AGV-1	AGV-1			BHVO1			BE-N	BE-N	BCR-1	BCR-1	SARM40	
				meas† (ppm)	Ref.‡ (ppm)			meas† (ppm) (AVG)	±1σ (ppm) (*N*=5)	Ref.‡ (ppm)	meas†	Ref.‡	meas†	Ref.‡	meas†	Ref.‡
Sc	ppm	5	<1	13	12·1	0·2	0·006	31·7	0·5	31·8	24·4	22·3	30·3	32·1	8·4	8·8
Ti	wt %										1·63	1·57	1·26	1·34	0·02	0·03
V	ppm	5	<3	119	123						238	235	395	407	22	27
Cr	ppm	5	<3	11	12						363	365	9·6	10·8	37	35
Mn	wt %										0·16	0·15	0·14	0·14	0·13	0·14
Co	ppm	4	<1	12·5	15						65·3	62·4	38·5	37·2	14·9	15
Ni	ppm	2	<1	14	17						280	267	10·1	13	23·8	25
Cu	ppm	5	<2	58	60						72	72	22·7	19	3·9	10
Zn	ppm	5	<1	84	88						123	120	119	129·5	20·5	25
Ga	ppm	5	<1	20	20						18	17	22·50	22	2·0	10
Rb	ppm	2	<0·5	66	67						49	47	46·7	47·2	1·02	1·3
Sr	ppm	1	<0·5	652	662						1363	1370	312	330	1648	1650
Y	ppm	5	<1	20	21						29·8	30	34·7	38	33·6	33
Zr	ppm	2	<1	223	225						270	260	185·9	190	48·3	87
Nb	ppm	2	<0·5	14·4	15						116	105	9·7	14	7·85	10
Cs	ppm					12	0·1				0·77	0·740	0·92	0·957	0·08	0·081
Ba	ppm	2	<1	1204	1221	8	26	139	16		1041	1006	628	661	448	447
La	ppm	2	<1	38	38	0·7	0·07	16·3	0·4	13·8	85·0	82·7	24·2	25·1	70·6	70·1
Ce	ppm	2	<2	69	66	0·4	0·45	39	3	39	161·1	151	50·9	52·6	153·7	151
Pr	ppm										17·34	17	6·63	6·5	18·53	17
Nd	ppm	4	<1	34	34	10	5	27·1	1·9	25·2	66·5	65	28·3	27·5	70·54	68
Sm	ppm					0·6	0·05	6·2	0·4	6·2	12·19	12·17	6·52	6·65	11·74	11·81
Eu	ppm					0·6	0·009	2·07	0·03	2·06	3·54	3·63	1·87	1·942	3·20	3·32
Gd	ppm										11·4	9	6·98	6·2	11·05	8·4
Tb	ppm					8	0·07	1·03	0·10	0·96	1·34	1·26	1·11	1·03	1·25	1·21
Dy	ppm										6·64	6·5	6·40	6·3	6·75	6·7
Ho	ppm										1·19	1·2	1·28	1·3	1·24	1·3
Er	ppm										2·67	2·6	3·64	3·6	3·15	3·1
Tm	ppm										0·32	0·32	0·52	0·52	0·42	0·42
Yb	ppm					5	0·1	1·6	0·2	2·02	1·79	1·76	3·33	3·3	2·43	2·47
Lu	ppm					5	0·02	0·27	0·05	0·291	0·25	0·239	0·51	0·487	0·34	0·352
Hf	ppm					0·6	0·05	4·4	0·2	4·38	5·69	5·85	5·10	5·00	0·81	1·7
Ta	ppm					1	0·03	1·17	0·08	1·23	5·24	5·62	0·65	0·757	0·62	0·6
Pb	ppm	20	1	35	36						4·07	4·00	13·38	13·6	15·63	20
Th	ppm	20	1	7	6·5	2	0·06	1·06	0·13	1·08	9·80	10·23	6·58	5·69	5·04	5·18
U	ppm										2·32	2·4	1·70	1·66	0·13	0·13

*LLD, Lower Limit of Detection. †Measured value. ‡Govindaraju (1994).

Appendix B. Parameters for the melting calculations

Modes (wt %)		olivine	opx	cpx	garnet	spinel
Mantle mode:	Garnet peridotite	50%	25%	15%	10%	
	Spinel peridotite	46·5	35	15		3·5
Melting mode:	Garnet peridotite	19	−50	68	63	
	Transition	−1·5	−6	69·5	31·5	6·5
	Spinel peridotite	−22	38	71		13

Partitioning coefficients mineral/melt (Halliday et al., *1995)*

	olivine	opx	cpx	garnet	spinel
La	0·0002	0·0031	0·054	0·0007	0·0006
Sm	0·0009	0·0037	0·27	0·22	0·0059
Tb	0·0015	0·019	0·31	0·75	0·00105
Yb	0·024	0·038	0·43	6·4	0·0045
Nb	5e−5	0·003	0·0089	0·01	0·08
Zr	0·001	0·012	0·26	0·2	—

Garnet to spinel transition:

Molar: Spi + 2opx = gar + ol, weight: 14/40spi + opx = gar + 14/40ol

Chemical composition (ppm)	DM*	PM†	carbonatite‡
La	0·687	0·206	262
Sm	0·444	0·299	42·9
Tb	0·084	0·077	5·35
Yb	0·372	0·347	9·21
Nb	0·712	0·39	398
Zr	11·2	7·19	180

*McKenzie & O'Nions (1991); †Sun & McDonough (1989); ‡T. F. Kokfelt (personal communication).
Adiabatic melting modelling was based on: $dF/dP = (dT/dP_{adiabat} - dT/dP_{solidus})/(H_{fusion}/C_P)$ (Langmuir *et al.*, 1992), $dT/dP_{adiabat} = 10^{\circ}C/GPa$, $dT/dP_{solidus} = 130^{\circ}C/GPa$ (McKenzie & Bickle, 1988) and $H_{fusion} = 180$ cal/(Hess, 1992) $C_P = 0{\cdot}3$ cal/(g°C), porosity: 0·3%).